Multiscale Modeling of Fatigue and Fracture in Polycrystalline Metals, 3D Printed Metals, and Bio-inspired Materials

Mohamad Ghodratighalati

Dissertation submitted to the faculty of the Virginia Polytechnic Institute and State University in partial fulfillment of the requirements for the degree of

Doctor of Philosophy

In

Mechanical Engineering

Reza Mirzaeifar, Chair

Mehdi Ahmadian

Christopher B. Williams

Matthew H. Hebdon

Pinar Acar

February 13, 2020

Blacksburg, Virginia

Keywords: Rolling contact fatigue, Multiscale modeling, Microstructure, Fatigue, Selective laser melting, Bio-inspired material

Multiscale Modeling of Fatigue and Fracture in Polycrystalline Metals, 3D Printed Metals, and Bio-inspired Materials

Mohamad Ghodratighalati

ABSTRACT

The goal of this research is developing a computational framework to study mechanical fatigue and fracture at different length scales for a broad range of materials. The developed multiscale framework is utilized to study the details of fracture and fatigue for the rolling contact in rails, additively manufactured alloys, and bio-inspired hierarchical materials. Rolling contact fatigue (RCF) is a major source of failure and a dominant cause of maintenance and replacements in many railways around the world. The highly-localized stress in a relatively small contact area at the wheel-rail interface promotes micro-crack initiation and propagation near the surface of the rail. 2D and 3D microstructural-based computational frameworks are developed for studying the rolling contact fatigue in rail materials. The method can predict RCF life and simulate crack initiation sites under various conditions. The results obtained from studying RCF behavior in different conditions will help better maintenance of the railways and increase the safety of trains.

The developed framework is employed to study the fracture and fatigue behavior in 3D printed metallic alloys fabricated by selective laser melting (SLM) method. SLM method as a part of metal additive manufacturing (AM) technologies is revolutionizing the manufacturing sector and is being utilized across a diverse array of industries, including biomedical, automotive, aerospace, energy, consumer goods, and many others. Since experiments on 3D printed alloys are considerably time-consuming and expensive, computational analysis is a proper alternative to reduce cost and time. In this research, a computational framework is developed to study fracture and fatigue in different scales in 3D printed alloys fabricated by the SLM method. Our method for studying the fatigue at the microstructural level of 3D printed alloys is pioneering with no similar work being available in the literature. Our studies can be used as a first step toward establishing comprehensive numerical frameworks to investigate fracture and fatigue behavior of 3D metallic devices with complex geometries, fabricated by 3D printing.

Composite materials are fabricated by combining the attractive mechanical properties of materials into one system. A combination of materials with different mechanical properties, size, geometry, and order of different phases can lead to fabricating a new material with a wide range of properties. A fundamental problem in engineering is how to find the design that exhibits the best combination of these properties. Biological composites like bone, nacre, and teeth attracted much attention among the researchers. These materials are constructed from simple building blocks and show an uncommon combination of high strength and toughness. By inspiring from simple building blocks in bio-inspired materials, we have simulated fracture behavior of a pre-designed composite material consisting of soft and stiff building blocks. The results show a better performance of bio-inspired composites compared to their building blocks. Furthermore, an optimization methodology is implemented into the designing the bio-inspired composites for the first time, which enables us to perform the bio-inspired material design with the target of finding the most efficient geometries that can resist defects in their structure. This study can be used as an effective reference for creating damage-tolerant structures with improved mechanical behavior.

Multiscale Modeling of Fatigue and Fracture in Polycrystalline Metals, 3D Printed Metals, and Bio-inspired Materials

Mohamad Ghodratighalati

GENERAL AUDIENCE ABSTRACT

The goal of this research is developing a multiscale framework to study the details of fracture and fatigue for the rolling contact in rails, additively manufactured alloys, and bio-inspired hierarchical materials. Rolling contact fatigue (RCF) is a major source of failure and a dominant cause of maintenance and replacements in many railways around the world. Different computational models are developed for studying rolling contact fatigue in rail materials. The method can predict RCF life and simulate crack initiation sites under various conditions and the results will help better maintenance of the railways and increase the safety of trains.

The developed model is employed to study the fracture and fatigue behavior in 3D printed metals created by the selective laser melting (SLM) method. SLM method as a part of metal additive manufacturing (AM) technologies is revolutionizing industries including biomedical, automotive, aerospace, energy, and many others. Since experiments on 3D printed metals are considerably time-consuming and expensive, computational analysis is a proper alternative to reduce cost and time. Our method for studying the fatigue at the microstructural level of 3D printed alloys can help to create more fatigue and fracture resistant materials.

In the last section, we have studied fracture behavior in bio-inspired materials. A fundamental problem in engineering is how to find the design that exhibits the best combination of mechanical properties. Biological materials like bone, nacre, and teeth are constructed from simple building blocks and show a surprising combination of high strength and toughness. By inspiring from these materials, we have simulated fracture behavior of a pre-designed composite material consisting of soft and stiff building blocks. The results show a better performance of bio-inspired structure compared to its building blocks. Furthermore, an optimization method is implemented into the designing the bio-inspired structures for the first time, which enables us to perform the bio-inspired material design with the target of finding the most efficient geometries that can resist defects in their structure.

Acknowledgment

I would like to thank my advisor, Dr. Reza Mirzaeifar, for his advice and support during this study. I have been very pleased to have the chance to work with him during these years and his support and guidance throughout my research have been the most valuable gift. I will never be able to express the level of my gratefulness for all the things I learned from him. Those are not just limited to the research matters; I have learned many general things from him, which I will be using in my life.

I am sincerely thankful to Dr. Mehdi Ahmadian, for his fruitful discussions and valuable comments throughout this project. He has been very supportive and helpful, and I have learned lots of valuable things from him.

I would also like to thank the members of my committee, Dr. Christopher B. Williams, Dr. Matthew H. Hebdon, and Dr. Pinar Acar for their advice and for being kind enough to serve on my graduate committee.

I would like to acknowledge the financial support provided by the Association of American Railroads (AAR) through the Technology Outreach program. I also greatly acknowledge the technical support provided by Mr. Steve Dedmon of Standard Steel and Mr. Brad Kerchof of Norfolk Southern during this study.

No work can be successful without the encouragement and support of the family. This work would not have been possible without the love and support of my lovely wife Zahra. I am also indebted to my parents for their great support and care in my entire life, without whom I would never achieve anything I have achieved.

Table of Contents

List of Figures

List of Tables

Chapter 1

1. Introduction

The goal of this research is developing a computational framework to study mechanical fatigue and fracture at different length scales for a broad range of materials. The proposed multiscale framework is utilized to study the details of fracture and fatigue for the rolling contact in rails (chapters 2 and 3), additively manufactured metals (chapter 4), and bio-inspired hierarchical materials (chapter 5). This dissertation is organized as follows. In chapter 1, each of the studied topics is briefly introduced. In chapter 2, details of microstructural modeling framework development for rolling contact fatigue analysis are presented, and several effective parameters on rolling contact fatigue are discussed. In chapter 3, a three-dimensional computational approach for rolling contact fatigue study is described. In chapter 4, we have analyzed fracture and fatigue behavior of 3D printed metals and studied effective parameters on fracture and fatigue behavior. In chapter 5, bio-inspired materials are studied under static loading, and their behavior is simulated with the finite element method. Furthermore, we have used an optimization method to find the optimum design for bio-inspired damage-tolerant structures.

1.1. Modeling of Rolling Contact Fatigue in Rails at the Microstructural Level

Rolling contact fatigue (RCF) is a major source of failure and a dominant cause of maintenance and replacements in many railways around the world. The cost of RCF defects to the United States and European rail system exceeds many millions of dollars annually [1-3]. The highly-localized stress in a relatively small contact area at the wheel-rail interface promotes micro-crack initiation and propagation near the surface of the rail. With repetitive forces, the micro-cracks grow to the surface of the rail and eventually lead to loss of material through growth deformation or chipping. Fig. 1-1 shows metal spalling on the rail surface that formed because of rolling contact fatigue.

Fig. 1-1. Metal spalling from the rail surface is happened due to rolling contact fatigue.

computational frameworks have been commonly used to study the subsurface stresses in Hertzian contacts for various geometries applicable to study both wheel-rail and ball-roller contact in bearings [4-7]. Although the continuum models can predict many essential properties of RCF, the fatigue behavior of polycrystalline materials is significantly influenced by their microstructural topology, which is ignored in most continuum-based theoretical and computational studies. Empirical models, as well as experimental studies, have confirmed the effect of grain sizes and texture on the fatigue response of polycrystalline metals [8-10]. Some efforts have been reported on developing discrete damage mechanics models for high cycle fatigue in polycrystalline materials, subjected to rolling contact. Mainly developed for studying rolling-element bearings and gears, these models use a stochastic fatigue model to analyze the initiation and propagation of fatigue damage in polycrystalline materials that are modeled by a number of individual crystals or grains separated by the grain boundaries [11-14].

Bomidi et al. [15] created a 3D microstructural geometry to study RCF in roller bearings. They used homogenous material properties in their model and statistically studied the initiation of cracks and failure in the model. Franklin et al. [16] introduced a new mechanism to distinguish RCF growth in pearlitic microstructures with different percentage volumes of pro-eutectoid ferrite, through conducting a series of twin-disk experiments that are compared with simulation results. The study finds that RCF growth decreases with decreasing ferrite volume fraction.

Grain boundaries play an important role in the mechanical properties of materials; however, they are not considered in most models for studying RCF. Most cracks initiate from grain boundaries that are most susceptible to the initiation of crack. Slack and Sadeghi [17] considered cohesive

elements in their model to study RCF in bearings. The study uses elastic material properties for grains, with fatigue damage at the grains, not grain boundaries.

This study develops a finite element framework for studying RCF at the microstructural level, including the grain boundaries, using a cohesive zone approach. The model will be used to study the effect of temperature, traction coefficient, and grain size on the initiation and growth of RCF.

The study focuses on the highly localized stresses at the small contact area between the passing wheel and rail, commonly referred to as the "contact patch." The grains and grain boundaries are considered as the main two features at the contact patch. The grain shapes and morphology are modeled by the Voronoi tessellation method that is often used as a realistic approximation of actual microstructure for non-uniform grain shapes [18-21]. The grains are modeled as elastic-plastic material and the grain boundaries as zero-thickness cohesive elements. The elements follow the traction-separation law. The weakening at the grain boundaries due to repeated loads is reflected in the model through a damage evolution law, during the loading cycle. A major difficulty in investigating RCF is the computational limitation in simulating a high number of loading cycles of the wheel passage on the rail. This issue is addressed by using the jump-in-cycle approach. In order to simulate the cyclic loading, moving Hertzian load is applied to the rail model, while periodic boundary conditions are applied to the boundaries to improve the accuracy of the results and eliminating the edge effects.

The model is used to study the mechanisms of crack initiation and propagation due to RCF, and the interaction of crack propagation with the microstructure of the material. Effect of various parameters on RCF including different traction coefficients, temperature change, maximum contact pressure, and grain size is investigated.

1.2. Three-dimensional analysis of rolling contact fatigue using crystal plasticity finite element method and cohesive zone modeling

Rolling contact fatigue (RCF) is widely considered to be one of the prominent causes of failure and maintenance costs in railways, bearings, and gears [12, 22, 23]. More than 30 percent of rail grinding costs in North America can be attributed to RCF [24]. Untreated RCF cracks promote the chance of failure and may lead to accident and loss of life. RCF cracks form due to highly

localized and repeated stresses at a small contact area during rolling motion. These cracks can form at the surface or under the surface of contact area, and can be removed by grinding at the early stages; however, deep and untreated cracks may grow to the surface and cause catastrophic failures. RCF cracks are proven experimentally to be highly dependent on the microstructure [25]. Therefore, a proper 3D approach to capture the microstructural response and orientation-dependent mechanical behavior is required. Microstructural study of RCF is performed by many researchers in different applications such as bearings, gears, rails, and wheels [15, 26-29]. Slack and Sadeghi [17] combined microstructural effect and cohesive zone approach together to study the RCF in bearings. They used elastic material properties with considering fatigue damage in the grains and were able to simulate crack initiation and propagation in bearing subsurface. Franklin et al. [16] developed a computational model for simulation of pearlitic microstructure in different rails. They used regular hexagonal microstructure to represent the pearlite grains with pro-eutectoid ferrite grain boundaries. Their model was able to distinguish between the RCF life of rails with different pro-eutectoid ferrite percentage. In spite of computational efforts to study the microstructural effect on RCF, there is still need for a comprehensive approach that reflects all the effects of micro-scale plasticity, grain microstructure, orientation, as well as grain boundaries.

Using a crystal plasticity finite element is a common approach to study the elastic-plastic deformation at the microstructural level [30-32]. This method considers the slip systems in polycrystalline materials and provides a precise stress-strain behavior as well as local deformation. This method considers orientation-dependent properties. However, there are limited implementations of this approach in rolling contact fatigue studies. Alley et al. [33] developed a two-phase crystal plasticity model to study the effect of inclusions and phase transformation on rolling contact fatigue in bearing steels. Noyel and colleagues [14] considered crystal anisotropy using a crystal elasticity model to study the effect of anisotropy on rolling contact fatigue. They studied the influence of crystal elasticity on microcrack distribution and used a cohesive zone method for simulation of interfaces. Paulson et al. [34] studied the effect of topology and crystal orientations on rolling contact fatigue in bearings using a crystal elasticity model. They found that elastic anisotropy provides a good description of scatter in rolling contact fatigue life of bearings. A recent research conducted by Vijay et al. [35] implemented a 3D approach to study the effect of microstructure and crystal anisotropy on rolling contact fatigue in bearings. The

predicted fatigue lives by their model were in good agreement with the RCF experiments. In a recent study, Wang et al. [36] studied the microstructure sensitivity of rolling contact fatigue in wind turbine gears. They used a crystal plasticity finite element with the Fatemi-Socie fatigue indicator parameter. They found the possible depth of RCF cracks and estimated crack angles based on the place of maximum fatigue indicator.

In this research, a 3D model with an explicit generation of microstructure using the Voronoi tessellation algorithm is created. We implemented a crystal plasticity constitutive model to simulate material behavior in grains. Since crystal plasticity considers the grain characteristics like slip systems and slip planes, it is vital to use this method for studying RCF because of its microstructure dependence nature. Cohesive elements are used at the interfaces to mimic the effect of grain boundaries, and an energy-based fatigue evolution law developed by Jiang and Sehitoglu [37] is applied to simulate fatigue damage at the grain boundaries. To the best of our knowledge, this promises to be a unique approach in studying RCF, which uses crystal plasticity for grains and considers fracture behavior at grain boundaries at the same time. In order to simulate the material behavior precisely, a two-step calibration method is utilized to calibrate the crystal plasticity model and cohesive element parameters. The effects of tangential forces and partial slip condition on RCF are studied by using the developed model.

1.3. Fatigue and fracture analysis of 3D printed metallic alloys at the microstructural level

1.3.1. Fracture modeling of metallic alloys made by additive manufacturing

Selective laser melting (SLM) as a part of metal additive manufacturing (AM) technologies is revolutionizing the manufacturing sector and is being utilized across a diverse array of industries, including biomedical, automotive, aerospace, energy, consumer goods, and many others [38-40]. In this AM process, a laser or an electron beam selectively melts a metal powder layer according to the geometry information provided by the machine control software. After solidification of the melt pool, the building platform drops down and a new powder layer is deposited on it, and the melting, solidification procedures are repeated several times until the physical part is created completely. Fig. 1-2 shows one of our recent results on characterizing the microstructure of a

fabricated part with the explained process under an optical microscope. A stacking of connected melt pools is clearly shown in this image.

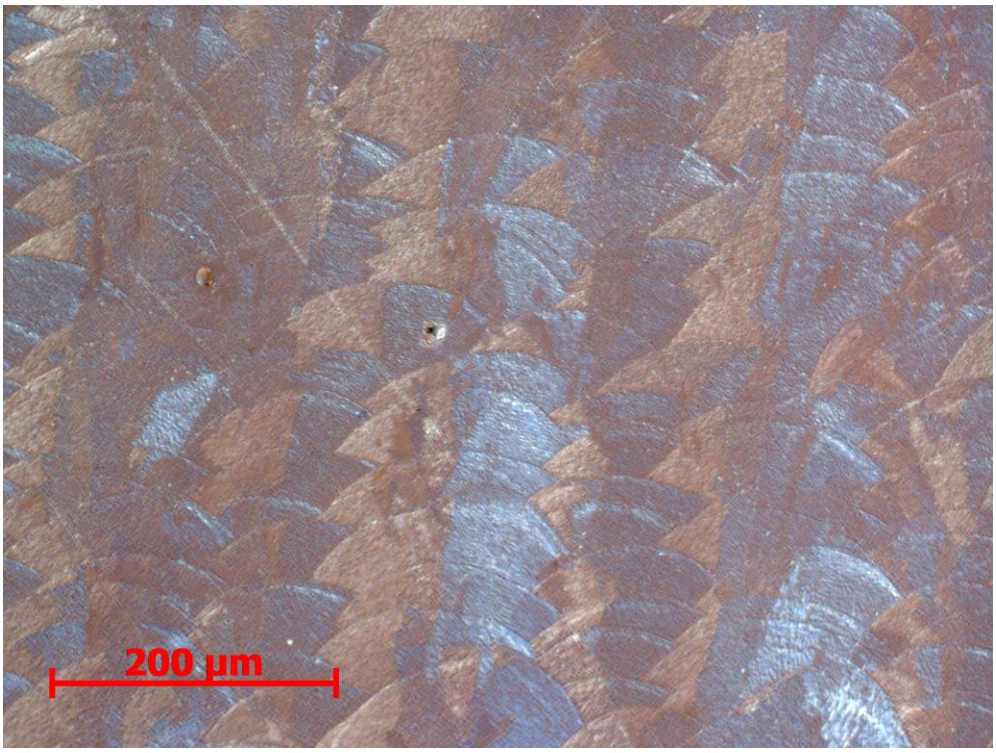

Fig. 1-2. An optical microscope image of melt pools in a fabricated part by selective laser melting method

The main challenge in the widespread adoption of metal AM technologies is the qualification of final products [41]. The mechanical properties of the part should be above a certain engineering specification for it to meet its service requirement. The mechanical response of any metallic AM part is derived from its solidified microstructure features such as melt pool and grain morphologies, and texture [42]. Thermal gradient and various solidification rate [43, 44], detrimental phase formation during cooling [45, 46], texturing due to use of various laser scan strategies [47, 48], and building directions generate variability in the microstructure. Characterization of the aforementioned variables and their correlation with mechanical responses of AM materials requires a large set of experiments that extends the qualification time and costs. With the help of simulation tools, these variabilities could be reproduced and the outputs could be further used for the optimization of microstructures and mechanical properties before the actual product is printed.

Various works [49-53] have been published which predict the microstructures features of AM materials. Phase-field [50, 54], Cellular Automata [55, 56], and Monte-Carlo [57] methods are commonly used for the simulation of AM microstructures. Lu et al. [58] developed a phase-field model to fundamentally understand the effects of laser beam power and scanning speed, on the shape and the size of the melt pool, grain structure, and porosity. The model reveals scaling relations between the laser parameters and the depth and length of the melt pool, the porosity, and the grain density. Akram et al. [55] formulated a cellular automata-based two-dimensional microstructure model to study grain evolution in the AM process. Grain evolution in multilayer depositions using various scan patterns in different metallic AM techniques including selective laser melting directed energy deposition, electron beam melting is presented. The results exhibited a significant correlation of scan patterns with evolving grain orientations. Rodgers et al. [57] simulated 3D grain evolution of solidified structures using a Q-Potts Monte Carlo method. They showed different types of crystallographic orientation and grain evolution in AM process driven by various laser scan strategies.

Clearly, there is a demand to develop an integrated computational platform to simulate the interconnection between the predicted microstructural properties of melt pools and grains of the AM materials to their mechanical response. Recently, Andani et al. [59] introduced a microstructural-based computational model for the prediction of yield strength and plastic flow in the AM metallic components. In the current contribution, we extend this work by accurately modeling the interaction between the melt pools (MPs) to predict the damage properties of metallic parts made by AM. The new model reproduces the explicit microstructural representation including the morphology and crystallographic orientations of grains and melt pools of AM metallic components. Crystal plasticity constitutive equations are used to define the material properties of bulk grains and melt pools. Melt pool boundaries (MPBs) are distinguished and cohesive zone modeling is implemented to study the damage in the material. The developed model is calibrated with experiments, and several case studies are considered in this research to help further understand the potential of the model in predicting the role of processing parameters and defects in damage properties of AM metallic alloys. Although works in the current study focus on selective laser melting technique, the findings are expected to extend to other AM powder-based processes that have similar mechanisms, such as a direct metal deposition.

1.3.2. Computational Study of Fatigue in Sub-grain Microstructure of 3D Printed Alloys

Additive Manufacturing (AM) has the most appeal for fabricating highly customized metallic parts with complex geometries that cannot be easily produced by conventional methods [60-62]. Despite this unique superiority, the full potential of AM to provide new means for manufacturing load-bearing parts is not yet fully realized [63, 64]. This challenge originates from multiple sources, but with no doubt one of the prominent obstacles on the way of adapting AM to a broad range of applications is the mechanical properties of 3D printed metallic parts, particularly the fatigue response. During the past few years, hundreds of papers have been published on studying different aspects of 3D printing of metals and alloys. Among these, a large portion is dedicated to discovering the relationship between processing parameters and material properties. The mechanical properties of 3D printed alloys under static loading are now comparable with those fabricated by other conventional methods [64, 65]. However, despite tremendous achievements in the past few years, the performance of 3D printed metallic parts under cyclic loading, *i.e.* their low and high cycle fatigue resistance, is still a major concern. AM materials still exhibit significantly shorter low and high cyclic fatigue lives compared to their wrought form. Several studies have been performed on the effect of processing parameters as well as some other influential parameters on the fatigue behavior of 3D printed alloys. Fatemi et al. [66] presented their recent experimental studies on the parameters influencing fatigue behavior of additively manufactured Ti-6Al-4V. They examined the effects of defects, residual stresses, surface finish, geometry and size, layer orientation, and heat treatment. Furthermore, Yadollahi et al. [67, 68] studied building orientation, heat treatment, surface roughness, defect size and shape effects on fatigue behavior of selective laser melted 17-4 PH stainless steel and Inconel 718.

Despite the debates on the actual reasons for the shorter fatigue life of 3D printed metals [64], researchers are unanimous that the very complicated microstructure of 3D printed alloys is one of the leading reasons behind the weakness of their response in cyclic loadings. Failure by cyclic loading is mostly a local phenomenon driven by the stress concentrations at the heterogeneous microstructures, and 3D printed alloys have one of the most complicated microstructures in metals fabricated by any of the manufacturing methods. Molaei et al. [69] studied the relationship between microstructure and material cyclic properties. They analyzed the effect of defects, porosities and partially melted material on crack initiation and propagation of additively

manufactured Ti-6Al-4V. They concluded that an appropriate fatigue damage model can predict the fatigue behavior obtained from fatigue experiments. Fatigue properties of AlSi10Mg fabricated by selective laser melting were investigated by Romano et al. [70]. They analyzed the microstructure of samples to find defects and micro-cracks and employed defect-based modeling to predict the strength of the material under high cycle fatigue.

We target investigating this challenge from an unexplored perspective in which the microstructure is the basis for our studies. The microstructure in 3D printed alloys is composed of three interconnected structures, being melt pools, grains, and cells. These features are connected by boundaries, among which only grain boundaries are well-known and the mechanical response of cell- and melt pool-boundaries are still highly unexplored. In a set of recent works, we have established a framework that considers melt pools and grains in the microstructure with some simplifications [30, 71-74]. It has been observed that sub-grain (cellular) microstructure can accommodate strain more easily, and prevent crack initiation and propagation [75] which shows importance of cellular microstructure developed in laser 3D printing process.

In this research, we have focused on studying fatigue in intra-granular cell and cell boundaries. To our best knowledge, fatigue response of 3D printed alloys at the sub-grain level has not been studied so far. We assume a perfect microstructure without defects and porosities, and we only study the effect of sub-grain cellular microstructure. It is worth noting that the total volume of the 3D printed alloys is prominently filled with this sub-grain cellular microstructure. Although, in presence of defects, it is a low chance that fatigue starts at the cells, fatigue at this microstructural feature, particularly at low cycle, is prominently affected by the response at the cellular structures. This study will be extended in future works to include all the microstructural parameters that affect fatigue life. We have employed damage-based fatigue models to predict the fatigue life of the cellular microstructure observed in additively manufactured alloys.

1.4. Fracture analysis and optimization of bio-inspired composites

1.4.1. Fracture analysis of bio-inspired composites

Pioneer engineering applications need materials, which are lighter, stronger, tougher and multifunctional. Basic homogenous materials are not able to accomplish these requirements and therefore engineers are shifted their way towards hybrid materials. Hybrid materials are fabricated by combining the attractive mechanical properties of materials into one system. A combination of materials with different mechanical properties, size, geometry, and order of different phases can lead to fabricating a new material with a wide range of properties. A fundamental problem in engineering is how to find the design that exhibits the best combination of these properties.

In order to address this problem, biological composites like bone, nacre, and teeth attracted much attention among the researchers. These materials are constructed from simple building blocks and show an uncommon combination of high strength and toughness [76-79]. High mineral contents of these materials increase stiffness, and toughening mechanism governed by interfaces and architectures provides toughness [80, 81]. An important mechanism in these materials is crack bridging [82, 83], which means high amounts of energy are dissipated at the interfaces of building blocks. For instance, tooth enamel has great hardness, and it is composed of long rods with 5 μm diameters, which are covered by a thin layer of protein. This cover is a weak place offering path for crack propagation [84]. In the inner part of the enamel, these rods intersect with each other and form a complex architecture. Crack propagation in this area includes crack bridging and crack deflection. Stable cracks can stay there for many years and resist the continual loading of the teeth. Another example of hybrid materials is the nacre that is made of lamellar thin mineral plates bonded with soft proteins (Fig. 1-3a). When loaded along the direction of plates, it can absorb high amounts of energy due to the sliding of soft layers on each other, which offers a failure strain of 1% that is much more than mineral failure strain (Fig. 1-3b). Also, the high density of mineral contributes to high hardness and stiffness of nacre. The plastic region around the tip of cracks and crack bridging are the two main mechanisms that make superior toughness for nacre compared to the toughness of mineral and interfaces [84].

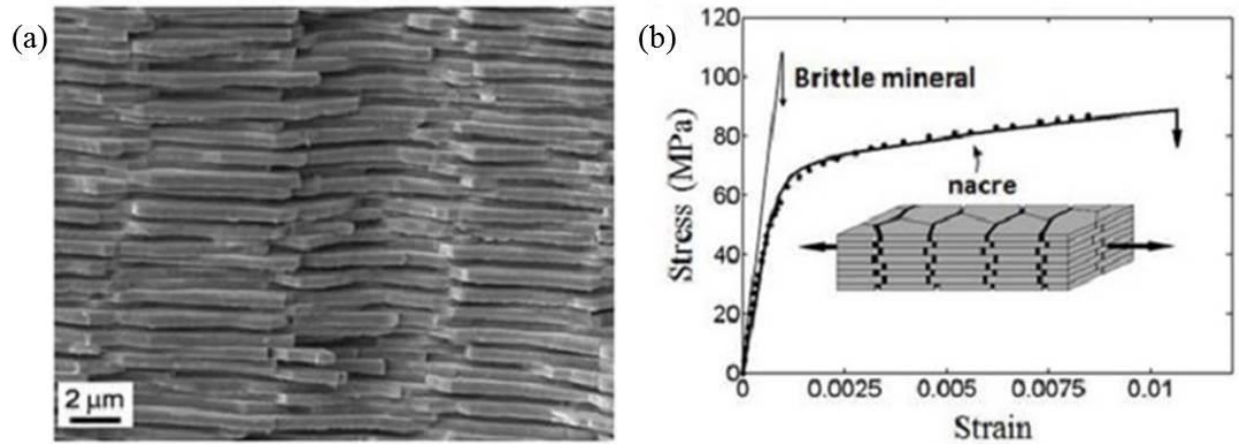

Fig. 1-3. (a) Scanning electron micrograph from fracture surface in nacre show mineral plates in a brick wall shape, (b) Tensile stress-strain curve of nacre compared to brittle mineral shows higher toughness and larger fracture strain (adapted from [84])

Many pieces of research are conducted to investigate the superior mechanical properties of biological composites due to their natural hierarchical system. Considering fracture behavior, many natural toughening mechanisms are found in these materials ranging from the nanoscale to the macroscale [79, 85-88]. Computational tools are used to gain more information about fundamental design principles used by nature to create such advanced materials from simple constituents [89-91]. Furthermore, analytical approaches have been employed to study the structure-property relationship of bio-composites with more focus on the effect of stiffness ratios on reducing the stress concentrations of the crack tip of lamellar structures [92, 93].

To fabricate these bio-inspired designs, different techniques and materials are employed by researchers. Dimas et al. [94] used additive manufacturing to make nacre-like and bone-like bio-inspired designs. They used a stiff polymer for hard mineral and a soft elastomer for the interface. In addition, they used a computational method to simulate composite behavior. They found a good agreement between experimental and computational results of mechanical properties. Livanov et al. [95] created a hybrid material composed of alumina and polymer, which resulted in a toughness that was one order of magnitude higher than bulk alumina. Other approaches like self-assembly [96], layer-by-layer deposition [97], freeze casting [98, 99] and using magnetic fields to orient microscopic plates [100].

During manufacturing or operation, some defects can be generated inside the material, which are inevitable. One of the important demands in the design of composite materials is increasing the material strength in the presence of defects, which are called damage-tolerant materials. Mirzaeifar et al. [101] used a computational approach and multi-material additive manufacturing to study different classes of bio-inspired damage-tolerant designs. They found that hierarchical architecture leads to higher defect-tolerant properties, and increasing the hierarchical level improves the defect tolerance dramatically. They introduced random cracks inside their computational model and found that in high levels of hierarchy, a large portion of strength remains unchanged even in the presence of cracks.

1.4.2. Optimum design for damage-tolerant multi-material composites

A novel method to design hybrid materials is the optimization with the utilization of Machine Learning (ML) algorithms. The ML paradigm has been recently introduced to materials modeling and design problems [102-107]. A generic ML model enables the integration of mathematical techniques into the experimental data sets and physics-based models. The basic principles behind ML algorithms are the mapping between the fingerprints and target properties. In the case of composite materials, the ML algorithms were used to study the design of 3D printed composites involving multiple phases to improve the mechanical performance of materials [108-110]. One efficient method is the Radial Basis Function (RBF) network, which is implemented in this work to design the damage-tolerant materials. The RBF is a class of artificial neural network models that is applied to the problems of supervised learning [111, 112]. By learning the fundamental design principles from nature, our goal is employing optimization methods to find the optimum distribution of soft phases in a hard and brittle phase in the presence of defects. We are focusing on finding the optimum design to reduce stress concentration and increasing the toughness and damage tolerance of a composite material. Due to the computationally expensive nature of the problem, we generate surrogates with the RBF algorithm to represent the original structural model and perform the design optimization on the surrogates. With the presented methodology, we have achieved significant improvement in the mechanical performance of damage-tolerant materials compared to the previous results. In addition, we have demonstrated an optimum design solution, for the first time, to a damage-tolerant material having multiple and oblique cracks, to the best of our knowledge.

Chapter 2

2. Modeling of Rolling Contact Fatigue in Rails at the Microstructural Level

2.1. Overview

A micromechanical-based finite element framework is developed to investigate the rolling contact fatigue (RCF) in rails. The microstructure of a representative part of the rail in contact with the wheel during wheel passage is modeled using the Voronoi tessellation algorithm. The geometry explicitly represents microstructural grain and grain interface features that represent the actual microstructure of rail steel. The grain interface is modeled using cohesive elements. For higher computational efficiency, moving the Hertzian load is applied to the rail surface instead of moving the wheel explicitly on top of the rail. The jump-in-cycles approach is employed to efficiently simulate a large number of loading cycles, while the material degradation at the grain interface is represented by an accurate damage evolution law. Additionally, the model is used to evaluate the effects of temperature change, traction coefficient, and grain size on the initiation and progression of RCF. The results indicate that colder temperatures increase the progression of RCF, while warmer temperatures do not have any significant effects. Large traction forces at the wheel-rail interface significantly accelerate RCF growth, mainly through migration of subsurface micro-cracks to the surface of the rail. The surface cracks grow into larger ones that lead to loss of rail material. Controlling the grain size can have a positive effect on both the initiation and migration of sub-surface cracks. Changing the yield strength of material with the Hall-Petch relation, the model evaluates the effect of refining the grain size. The results indicate that smaller grains can improve the RCF properties of the rail. The effect of maximum contact pressure on RCF is studied, and the results show a power relation between maximum contact pressure and RCF life. Also, several case studies are simulated and compared with experimental observations. The simulation results are in close agreement with the experimental observations for the crack pattern and crack depth.

2.2. Material modeling and methods

2.2.1. Grain material model

An elastic-plastic model that is a combination of isotropic and kinematic hardening is considered for the material. This model is capable of accurately predicting the cyclic loading effects, including cyclic softening/hardening, Bauschinger effect, and ratcheting. The model presented by Chaboche [113] has been widely used in recent years [114-117]. In this model, the isotropic hardening parameter R, defined as the change of yield stress for accumulated plastic strain p, is defined by

$$R = Q(1 - e^{-bp}) \tag{2-1}$$

where Q and b are material parameters.

The nonlinear kinematic hardening, called back stress tensor (X), defines the translation of yield surface, and is described by summation of N back stresses X_i [118]

$$X = \sum_{i=1}^{N} X_i \tag{2-2}$$

Nonlinear evolution law of kinematic hardening for isothermal conditions is defined by

$$\dot{X}_i = \frac{2}{3} C_i \dot{\varepsilon_p} - \gamma_i X \dot{p} \tag{2-3}$$

where C_i and γ_i are material parameters and $\dot{\varepsilon_p}$ is the plastic strain rate. A detailed definition of this plastic material law and calibration of its parameters is described in [119, 120]. For pearlitic rail steels, the material properties from [121] are used in this research.

2.2.2. Grain boundaries: cohesive elements

The grain boundary mechanics is simulated using zero-thickness cohesive elements at the grain interfaces. Cohesive elements follow the bilinear traction-separation law (shown schematically in Fig. 2-1). In this model, the traction between element surfaces increases linearly until a

maximum is reached, and then reduces to zero traction where final separation occurs. The latter part of the traction-separation curve (from maximum traction to zero traction) defines static damage (D_s) as an internal parameter. The static damage is zero at the maximum traction and linearly increases to one as the static degradation evolves (see Fig. 2-1). Abaqus, which is utilized in this study as the finite element software, uses strain (ε) instead of separation (δ) using

$$\varepsilon = \frac{\delta}{T_0} \tag{2-4}$$

where T_0 is the initial thickness assigned to the element.

The nominal tractions are related to the nominal strains of cohesive elements by the following elastic constitutive matrix [120]:

$$t = \begin{Bmatrix} t_n \\ t_s \\ t_t \end{Bmatrix} = \begin{bmatrix} E_{nn} & & \\ & E_{ss} & \\ & & E_{tt} \end{bmatrix} \begin{Bmatrix} \varepsilon_n \\ \varepsilon_s \\ \varepsilon_t \end{Bmatrix} = E\varepsilon \tag{2-5}$$

where E, t, and ε are elastic stiffness matrix, the nominal traction, and strain vectors, respectively. Each vector consists of three components; one normal (t_n or ε_n) and two shear components (t_s, t_t or $\varepsilon_s, \varepsilon_t$). Shear elastic stiffness is related to the normal elastic stiffness by [122]

$$E_{ss} = E_{tt} = \frac{E_{nn}}{2(1+\nu)} \tag{2-6}$$

where ν is Poisson's ratio. Static damage will initiate when

$$\left\{\frac{\langle t_n \rangle}{t_n^0}\right\}^2 + \left\{\frac{t_s}{t_s^0}\right\}^2 + \left\{\frac{t_t}{t_t^0}\right\}^2 = 1 \tag{2-7}$$

where t_n^0 , t_s^0, and t_t^0 are critical tractions for normal, first shear, and second shear directions, respectively. The symbol $\langle\ \rangle$ represents the Macaulay bracket that means damage will not initiate when the element is under compressive deformation. The Benzeggagh-Kenane (BK) criterion is used for defining the mixed-mode critical fracture energy (G^c) as

$$G^c = G_n^C + (G_s^C - G_n^C)\left(\frac{G_s + G_t}{G_n + G_s + G_t}\right)^{\eta} \tag{2-8}$$

where G_n, G_s, and G_t are the released energies in the normal, first, and second shear directions respectively. G_n^C, G_s^C and G_t^C are the critical fracture energies required for the failure in the normal, first, and second shear directions respectively, and η is a material constant. Normal and shear fracture energies are related to each other with the same equation given in (2-6). Using G^C, effective displacement at failure and accordingly static damage can be found [120, 122]. Progressive damage in fatigue situation (D_f) is also added to the cohesive zone approach by degrading the critical tractions (t_n^0, t_s^0, and t_t^0) and critical fracture energies (G_n^C, G_s^C, and G_t^C). For this purpose, an energy-based fatigue damage evolution law is used as described in section 2.2.3.

2.2.3. Damage evolution law

In order to study the rolling contact fatigue in railroad applications, Jiang and Sehitoglu [37] proposed an energy-based multiaxial fatigue criterion, which can be used for either normal cracking or shear cracking of materials. This evolution law has been used to model different responses of materials, and particularly has been shown to accurately predict the fatigue response of rail and wheel materials [123, 124]. The model searches for a critical plane by examining every possible direction. The obtained critical plane is then considered for further studies. A critical plane is a plane where the fatigue parameter (*FP*) is maximum. In this study, the model is applied to each cohesive element and it is assumed that damage occurs only in cohesive elements (grain boundaries). The fatigue parameter is expressed as

$$FP = \langle \frac{\Delta\varepsilon}{2}\, \sigma_{max} \rangle + J\, \Delta\gamma\, \Delta\tau \tag{2-9}$$

where $\Delta\varepsilon$ is the normal strain range in cyclic loading, σ_{max} is the maximum stress, $\Delta\gamma$ and $\Delta\tau$ are the shear strain range and shear stress range, respectively, and J is a material constant. All the above stresses and strains are calculated for each cohesive element in one loading cycle. The damage is related to the number of cycles (N) through the following damage evolution law

$$\frac{dD_f}{dN} = \frac{1}{N_f} = \frac{(FP - FP_0)^m}{C} \tag{2-10}$$

where D_f is the fatigue damage, which has a value between 0 and 1. N_f is the total life and FP_0, m and C are material constants. The damage will not be initiated when the FP is smaller or equal to FP_0.

By incorporating the described fatigue damage parameter (D_f), the degradation process is implemented in the model. As the number of cycles increases, the degradation of cohesive elements continues to evolve by decreasing the load-bearing capacity of the material (degrading the traction-separation response) until either static damage or fatigue damage becomes one [125] as shown in Fig. 2-1.

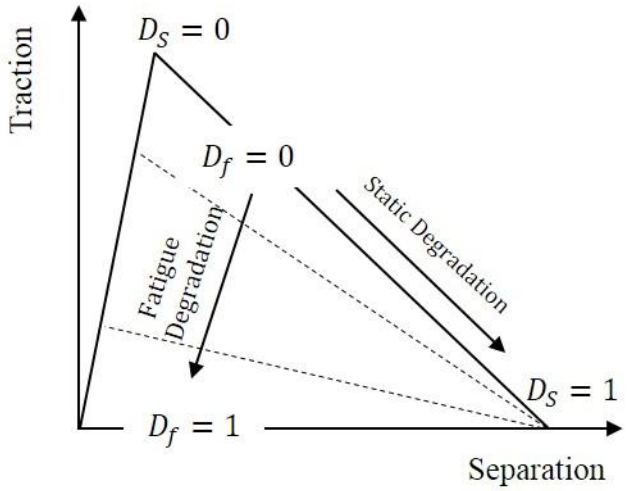

Fig. 2-1. Bilinear traction-separation curve, which shows fatigue damage (D_f) and static damage (D_s) parameters. Fatigue damage is applied with energy dissipation in cohesive elements (i.e., reduction in area under the curve).

Consequently, the degraded element will be removed from the simulation and the process will be continued until the remaining elements reach their failure. The process of implementing the damage evolution law in the high number of cycles is discussed in the next section.

2.2.4. Jump-in-cycles approach

Due to high complexities in the geometry and the material model, simulation of every single cycle is not feasible. To increase the computational efficiency and simulating the high number of cycles, the jump-in-cycles procedure is employed. In this method, which was first introduced by Lemaitre [126], stress histories are assumed to be constant over a finite number of cycles ΔN, called a block of cycles. Each block has variable amount of cycles, which is obtained through the following steps [11]: (i) The fatigue parameter $(FP)_j^i$ for each element j at the current block of cycle i is computed using Equation (2-9); (ii) The damage evolution rate according to Equation (2-10) is calculated in each element at each block as described by

$$\left(\frac{dD_f}{dN}\right)_j^i = \frac{\left((FP)_j^i - FP_0\right)^m}{C} \tag{2-11}$$

(iii) The element with the maximum amount of fatigue damage rate is chosen as the critical element for that block of cycle

$$\left(\frac{dD_f}{dN}\right)_{critical}^i = max\left|\left(\frac{dD_f}{dN}\right)_j^i\right| \tag{2-12}$$

(iv) The number of cycles (ΔN_i) in the current block is computed by

$$\Delta N_i = \frac{\Delta D_f}{\left(\frac{dD_f}{dN}\right)_{critical}^i} \tag{2-13}$$

where ΔD_f is the fatigue damage increment. This parameter is the maximum increment of fatigue damage that can be applied in each block of cycles. The effect and the procedure of selection of ΔD_f are discussed in section 2.4. (v) The number of cycles is updated using

$$N = N + \Delta N_i \tag{2-14}$$

(vi) The damage increment for each element is computed by

$$\left(\Delta D_f\right)_j^i = \left(\frac{dD_f}{dN}\right)_j^i \Delta N_i \tag{2-15}$$

(*vii*) Damage in each element for starting of the next block is updated as

$$\left(D_f\right)_j^{i+1} = \left(D_f\right)_j^i + \left(\Delta D_f\right)_j^i \tag{2-16}$$

(viii) All components of critical fracture energies (G_n^C, G_s^C and G_t^C) and critical traction stresses (t_n^0 , t_s^0 and t_t^0) are updated at the start of next block of cycles following equations

$$(G^C)_j^i = \left(1 - \left(D_f\right)_j^i\right)(G^C)_{initial} \tag{2-17}$$

$$(t^0)_j^i = \left(1 - \left(D_f\right)_j^i\right)(t^0)_{initial} \tag{2-18}$$

The described procedure is implemented into Abaqus by user-written USDFLD and UEXTERNALDB subroutines.

2.3. **Finite Element Modeling**

2.3.1. Microstructural modeling based on Voronoi tessellation

There is a variety of rail steels, such as pearlitic and bainitic rail steels, used in different regions [127]. Pearlitic rail steels have lamellar microstructure, and layers of ferrite and cementite are stacked together and a group of these layers forms a pearlite grain. The microstructure of an Evraz STD 132 rail sample (Fig. 2-2a) is studied using scanning electron microscopy (SEM). The cross-section of the rail is cut at different locations, and various surfaces in the rolling and lateral directions have been studied to extract the microstructure of this pearlitic rail steel. As shown in Fig. 2-2b, layers of ferrite and cementite can be clearly observed in the rail sample. By investigating different SEM images, pearlite grain sizes found to be in the range of 20-60 μm. This range is in agreement with reported values of pearlite grain sizes [127]. To study the effect of inter-lamellar spacing, and consider ferrite and cementite layers, a complex geometrical model

is required, which is the topic of future communication by the authors. In this research, a simplified geometrical model is considered, which is explained in the following.

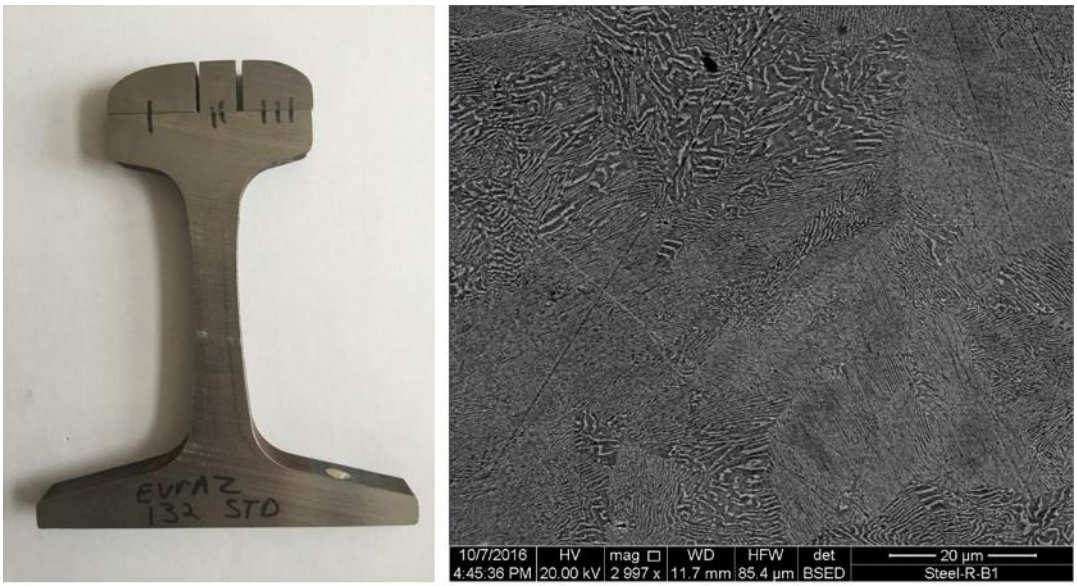

(a) (b)

Fig. 2-2. (a) Evraz standard rail sample, and (b) SEM image of rail sample showing a highly ordered lamellar structure of cementite (white) and ferrite (black).

By looking into the previously reported researches in the literature that study the rolling contact fatigue using the microstructural based models, the polycrystal structure was designed for simulating the microstructure as closely as possible to the actual structure (see Fig. 2 in [15] and Fig. 2 in [128]). In some of these works, cubic geometries are used for modeling the geometry of each grain, which means more assumptions are made [28]. In this research, a more realistic microstructure model is created using the Voronoi tessellation method. A set of randomly distributed seeds are used to construct Voronoi cells in a specific domain. Voronoi tessellation is similar to a microstructure where all the seeds nucleate simultaneously and grow isotropically to reach the neighboring grains [18]. In order to create finite element models based on Voronoi tessellation, open-source software Neper [129] is used in this research. It is preferred to study a group of domains and analyze the results with Weibull distribution. However, our purpose in this research is mostly studying the fundamental aspects of the RCF at the microstructural level, presenting our developed computational framework for studying RCF, and comparing changes in effective conditions (like temperature and traction coefficient) on RCF.

2D geometries of four different grain sizes are created. Each model has a representative volume element (RVE), which is focused in this study. The model size is selected $10a$ by $4a$, which is the same size as employed by Bomidi et. al [15]. They have validated the model size with the theory to be sure that edges do not affect the Hertzian load distribution. Also, damage outputs are taken from RVE only in this research, which is far from boundaries based on the Hertz contact theory [130]. Dimensions of RVE considered large enough to include all the cracks initiate from under the surface. The microstructure and finite element meshes of a created model are shown in Fig. 2-3, which $2a$ represents the length of contact patch between wheel and rail, and the rolling distance is $4a$. Based on [131] contact patch is around 10 mm, and this model is scaled to $1/10$ of real size for the computational efficiency, so $2a$ in this model is 1 mm. The model consists of 856 grains, which around 550 of these grains are positioned inside the RVE. The average equivalent diameter of each grain is 45 μm that is compliant with the grain size of pearlitic rail microstructure.

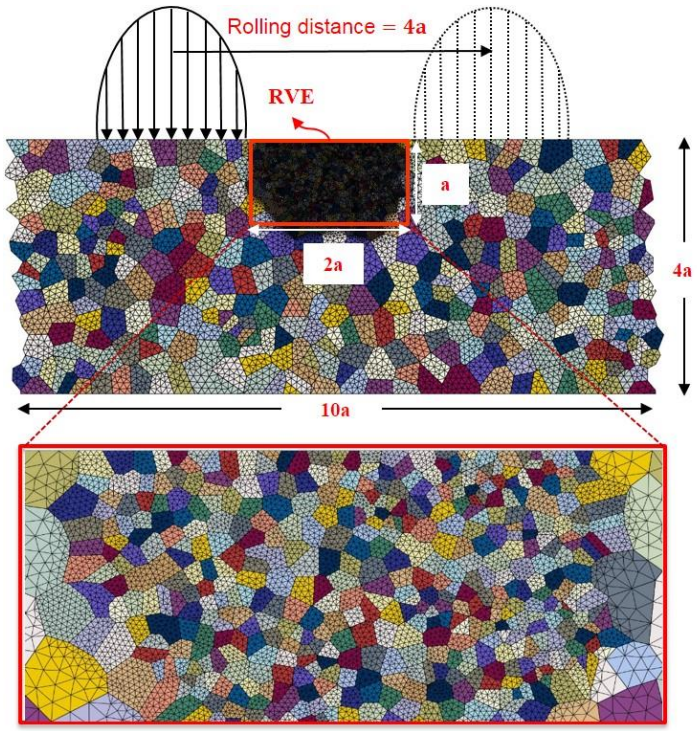

Fig. 2-3. Generated Voronoi microstructure (with 856 grains) that includes larger grains in the outer region, and fine grains with an average size of 45 μm in RVE. The contact patch size is $2a$, rolling distance is $4a$, and other sizes are labeled with respect to the size of the contact patch.

To reduce the computational efforts, real size grains are used in the RVE, and larger grains are employed in the outer regions. The model utilized in this research, shown in Fig. 2-3, is an improved version of a previously introduced finite element model [15]. Two major improvements are applied to the model. First, the boundary between RVE and the outer region is continuous in the presented model. Furthermore, the outer region grains are of the same shape as the grains inside RVE. Linear plane strain triangle elements (CPE3) are used to mesh the FE model. Each grain is meshed with respect to its size, so fine meshes in outer regions are avoided. Cohesive elements are applied between the grains as grain boundaries and meshed with 4-node two-dimensional cohesive elements (COH2D4). The geometrical thickness of these elements is zero before the start of the simulation, and they behave based on traction-separation law as discussed in section 2.2.2. The material properties used for cohesive elements and Jiang-Sehitoglu damage evolution law are given in Table 2-1.

Table 2-1. Simulation parameters, and material properties for cohesive elements and Jiang-Sehitoglu model

a) Simulation parameters		b) Cohesive element properties		c) Jiang-Sehitoglu model parameters [37]	
ΔD_f	0.1	$E_{nn}\ (GPa)$	200	FP_0	0.5
α $(1/°C)$	12×10^{-6}	$t_n^0\ (GPa)$	1.1	m	2
$p_{max}\ (GPa)$	1.0	$G_n^C\ (mJ/mm^2)$	0.0113	c	1.5×10^6
$a\ (mm)$	0.5	η	1	J	0.3
$\sigma_0\ (MPa)$	450	$T_0\ (mm)$	0.00018		
$k_{HP}\ (MPa.mm^{0.5})$	53				

2.3.2. Periodic Boundary Conditions

Careful consideration is necessary for representing the actual boundary conditions of a rail section. Rail section boundaries in simulation should not be free since they are supported by the rail steel in an actual case. Periodic boundary conditions (PBCs) are useful to avoid boundary effects and reduce the size of the model and make the model more like an infinite one. However, no PBC is present in normal load (y) direction, since the Hertzian load moves on the top surface and the bottom surface is fixed.

In order to have PBCs in rolling direction, displacement of similar nodes on opposite boundaries (left and right) must be related to each other through the following equation

$$u_a^x - u_b^x = 0 \tag{2-19}$$

where u_a^x and u_b^x are displacements of matching nodes on the left and right boundaries, respectively. Displacement of each node on the left side is coupled to the displacement of the same node on the right side by using Equation (2-19) in Abaqus. This equation also requires a periodic mesh along the x direction [132], which has been implemented in the model (See left and right boundaries in Fig. 2-3).

2.3.3. Cyclic loading: Moving normal and traction loads

Normal and tangential forces are two common forces between the wheel and rail. Different methods have been used in the literature in order to accurately apply these loadings. One method is using the full geometry of the wheel and a part of the rail. Although this is a desirable approach, it is a computationally expensive approach, particularly when the microstructure is modeled explicitly. As such, only a few cycles can be modeled (see [121]). Another method is using a moving Hertzian load, which helps to significantly reduce the computational time [123, 133, 134]. The Hertzian load distribution is applied as non-uniform, general surface traction vectors by use of UTRACLOAD user subroutine in Abaqus. The schematic of the moving Hertzian load is depicted in Fig. 2-3

In this model, the normal component of Hertzian pressure $p(x)$ for line contact loading is given by [4]:

$$p(x) = p_{max}\sqrt{1 - \left(\frac{x - x_c}{a}\right)^2} \tag{2-20}$$

where, p_{max} is the maximum pressure of Hertzian pressure distribution ($p_{max} = 1\ GPa$ in this research), x is the load position, x_c is the position of the maximum pressure and a is the half-width of contact patch length. The normal and tangential stresses are modeled with moving Hertzian load in this study. Tangential stress is also known as a tractive effort or traction vector,

and it moves the maximum shear stress location closer to the surface. The maximum traction $q(x)$ can be applied to the surface by the following equation

$$q(x) = \mu_{tr} \,.\, p(x) \tag{2-21}$$

where μ_{tr} is the traction coefficient. Figure 4 shows the variation of the traction $q(x)$ and pressure $p(x)$ along the contact patch. There are other theories describing the relationship between normal and traction forces, such as the well-known Kalker's theory [135]. While using the approximation given in Equation (2-21) is proven to be accurate enough, using more accurate theories will be the topic of future communication by the authors.

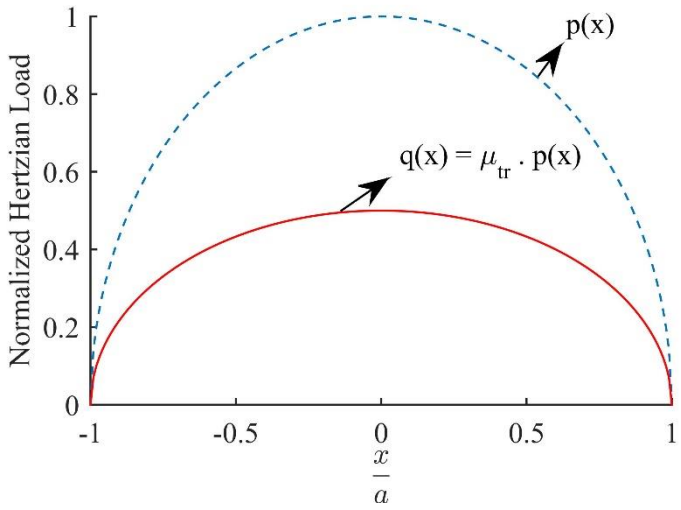

Fig. 2-4. Normal and traction stresses with Hertzian distribution. $p(x)$ is the normal pressure distribution and $q(x)$ is the traction distribution, which is assumed as a fraction of normal stress by employing Equation (2-21).

2.3.4. Applying temperature change

The temperature change can cause severe deformations in the longitudinal (rolling) direction of continuous rails. When there is no expansion space in the continuous rail, compression stresses arise above a specific temperature, while, below this temperature, tensile stresses arise. The temperature corresponding to no tension or compression stress in the rail is called "neutral temperature" [136]. The deformation due to temperature change can be in the form of buckling in the summer when there is high compression stress in the rail, or in the form of rail breakage in

the winter when the track is in tension in the rolling direction of the wheels. To reduce or eliminate the likelihood of track buckling, it is installed and maintained in tension. There exist many studies on the effect of temperature change on track buckling and fracture. Although there exists some scatter, anecdotal data on the seasonality of RCF (showing it to be more prevalent in cold seasons), the effect of temperature change on RCF has not been studied in any great detail. In the next section, we study the effect of temperature change on RCF.

2.4. **Results and discussion**

In this section, we study the effects of temperature change, traction coefficient and grain size on RCF. In order to have accurate results, we need to be sure that damage increment (ΔD_f) introduced in Equation (2-13) is small enough. The value of ΔD_f is a tradeoff between simulation time and accuracy. Doubling the damage increment will approximately double the computation time. To study the sensitivity of results to this parameter, several ΔD_f values are compared together in a model with zero traction coefficient. To track the overall damage in the structure, at each cycle the damage is averaged in all cohesive elements with the following equation [137]

$$D = \frac{1}{A}\sum_{i=1}^{n} D_i \, A_i \tag{2-22}$$

where n is the number of cohesive elements in RVE, A_i is the area of each cohesive element, and A is the total area of cohesive elements. RCF life is obtained when the averaged damage has an infinite slope in damage versus life plots, and damage propagation becomes unstable in the structure. This condition is usually achieved when the finite element simulation diverges. Values of 0.1 and 0.2 for ΔD_f are used in [11] and high accuracy was achieved. So values of 0.05, 0.1, 0.2 and 0.4 are selected here. RCF induced damage versus life (number of cycles leading to damage) is shown in Fig. 2-5 for different ΔD_f values.

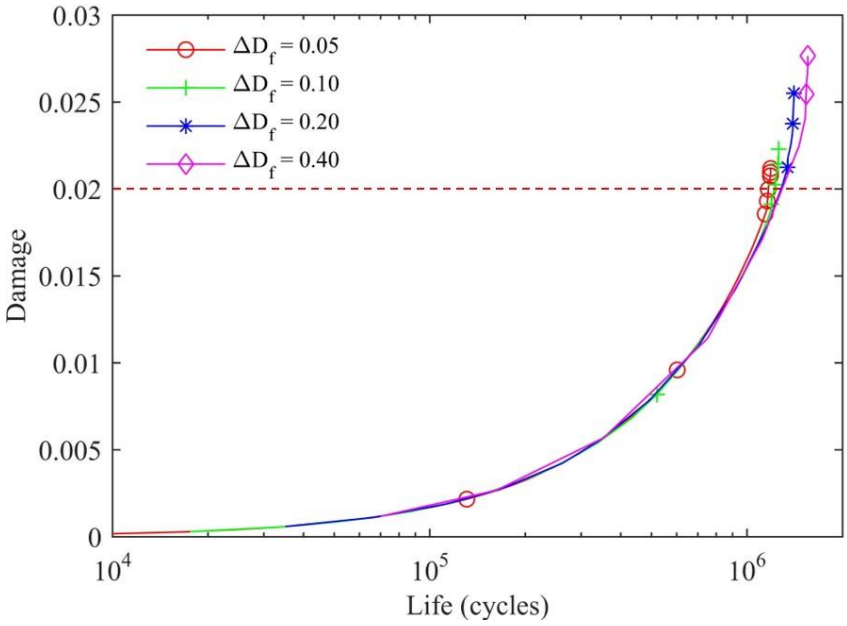

Fig. 2-5. Damage-Life plot for studying the sensitivity of results to fatigue damage increment (ΔD_f)

The figure shows that results converge with damage increment decrease. Considering $\Delta D_f = 0.05$ as an accurate and reliable value, if we compare life for different damage increment at average damage of 0.02, there is 4%, 11%, 12% error for 0.1, 0.2 and 0.4 damage increments, respectively. So we used $\Delta D_f = 0.1$ for all the simulation as a reliable and time-efficient value.

2.4.1. Temperature effect

Longitudinal displacements due to the temperature change can be calculated from

$$\Delta L = L\,\alpha\,(T_N - T_R) \tag{2-23}$$

which L is the initial length, α is the thermal expansion coefficient in "$\frac{1}{°C}$", T_R and T_N are rail temperature and neutral temperature in "°C", respectively. To study the effect of changing temperature on RCF, using the periodic boundary conditions, ΔL (representing the longitudinal displacement due to temperature change) is applied to the model by

$$u_a^i - u_b^i - \Delta L = 0. \tag{2-24}$$

To study the effect of temperature change on RCF of rails during different seasons, a model with the microstructure shown in Fig. 2-3 is used. The traction coefficient is considered zero in temperature effect study. Different rail temperature changes, which are considered with respect to the neutral temperature, are applied to the model as explained in section 2.3.4. Since temperature difference is present in Equation (2-23), the rail temperature (T_R) is assumed as a function of neutral temperature (T_N) from $T_N - 40$ to $T_N + 40$. Therefore, temperature difference in Equation (2-23) is between -40 to $+40$. RCF induced damage versus life are shown in Fig. 2-6 for multiple temperatures above and below the neutral temperature. In Fig. 2-6b, the dashed line is the damage-life plot for neutral temperature. By increasing the temperature, damage does not change much; however, when there is a temperature decrease, damage in cohesive elements increases and the structure reaches its final failure sooner. Figure 6 depicts the RCF life for different temperatures, showing that life is almost constant at high temperatures, mainly due to higher compressive stresses. At higher compressions, the crack faces are compressed together, and the first mode of fracture (opening mode) is suppressed. Only the second mode of fracture (sliding mode) is active because of rolling contact loads, therefore the life remains constant. Conversely, when temperature decreases with respect to the neutral temperature, RCF life significantly decreases. This phenomenon is attributed to the presence of higher tension and the first mode of fracture becoming more active, while the second mode is already active in the subsurface because of the rolling contact load. Based on these results, different crack patterns at high and low temperatures are expected.

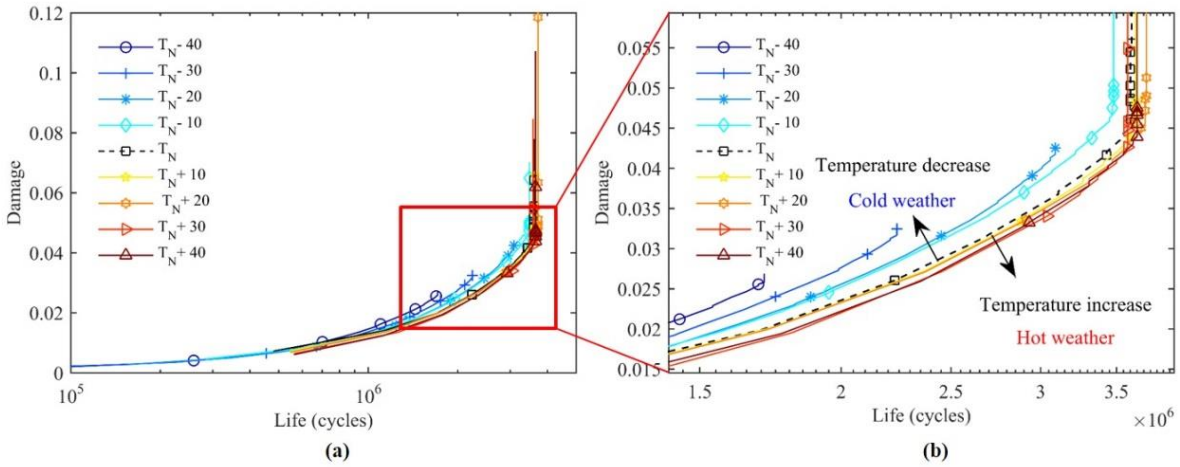

Fig. 2-6. (a) Damage-Life curve to study temperature effect on RCF for different temperature changes from neutral temperature (T_N) (Traction coefficient is zero), (b) A magnified section of (a) with more details that shows by increasing the temperature from neutral temperature (dashed line) no remarkable change in RCF occurs but when temperature decreases, the life considerably decreases.

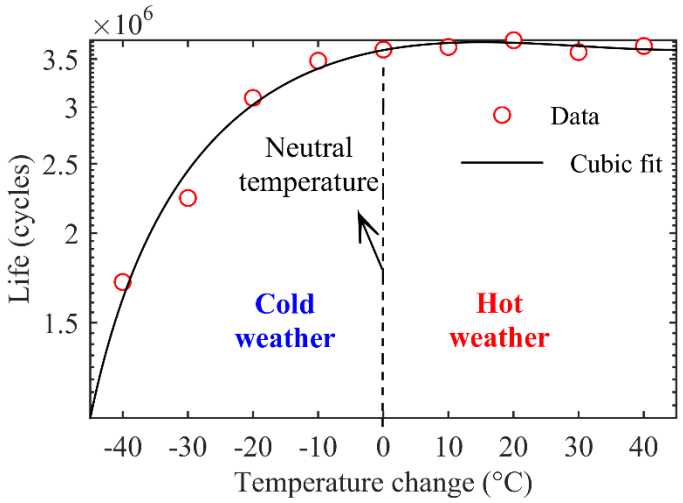

Fig. 2-7. The effect of temperature on RCF life. Decreasing the temperature significantly reduces rail life, while temperature increase does not have a considerable effect on the RCF life of the rail.

Crack patterns of the failed structure of the model with the highest temperature ($T_N + 40$℃) and the model with the lowest temperature ($T_N - 40$℃) are depicted in Fig. 2-8a and Fig. 2-8b, respectively. In RCF studies, the subsurface cracks are found to be at the place of maximum shear stress below the surface [12]. In Fig. 2-8a, cracks are observed under the surface, where the

shear stress is maximum. Due to compressive loads on top of the contact patch and along the periodic boundaries, only the second mode is active and cracks form only under the surface where the shear stress is maximum. Two kinds of crack are observed in Fig. 2-8b, which corresponds to a low-temperature condition crack pattern. The first type is shear dominated cracks that are developed under the surface in the place of maximum shear. The second type is surface-initiated cracks, which are formed due to tensile stresses of low-temperature conditions.

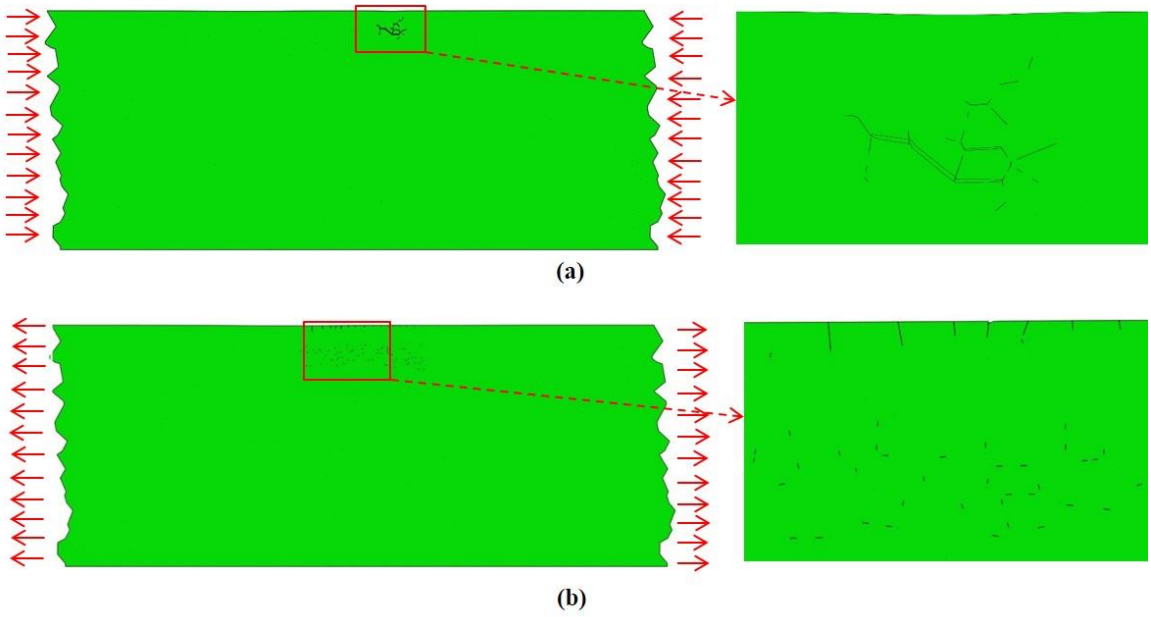

Fig. 2-8. (a) Subsurface crack pattern in high temperature ($T_N + 40$ ℃) condition, where cracks form under the surface. (b) Cracks are present both in the subsurface and on the surface in low-temperature condition ($T_N - 40$ ℃). T_N is the neutral temperature.

It is determined that RCF is more damaging in cold weathers specially when there are other influencing factors, such as increased steel brittleness and presence of freeze-thaw cycle of moisture in the cracks [138]. This is in accordance with the finding of Zerbst et al. [139]. They stated that in Britain, whilst the number of failures in wheel and axles has been decreased during the last century, the number of rail failures per train kilometer has increased. They attributed this to higher loads and thermal stresses in continuous rails due to low ambient temperatures. With measuring stress intensity factors in different days in actual track, they found that tensile stresses are highly substantial for fatigue crack propagation in cold winter days. Due to high probability of fracture at beginning of winter, they highly recommended to inspect the rail in late autumn.

2.4.2. Traction coefficient effect

In this section, different traction coefficients are considered to find out how the traction coefficient affects RCF in the rail. There is a range for an appropriate amount of traction between wheel and rail. If the traction coefficient is too low, it reduces the traction and braking rates of the train, and if the traction coefficient is greater than about 0.4, it will cause surface damage of wheels and rails.

In the beginning, no traction is considered, implying that the wheel freely rolls on the rail with no traction forces. The Jiang-Sehitoglu fatigue damage evolution law, used in this study, considers all shear and normal stresses, as well as shear and normal strains. In the free-rolling case, the effect of shear stress and strain is more remarkable, because normal stresses are mostly compressive, and both cohesive static damage model and fatigue damage evolution law do not consider the compressive stresses due to their crack closure effect. Also in RCF studies, most of the subsurface cracks initiate from the position of maximum shear stress, which is slightly under the surface [12]. The contour plot of shear stress due to the normal Hertzian load is shown in Fig. 2-9a. The figure shows that maximum shear stress happens under the surface. So it is expected that cracks initiate under the surface where shear stress is maximum. Shown in Fig. 2-9b is a plot of damage versus life for free-rolling condition. The damage, which is the average damage of cohesive elements in RVE, increases by increasing the number of cycles until the model reaches its final failure. The propagation of cracks and shear stresses around the cracks for different stages (A, B, C, and D) are illustrated in Fig. 2-9c. First cracks initiate slightly below the surface, and further loading will cause the cracks to propagate until the structure fails.

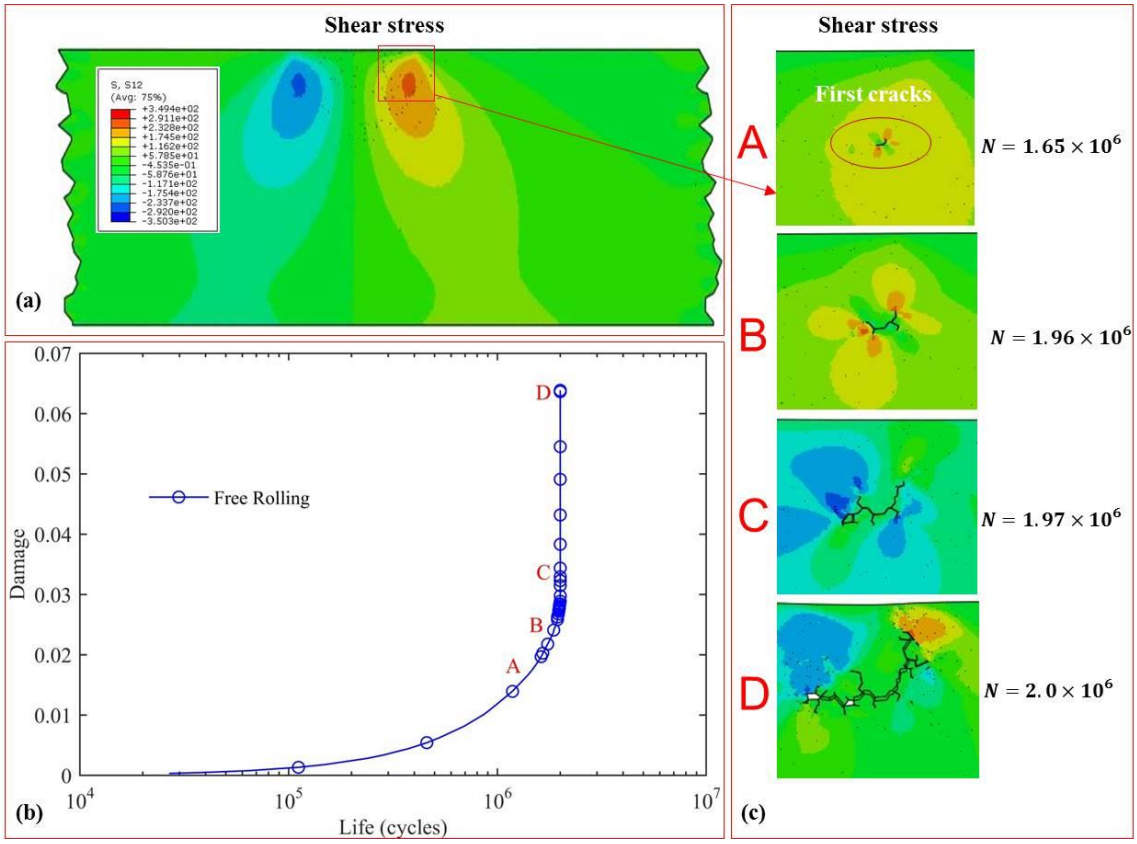

Fig. 2-9. (a) Shear stress contour for free-rolling condition indicates that maximum shear stress occurs under the surface. (b) Damage-life plot for free-rolling condition shows an infinite slope of damage that means the structure is failed. (c) Crack propagation for different cycles is shown in the shear stress contour for four different stages of damage evolution (points A, B, C, and D in (b))

After studying the free-rolling condition, different traction coefficients are studied for two cases: braking and acceleration. During braking, the traction forces act in the same direction of the wheels' motion on the rail. During acceleration the opposite happens, meaning that the accelerating forces act in the opposite direction of the wheels' motion on the rail. Both acceleration and braking studies are performed in the same domain.

The damage-life plots for braking and accelerating cases are shown in Fig. 2-10. Increasing the traction coefficient up to 0.5 significantly decreased the final RCF life. In cases with a higher traction coefficient, Fig. 2-10 shows a lower amount of averaged damage in the structure compared to the lower traction coefficient plot. Due to higher tangential forces, the structure has more surface damage, and the FEM solution becomes unstable in the presence of surface

damage. However, the predicted life is the final life since the slope of damage-life curve moves toward infinity and no further life remains. Also, it is worth mentioning the damage in Fig. 2-10 is the averaged damage in cohesive elements, and since only some of the elements are failed, the average damage value is small. Similar results are obtained by Onal et al. [124] from the simulation of the RCF behavior of the pearlitic and bainitic rail steels. Also, Ma et al. [140] stated that due to tangential forces, higher traction coefficients accelerate the initiation of RCF cracks. This clearly indicates the importance of including the traction dynamics in RCF studies, as has been done in this study. Although the braking and accelerating conditions seem to have the same results for a specific traction coefficient, they have some differences, which are represented in Fig. 2-11.

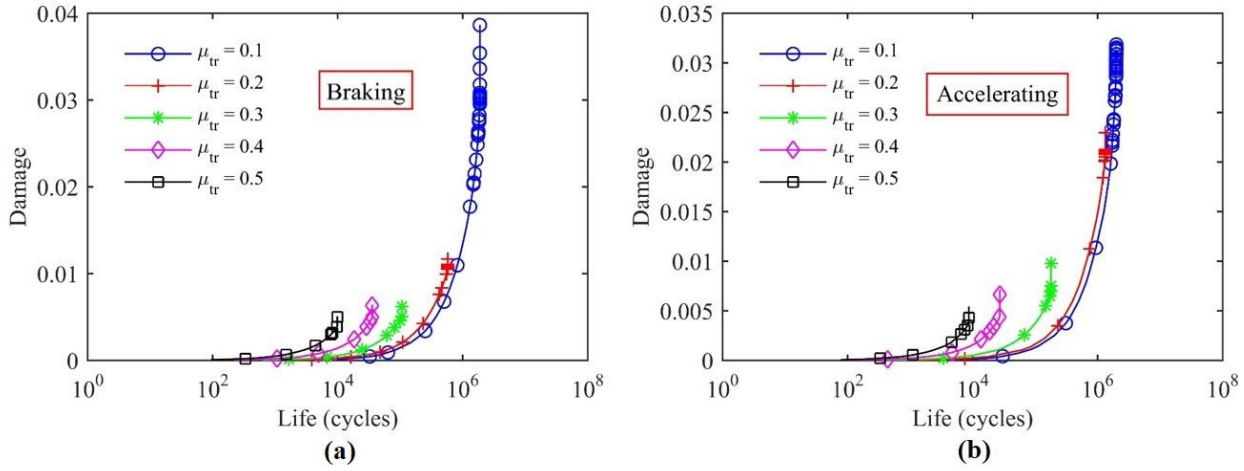

Fig. 2-10. Damage-life plot for different traction coefficients of two cases (a) braking and (b) accelerating, show that increasing the traction coefficient, significantly decreases the rail life.

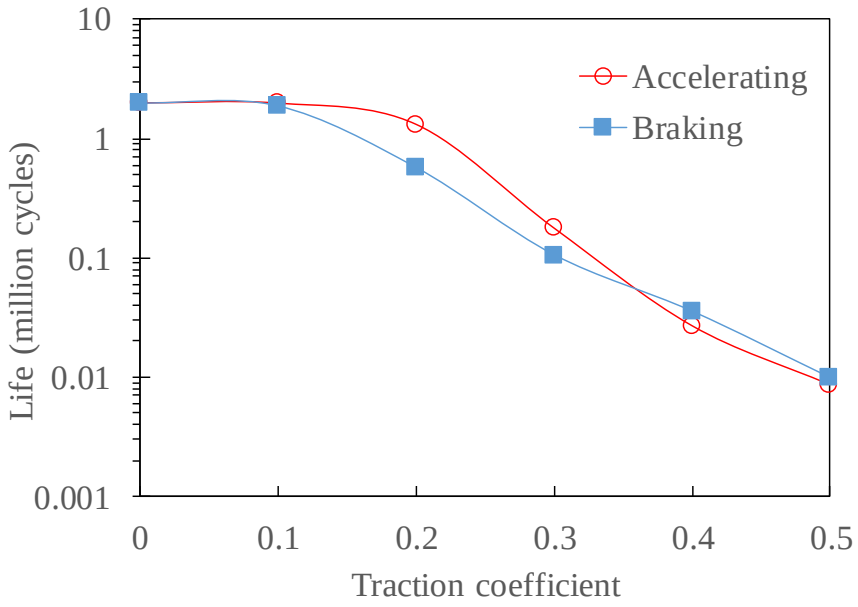

Fig. 2-11. Comparison of RCF life for different traction coefficients for accelerating and braking cases indicates that in lower traction coefficients braking is more detrimental while in higher traction coefficients, accelerating is more damaging to the rail life.

Fig. 2-11 indicates that at lower tractions braking is more damaging than accelerating, and it leads to lower RCF life. At high tractions, however, accelerating forces are more damaging than braking.

Magel [2] states that in lubricated surfaces (very low friction coefficients) the subsurface cracks can form in the place of maximum shear stress. Also by looking at the shakedown map [141], for low traction coefficients ($\mu_{tr} < 0.3$), material flow happens under the surface, and for high traction coefficients ($\mu_{tr} > 0.3$) the material flows on the surface. The value of $\mu_{tr} = 0.3$ is an approximate value and changes slightly for elastic and plastic deformations. The effect of the traction coefficient on the position of micro-cracks is predicted by the current model. Fig. 2-12 shows crack morphologies in shear stress contour for different traction coefficients (traction loads are in the opposite direction of rolling).

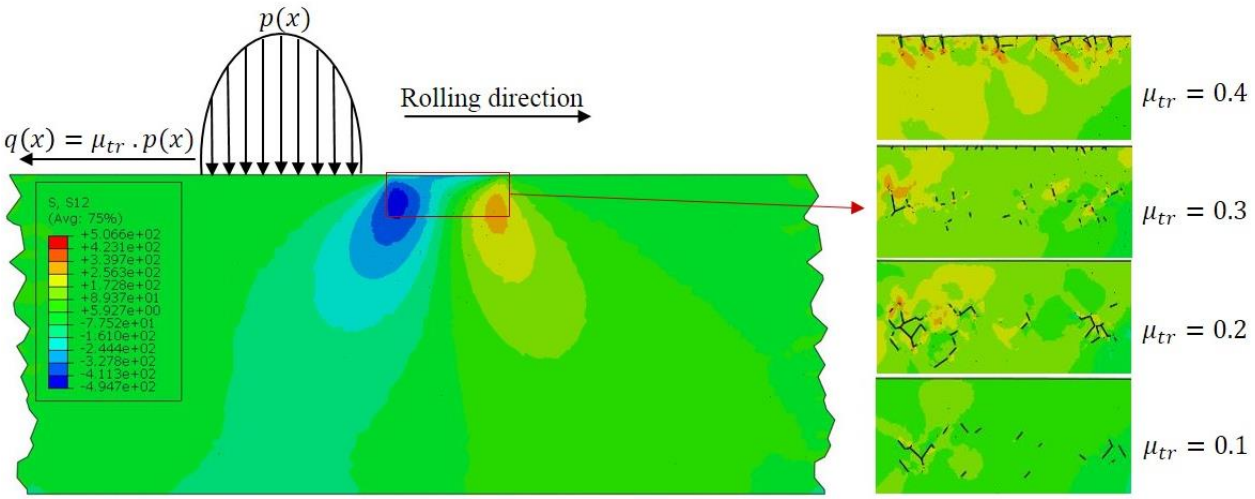

Fig. 2-12. Micro-cracks pattern for different traction coefficients. Micro-cracks form in the subsurface for lower traction coefficients and moves toward the surface for higher traction coefficients.

The results show with increasing μ_{tr} from 0.1 to 0.4, cracks move toward the surface. For $\mu_{tr} = 0.1$ and $\mu_{tr} = 0.2$ cracks form under the surface. For $\mu_{tr} = 0.3$, some of the cracks form on the surface and some of them initiate under the surface. By increasing μ_{tr} to 0.4, all the cracks form on the surface. This change happens since maximum shear stress moves toward the surface by increasing the traction coefficient. The model is able to see this effect perfectly. This observed behavior in the computational simulations is also studied by Ma et al. [140], and several surface cracks and spalling are observed for high traction coefficients.

2.4.3. Grain size strengthening effect

In this section, the effect of grain size change on RCF is studied. Voronoi geometries with different average RVE grain sizes are created. RVE of these geometries with different grain sizes are magnified in Fig. 2-13. Equivalent diameter of a circle with the same area of the grain is considered as the grain size. The average grain sizes in RVEs are 60, 45, 30, and 20 μm. The grain size distribution in the RVE of each geometry is shown in Fig. 2-14. It is observed that the grain sizes in RVEs are following a normal distribution, which is in agreement with the distribution of grain sizes in experimentally observed microstructures.

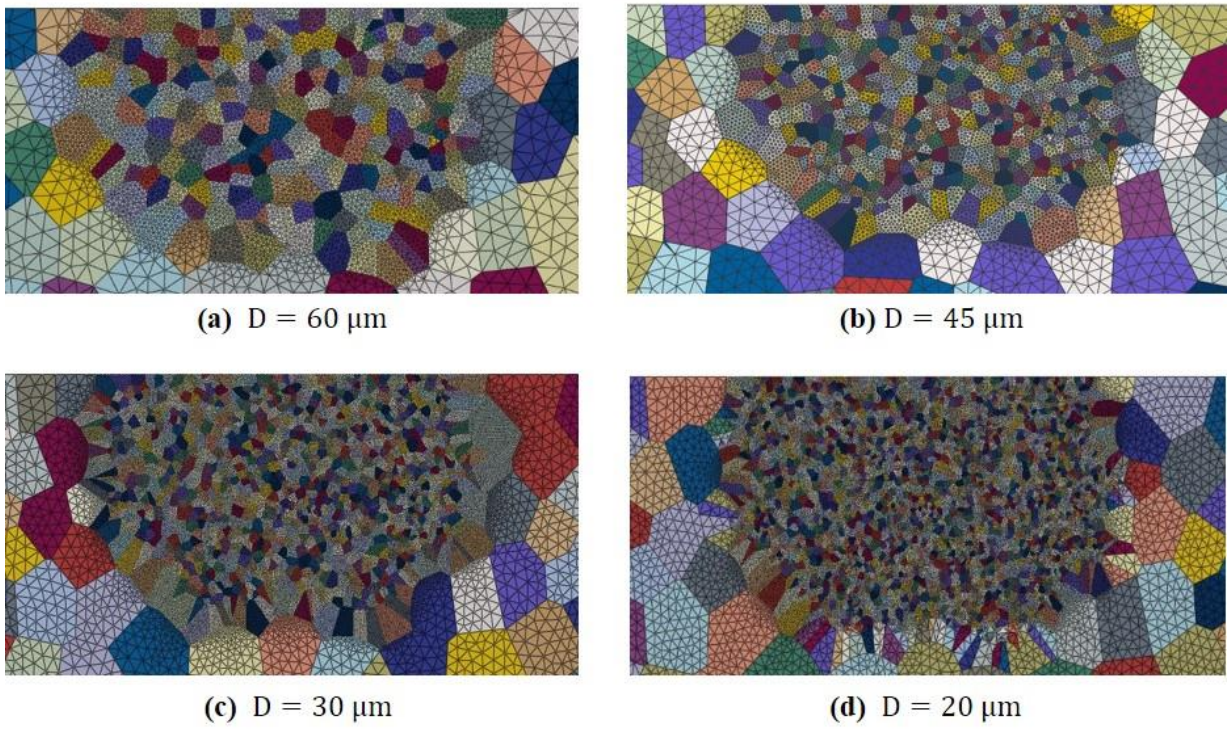

Fig. 2-13. RVE of four different geometries are shown in (a) to (d) with average grain sizes of 60, 45, 30, and 20 μm, respectively. These geometries are created to study the grain size effect on RCF.

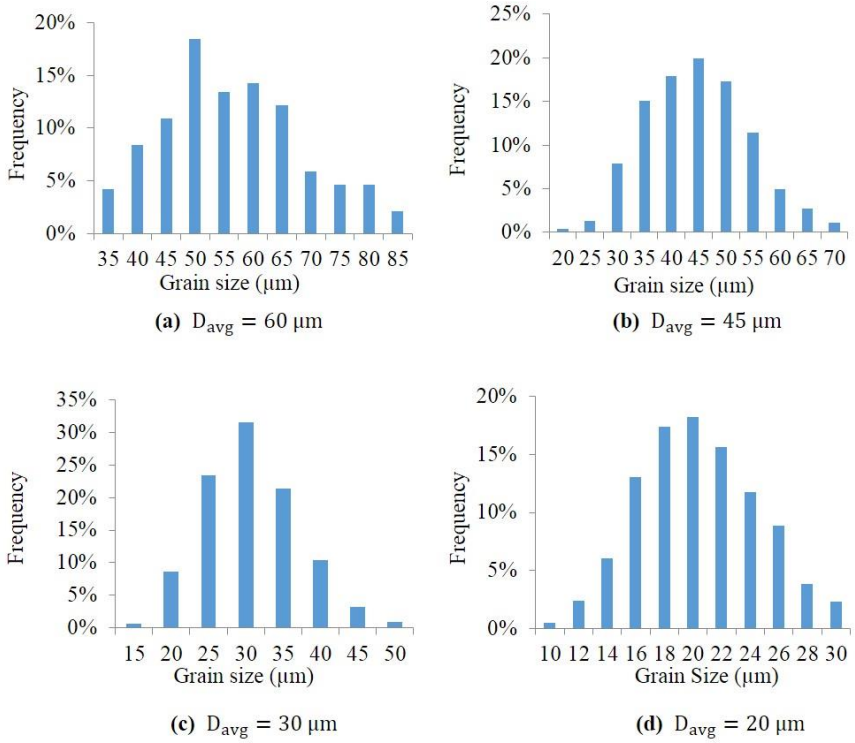

Fig. 2-14. Grain size distribution in the RVE of four different geometries. The grain sizes are following a normal distribution, which is in agreement with experimentally observed microstructures.

Initially, same yield strength ($\sigma_y = 700\ MPa$) assigned to all of models with different grain sizes. The results of damage-life plots showed a very small increase in life by decreasing the grain size. In theory, decreasing the grain size will increase the grain boundary area which leads to higher strength, since dislocations have less area to move and they pile up at grain boundaries. However, the current model cannot see dislocation interaction with grain boundaries and this causes similar results for different grain sizes. Since changing grain sizes leads to yield strength change, this effect is implemented in the model by changing the yield strength of both grains and grain boundaries based on Equation (2-25).

Based on the experimentally reported results, decreasing the grain size (up to a critical size, which is in the order of tens of nanometers) in polycrystals increases the yield strength. This behavior is known as the Hall-Petch effect, and it has been shown that the change of yield stress with decreasing the grain size can be expressed by [142]

$$\sigma = \sigma_0 + \frac{k_{HP}}{\sqrt{d}} \tag{2-25}$$

where σ is the yield stress, d is the grain size, and σ_0 and k_{HP} are material constants. In pearlitic steels, yield strength depends on interlamellar spacing, pearlite colony size, and prior-austenite grain size [143]. The most important factor is interlamellar spacing which will be a future research subject by the authors. These factors are not considered in this study, and a simple Hall-Petch equation for steel is used to study the effect of grain size and grain boundaries on RCF. Hall-Petch constants ($\sigma_0 = 450\ MPa$ and $k_{HP} = 53\ MPa.mm^{0.5}$) of mild steel [142] are used in this section as a case study. Calculated yield strengths are 666, 700, 755 and 825 MPa for 60, 45, 30, and 20 μm grain sizes, respectively. The goal is to find out how changing the yield strength and grain size affects the RCF.

Damage versus the life of four different grain size is plotted in Fig. 2-15. The figure shows that decreasing the grain size improves RCF life. This is in agreement with experimental fatigue data of ferritic-pearlitic steel [144] stating that fatigue resistance improves with the grain size refinement. It is worth noting that the grain size can be changed in practice by a broad range of

post-processing methods, including heat treatments and rolling. The developed computational model can be used as a basis for studying fundamental mechanisms of RCF, which can be considered as a first step to use computational models as a guide to design appropriate processing steps to improve the RCF life of rails.

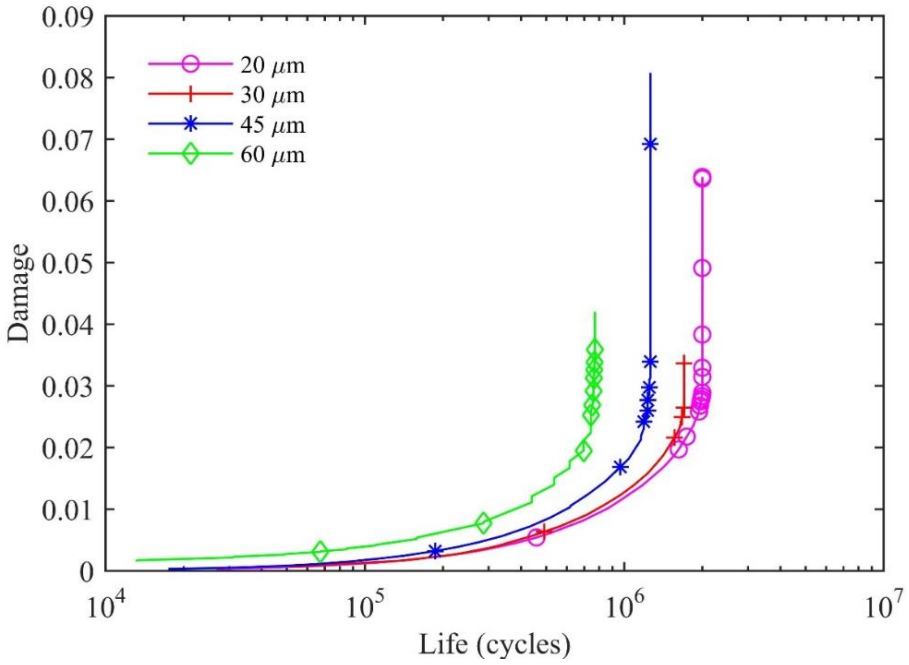

Fig. 2-15. Damage-life plots for different grain sizes indicate that refinement of grain size increases the rail life.

2.4.4. Effect of maximum contact pressure

The effect of maximum contact pressure ($p_{\max}$)on RCF is studied by many researchers [124, 145], and it is found that a power-law function between RCF life and p_{max} exists. Su et al. [145] investigated the behavior of different rail steels under different contact conditions with a twin-disk machine. The RCF life is described by

$$\text{RCF life} = A\,(p_{max})^{B}. \tag{2-26}$$

They stated that the power index (B) can be in the range of -1 to the -14.5 for different contact conditions. A similar case is studied with the developed model to compare with the results obtained from the above-mentioned work. The traction coefficient is $\mu_{tr} = 0.25$, and material is pearlitic rail steel STD (standard carbon). Yield strength and ultimate tensile strength for the rail

steel are 538 and 1034 MPa, respectively. The same properties are used in our model to compare the results with the experiment. The results are presented in Fig. 2-16.

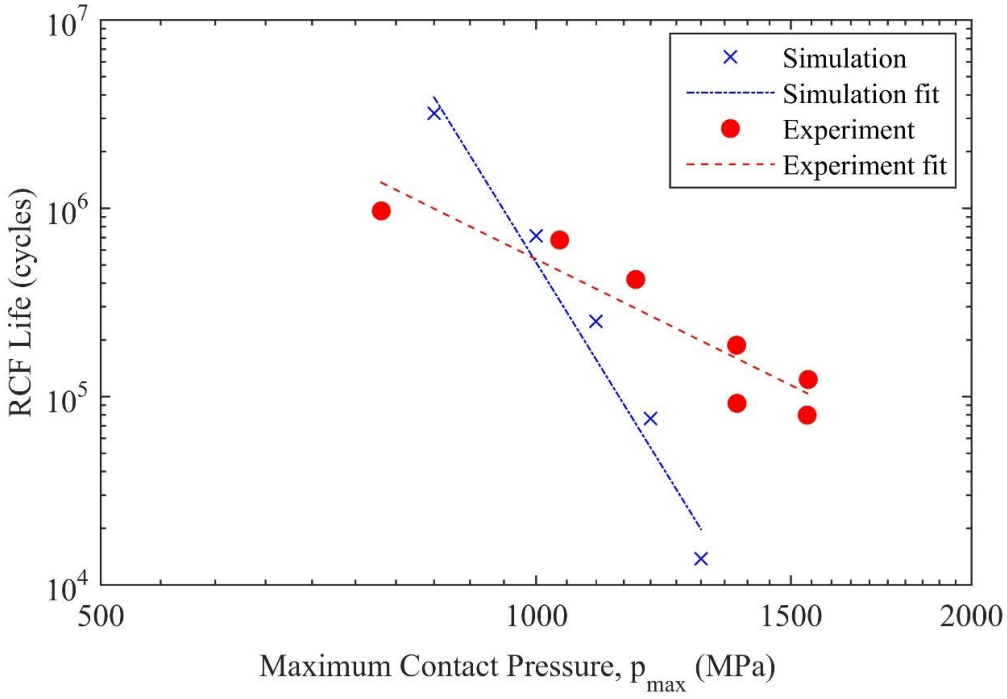

Fig. 2-16. Comparison of RCF life of the current model and experimental results [145] for different maximum contact pressures. See text for details of the comparison between computational and experimental results, and also the origins of observed differences.

The simulation shows a power relation between RCF life and maximum contact pressure, which is in agreement with previous findings [124, 145]. The simulation fit result shows a slope of -10.39 which is in the range of -1 to -14.5 [145]. However, the simulation fit has a steeper slope (-10.39) compared to the experiment fit slope (-4.67). The model predicts low RCF life in high contact pressures. It can be attributed to the fact that the criterion of RCF failure is different. In the experiment, loss of surface material as spalling or collapse of the surface is used to determine RCF life. Some of the cracks form in the subsurface and cannot be detected during the experiment. These subsurface cracks can form an extensive crack network under the surface but never cause a spalling [146] (like Fig. 2-17b). So, this leads to higher RCF life in experiments, since the simulation considers cracks in all regions, and calculated RCF life is more conservative than experiments in high contact pressures.

2.4.5. Comparison with experimental observations

The use of cohesive elements helps to find out the position of micro-cracks and the amount of damage in them, and compare the results for different cases. This method does not simulate only one crack and propagation of that crack, instead, it shows a system of micro-cracks between the grains in the rail microstructure. Cracks can initiate from surface or subsurface depending on loading and surface parameters [147]. The surface cracks are believed to form due to the accumulation of damage and repeated plastic deformation on the railhead surface. The crack direction is dependent on the direction of the deformed microstructure caused by traction and normal forces in the contact patch [148]. When the rail is very well lubricated and the coefficient of friction is low, subsurface shear stress can be very high. This high shear stress and the possible metallurgical defect can lead to subsurface cracks [2]. When the micro-cracks join together, they form a crack pattern. If these cracks remain undetected, there is the risk of rail break and derailment specially when residual tensile stress (due to thermal stresses in cold weather) is present in the rail. Thermal and bending stresses increase crack propagation rates and can result in crack branching downwards [147].

Crack patterns from our model are compared to experimental observations from [149], and the results are illustrated in Fig. 2-17a. Since no details on the microstructure in the experiment are available and randomness happens in fatigue testing, we don't expect to have exactly the same results. The experiment is performed by twin disk rolling-sliding testing machine and has maximum contact pressure $p_{max} = 1500\ MPa$, contact half width $b = 359\ \mu m$ and traction coefficient $\mu_{tr} = 0.14$. The material is bainitic roll steel, and no other specific properties are provided. The same loading parameters in this experiment are used in the simulation, and previous rail steel properties are used for material properties.

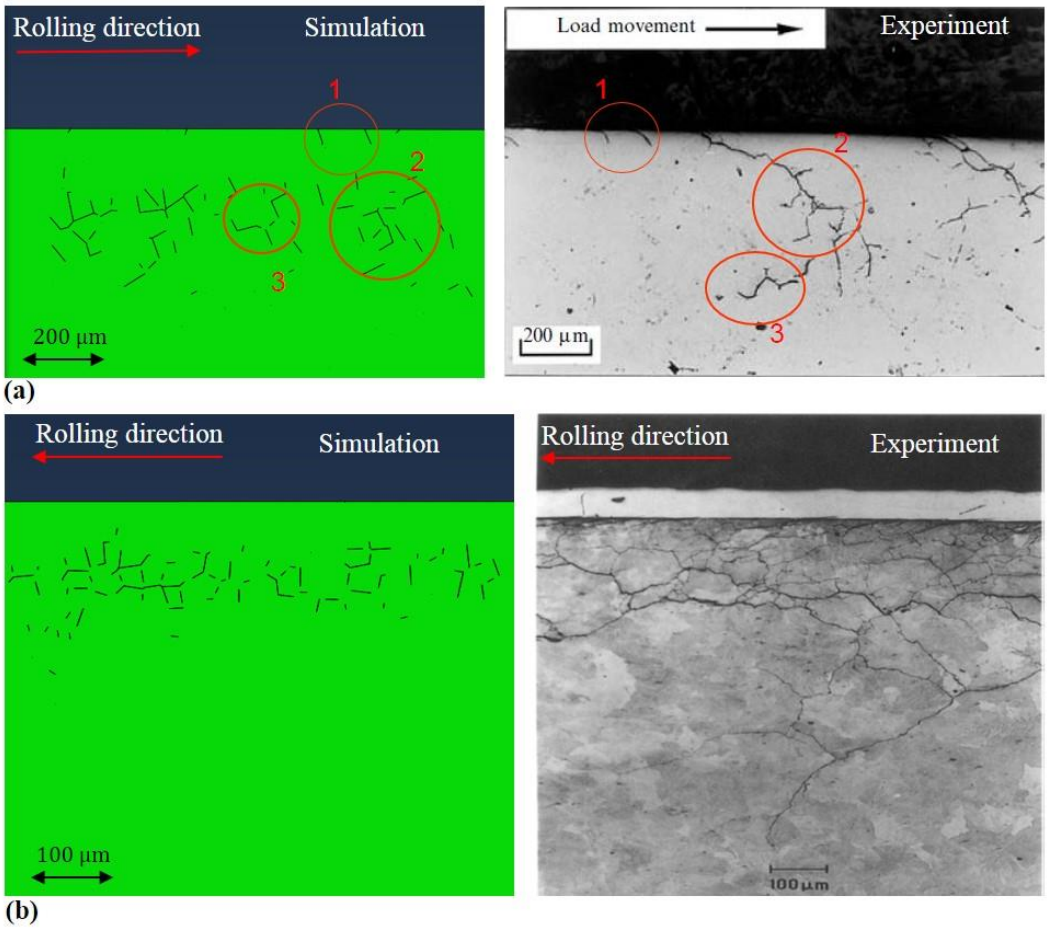

Fig. 2-17. Micro-crack pattern compared for current model and experimental observations (a) [149] and (b) [146]. The results show some similarities between crack patterns from simulations and experiments, and the model predicts near the same depth for the micro-cracks.

As shown in Fig. 2-17a, the crack pattern from experiments and simulation have some similarities. The subsurface cracks form near the same depth, and interact with each other and create a network of micro-cracks. Also, surface cracks, which form due to plastic deformation and high contact loads, can join the subsurface cracks and peel off a part of the surface layer and lead to spalling.

Another comparison is made between simulation and experimental observation of pearlitic rail steel. The experiment [146] is done with a twin-disk machine and has maximum contact pressure $p_{max} = 1500\,MPa$, contact half width $b = 107\,\mu m$ and traction coefficient $\mu_{tr} = 0.10$. The

results are illustrated in Fig. 2-17b and show a similar network of subsurface micro-cracks in both experiment and simulation.

2.5. **Conclusions**

A microstructural-based computational framework is developed for studying the rolling contact fatigue (RCF) in rail materials. To construct a realistic geometry, Voronoi tessellation is employed to create a 2D microstructure of the contact patch of wheel and rail, and cohesive elements are applied between grains as grain boundaries. Instead of moving the wheel on the rail, a moving Hertzian load is applied to the rail surface. The jump-in-cycles approach is implemented in Abaqus through subroutines to efficiently simulate a large number of loading cycles, while material degradation at the grain boundaries with increasing the number of cycles is simulated by using Jiang-Sehitoglu damage evolution law. With the developed framework, RCF in rail in different conditions is studied. The results show that increasing temperature above the neutral temperature does not have a significant effect on RCF, while decreasing the temperature decreases RCF life, and can significantly accelerate rail damage. The effect of the traction coefficient on RCF is also studied. The results indicate that large traction forces at the wheel-rail interface considerably accelerate RCF growth, and micro-cracks migrate from subsurface to the surface of the rail. To study the effect of grain sizes on RCF, geometries with different grain sizes were created and using the Hall-Petch relation, the material properties were calibrated for each model. It is approved that by decreasing the grain sizes, RCF life increases and a lower amount of damage accumulates in the material. Studying the maximum contact pressure effect on RCF shows that there is a power relation between RCF life and maximum contact pressure, which matches previous findings in the literature. Several cases are also simulated and compared with experiments in the literature, and it is observed that the crack pattern and depth are in close agreement with experimental observations.

Chapter 3

3. Three-dimensional analysis of rolling contact fatigue using crystal plasticity finite element method and cohesive zone modeling

3.1. Overview

In this chapter, a three-dimensional (3D) finite element model that includes the microstructure of grains and grain boundaries is developed for studying the rolling contact fatigue (RCF) damage caused by a rolling steel wheel on a steel railway. The 3D model uses a crystal plasticity-based micromechanical framework for simulation of stress-strain behavior inside the grains, and cohesive elements with traction-separation law for modeling the intergranular fatigue damages. A combination of moving normal Hertzian load and tangential loads are employed to mimic the rolling contact conditions. The effect of various parameters such as friction coefficient, traction, partial slip contact and wheel load on RCF is studied. The results reveal that RCF cracks initiate slightly below the surface for large wheel loads and low tractions. The cracks migrate toward the surface as the wheel-rail traction increases. For high tractions, the cracks initiate at the rolling surface. Under partial slip contact condition, there is a large change in rail life for small normalized tractions. With a slight increase in the latter, the rail life significantly decreases. For moderate to large tractions, rail life remains relatively unchanged or slightly increases. The results of the study appear to agree with anecdotal observations by the U.S. railroads from the revenue service operation.

3.2. Material and methods

Manganese rail steel (Hadfield steel) is selected for this study. This alloy is used in the frogs and diamond crossings along railways [37, 150]. This austenitic steel has a face-centered cubic (FCC) crystal structure, and grains/grain boundaries are clearly visible under the optical microscope. This material shows a good combination of high toughness, resistance to wear, and

heavy impact loadings [150]. The monotonic stress-strain curve and rolling contact fatigue damage properties for this alloy are obtained from the literature [37, 150].

Two different material models for grains and grain boundaries are employed in our model. Crystal plasticity is used for bulk grains, and traction-separation law with fatigue damage is utilized for grain boundaries. Fig. 3-1 illustrates these material models, and more details are provided in the following sections.

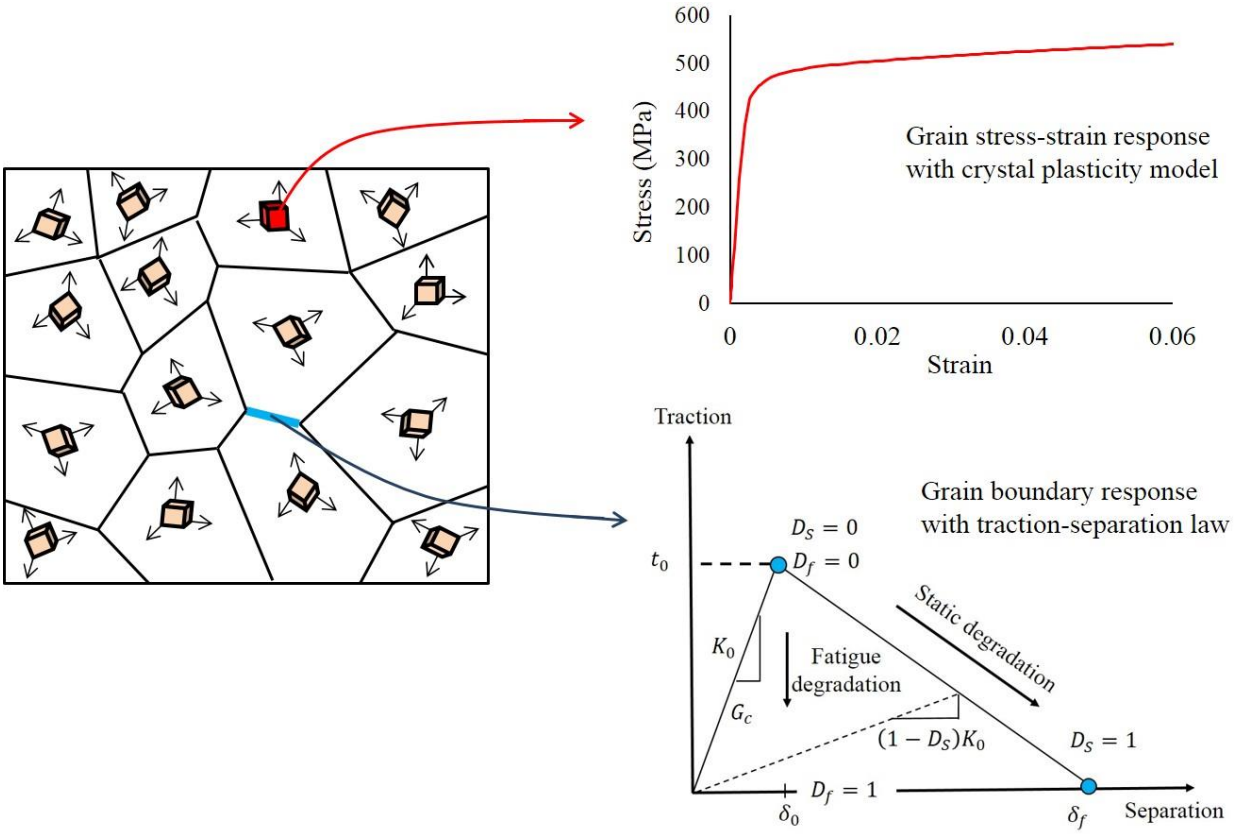

Fig. 3-1. Schematic of models for defining material behavior. Crystal plasticity material model is used to define stress-strain behavior of grains, and traction-separation law with fatigue degradation is utilized to simulate grain boundary behavior.

3.2.1. Crystal plasticity model

A rate-dependent single crystal plasticity model developed by Hill [151], Rice [152], and Asaro [153] is used for studying the material response of bulk grains to the deformation caused by rolling contact. Crystal plasticity is a precise model to study the effect of microstructure on the mechanical behavior of materials and is widely utilized by other researchers. This constitutive

model assumes that plastic deformation occurs because of the dislocation movement on a specific set of slip planes. Each slip system, α, is specified by combining a slip plane (with normal of m^{α}) and a slip direction (s^{α}). The total deformation gradient F is defined by

$$F = F^{*}F^{p} \tag{3-1}$$

where, F^{*} denotes elastic stretch and rotation of crystal lattice, and F^{p} refers to the plastic shear of material. The rate of change of F^{P} (denoted as L^{p}) is given by

$$L^{p} = \dot{F^{p}}(F^{p})^{-1} = \sum_{\alpha} \dot{\gamma}^{\alpha} s_{i}^{\alpha}\, m_{j}{}^{\alpha} \tag{3-2}$$

where, $\dot{\gamma}^{\alpha}$ is the slipping rate of the α slip system. The resolved shear stress τ on the α slip system is defined by

$$\tau^{\alpha} = s_{i}^{\alpha}\, \sigma_{ij}\, m_{j}^{\alpha} \tag{3-3}$$

The slipping rate $\dot{\gamma}^{\alpha}$ of α slip system is defined based on the Schmid law by a power-law expression as

$$\dot{\gamma}^{\alpha} = \dot{\gamma_{0}}{}^{\alpha}\, sign\,(\tau^{\alpha}) \left|\frac{\tau^{\alpha}}{g^{\alpha}}\right|^{n} \tag{3-4}$$

where g^{α} defines the current strength of α system, $\dot{\gamma_{0}}{}^{\alpha}$ is the reference slipping rate, and n is the strain rate sensitivity ratio. In the systems where slip happens, the resolved shear stress τ^{α} on the active slip system ($\dot{\gamma}^{\alpha} > 0$) attains a critical value g^{α}. On the inactive slip systems with $\dot{\gamma}^{\alpha} = 0$, the resolved shear stress τ^{α} does not exceed g^{α}. The hardening law for the current strength g^{α} is given by

$$\dot{g}^{\alpha} = \sum_{\beta} h_{\alpha\beta}\, \dot{\gamma}^{\beta} \tag{3-5}$$

where, $h_{\alpha\beta}$ are the slip hardening moduli. $h_{\alpha\alpha}$ (no summation on α) and $h_{\alpha\beta}$ ($\alpha \neq \beta$) are called self-hardening and latent hardening moduli, respectively. These moduli used by Peirce [154] are given as

$$h_{\alpha\alpha} = h(\gamma) = h_0 \operatorname{sech}^2 \left|\frac{h_0 \gamma}{\tau_s - \tau_0}\right| \text{ (no sum on } \alpha) \quad (3\text{-}6)$$

$$h_{\alpha\beta} = q\, h(\gamma) \quad \alpha \neq \beta \quad (3\text{-}7)$$

where, h_0 is the initial hardening modulus, τ_s is the saturation stress, and τ_0 is the initial stress. γ is the accumulated shear strain in slip systems, and q is the latent-hardening to self-hardening ratio. The above described constitutive model is previously implemented into a user-defined material subroutine (UMAT) by Huang [155]. This UMAT is employed in this research properly. Crystal plasticity parameters are calibrated with the macro-scale tension test results, as will be discussed in the following sections.

3.2.2. Static and fatigue damage in grain boundaries

Grain boundaries are assumed the regions of damage initiation and evolution in this research. In order to implement damage criteria to the model, cohesive elements are utilized similar to the 2D analysis by the same authors [156] with traction-separation law for static damage, and Jiang-Sehitoglu damage evolution law for fatigue damage. A few changes are applied to the model, as described next.

3.2.2.1. Traction-separation law

A new form of damage initiation and evolution for traction separation law is used in the 3D analysis compared to 2D analysis [156]. For damage initiation modeling in cohesive elements, the maximum nominal stress criterion is applied (Equation (3-8)). In this criterion, it is assumed that pure modes of shear or tension may cause damage initiation as defined by

$$Max\left\{\frac{\langle t_n \rangle}{t_n^0}, \frac{t_s}{t_s^0}, \frac{t_t}{t_t^0}\right\} = 1 \quad (3\text{-}8)$$

where, ${t_n}^0$, ${t_s}^0$ and ${t_t}^0$ are material parameters representing the critical values for damage initiation in pure tension and shear loading, respectively. t_n is the normal traction, and t_s and t_t are the first and second shear tractions according to a local coordinate system. Static damage evolution law is utilized the same as 2D analysis [156]. Critical shear and normal displacements are considered equal ($\delta_n^0 = \delta_s^0 = \delta_t^0$), while shear and normal stiffness are related by [122]

$$E_{ss} = E_{tt} = \frac{E_{nn}}{2(1+\nu)} \tag{3-9}$$

Critical fracture energy and maximum traction in both normal and shear directions follow the same relation as Equation (3-9). More details about traction-separation laws are provided in [120].

3.2.2.2. Modifying the fatigue parameter (FP)

In the 3D analysis, cohesive elements have two shear components (t_s, t_t or $\varepsilon_s, \varepsilon_t$), and in 2D analysis, only one of them is applicable (t_s or ε_s). As described in [156], a multi-axial energy-based fatigue criterion introduced by Jiang and Sehitoglu [37] is used in the 2D analysis for cohesive elements, with the fatigue parameter (FP) defined as

$$FP = \langle \frac{\Delta\varepsilon}{2} \sigma_{max} \rangle + J\, \Delta\gamma\, \Delta\tau \tag{3-10}$$

where shear or normal stress and strain ranges ($\Delta\tau, \Delta\varepsilon, \Delta\gamma$) were calculated during one cycle. σ_{max} is the maximum normal stress in one cycle, and J is a material constant. The energy-based fatigue criterion (which is known as critical plane approach) searches for the plane which has the maximum FP, and considers that plane as the possible fatigue failure plane. Since it is assumed that grain boundaries are the place of crack initiation, FP is calculated at the grain boundaries (cohesive elements). In the 3D analysis, the fatigue parameter is modified to the following form

$$FP = \langle \frac{\Delta\varepsilon}{2} \sigma_{max} \rangle + J\, \Delta\gamma_{eq}\, \Delta\tau_{eq} \tag{3-11}$$

where, $\gamma_{eq} = \sqrt{\gamma_s^2 + \gamma_t^2}$ and $\tau_{eq} = \sqrt{\tau_s^2 + \tau_t^2}$ are absolute values of shear strain and shear stress at integration points, respectively. $\Delta\gamma_{eq}$, $\Delta\tau_{eq}$, and $\Delta\varepsilon$ were calculated at the end of each cycle as the difference between maximum and minimum of γ_{eq}, τ_{eq}, and ε, respectively, during one cycle. The relationship between fatigue life and fatigue parameter is described by

$$N_f = C\, (FP - FP_0)^{-m} \tag{3-12}$$

where, C, m, and FP_0 are material fatigue parameters, N_f is the total fatigue life, and fatigue will not initiate if FP is smaller than FP_0 [37]. These constants are obtained by fitting Equation (3-12) to the FP versus N_f curve on logarithmic scale. Fatigue damage is assumed to change linearly from 0 to 1, and fatigue life range is N_f; therefore, fatigue damage rate can be estimated as

$$\frac{dD_f}{dN} \sim \frac{\Delta D_f}{\Delta N} = \frac{1}{N_f} \tag{3-13}$$

From equations (3-12) and (3-13), the damage rate is related to the fatigue parameter by

$$\frac{dD_f}{dN} = \frac{(FP - FP_0)^m}{C} \tag{3-14}$$

where N is the number of loading cycles. Fatigue parameter is calculated at the end of each loading cycle, and the amount of fatigue damage can be found and updated based on the damage rate from Equation (3-14). In order to degrade the cohesive elements with cyclic loading, based on a similar method used in [125], the maximum traction (t^0) and fracture energy (G^C) of all normal and shear directions were updated at the end of each cycle by

$$t^0 = \left(1 - D_f\right)(t^0)_{initial} \tag{3-15}$$

$$G^c = \left(1 - D_f\right)(G^c)_{initial} \, . \tag{3-16}$$

A schematic of traction-separation law, and static and fatigue damage evolution is shown in Fig. 3-1. It is worth mentioning that traction-separation law is valid for either normal or shear tractions. For simulating a large number of cycles and reducing the computational time, an approach called "jump-in-cycles" is used. This approach eliminates the need for simulating every single cycle by extrapolating the results at the end of each block of cycles. Details of this approach are discussed in [156]. A schematic of the applied damage model considering the "jump-in-cycles" approach is depicted in Fig. 3-2, and fatigue damage constants used in this study are presented in Table 3-1.

Table 3-1. Fatigue damage model parameters.

Fatigue constants for 12% manganese rail steel from [37]			“Jump-in-cycles” constant [156]	
C	m	FP_0	J	ΔD_f
6000	2.0	1.0	0.3	0.1

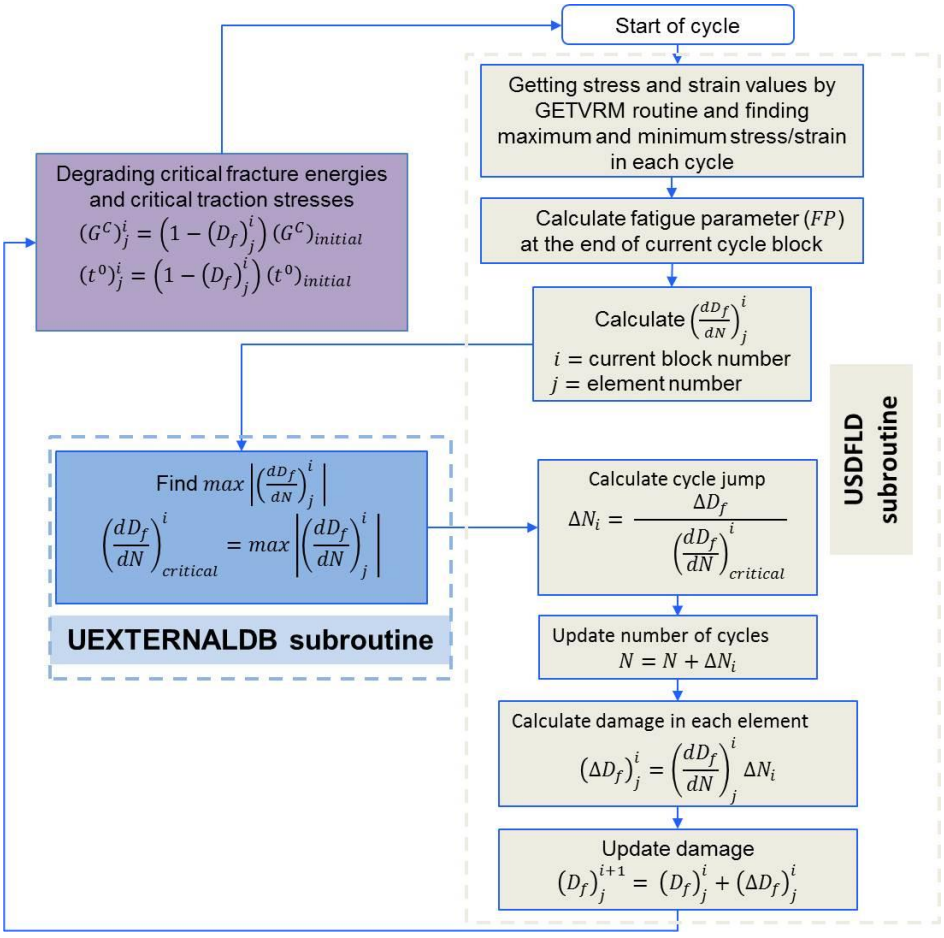

Fig. 3-2. “Jump-in-cycles” approach used to degrade cohesive elements strength and fracture energy in order to simulate fatigue damage in a high number of cycles. When damage in each element reaches one, that element gets removed from the simulation. The process continues until damage propagation becomes unstable.

3.3. **Finite element modeling**

3.3.1. 3D geometry

The contact between two rolling elements such as wheel and rail occurs in a small area, which is called contact patch. Contact stresses are very high in the contact patch, and large deformations take place in this area. It is valuable to study the contact patch by looking only at the microstructure of this region. To simulate a realistic representation of microstructure for studying RCF, the Voronoi tessellation algorithm is employed using open source software Neper [129]. This method helps to account for geometric randomness in microstructure, and the average grain size and deviation can be controlled by changing the density of seed points. The size of this granular microstructure cannot be large, because small meshes are required, and it is not computationally efficient to use granular microstructure in all regions of the model. Only the contact patch is modeled with a detailed microstructure, and the other parts are meshed with simple tetrahedral elements.

The granular microstructure, which is called representative volume element (RVE), is considered as the target region, and results will be extracted from this region (Fig. 3-3a). Each color in this figure represents a crystalline grain. The size of RVE is chosen to be large enough to consider the randomness of microstructure. Random orientation is assigned to each grain to have a more realistic microstructure. At the interface of grains, cohesive elements are applied to simulate crack initiation and propagation due to RCF (Fig. 3-3b). The grains are meshed with 4-node linear tetrahedral elements (C3D4 in Abaqus), and cohesive elements are meshed with COH3D6 elements. RVE contains 500 grains, and the average grain size is selected to be $50\ \mu m$, which is a reasonable grain size for manganese rail steels. Since the wheel-rail contact patch area consists of a large number of grains, it is not computationally possible to simulate all of the grains; therefore, the geometry is scaled to $1/10$ of actual rail contact patch size. In order to have continuity in the model, and simulate half-space around the contact patch, the RVE is placed inside a larger model. As shown in Fig. 3-3c, this geometry is considered large enough to eliminate the edge effects. The larger model is meshed with first-order tetrahedral elements (C3D4 in Abaqus), and its inner surfaces are tied with the RVE surfaces.

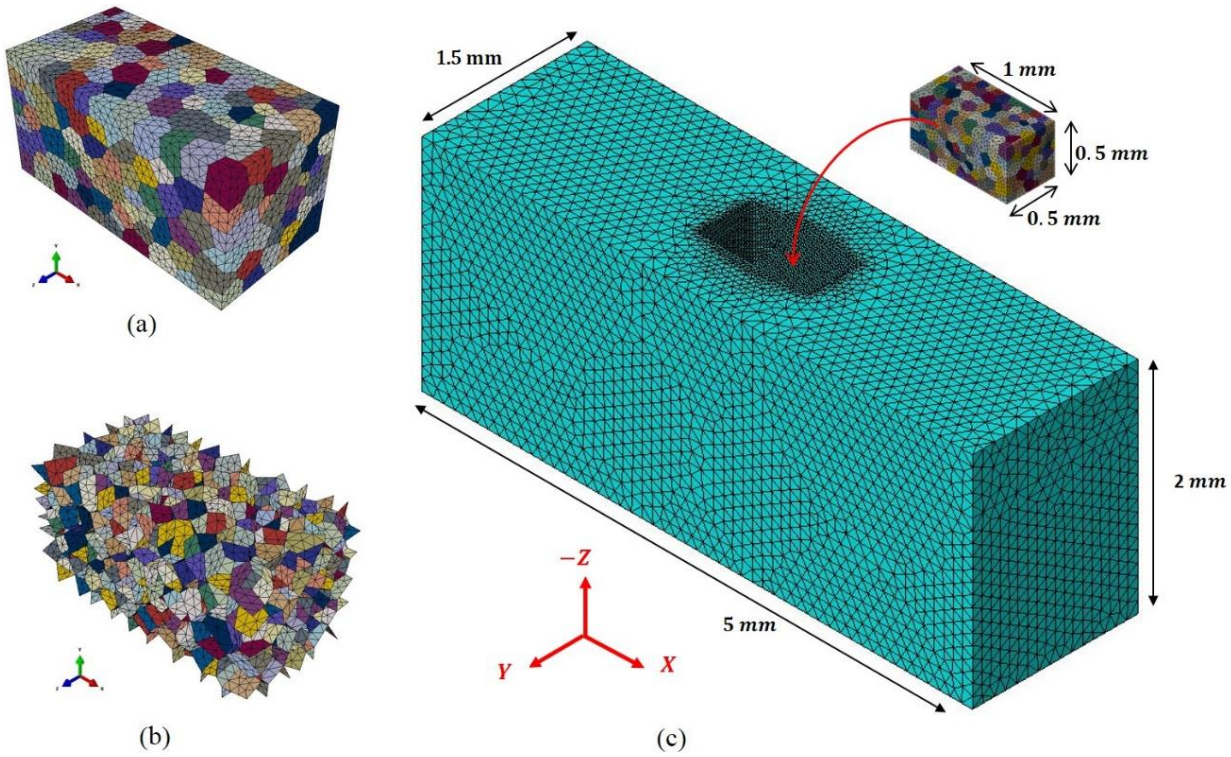

Fig. 3-3. (a) RVE with 500 grains (each color represents a grain), and (b) cohesive elements representing grain boundaries. (c) 3D geometry consists of two regions: RVE with small mesh sizes containing the cohesive elements at the grain interfaces, and a larger model containing the RVE

Elastic-plastic material properties calibrated with tension a test were used at the first stage for the large region; however, by switching to elastic properties, it did not affect RVE results. So, elastic properties were used for simplicity in the larger model. There are similar approaches that have used the Voronoi tessellation method to study RCF in bearings [15, 35, 128]. In these researches, periodic boundary conditions are applied in the Y direction (transverse); however, in the current study, periodic boundary conditions are not used. The reason is that although the grains can be modeled and meshed periodically in the Neper software, cohesive elements are not periodic, and this will cause non-periodic damage.

3.3.2. Loading distributions

In order to simulate wheel load on the rail, frictional rolling contact is defined by the superposition of 3D normal Hertzian load and tangential traction load on the surface of created geometry. The distributions of the mentioned loads are described in the following sections.

3.3.3. Hertzian normal load

Point contact Hertzian load distribution is used in the current study for simulation of the normal load. Different studies on wheel-rail interaction have measured the contact patch, and it is shown that the contact patch is almost elliptical. The Hertzian contact theory also leads to an elliptical contact patch and a semi-ellipsoid contact pressure distribution [157]

$$p(x,y) = p_{max}\sqrt{1-\left(\frac{(x-x_c)^2}{a^2}+\frac{(y-y_c)^2}{b^2}\right)} \tag{3-17}$$

where p_{max} is the Hertzian peak pressure, (x, y) is the load position, (x_c, y_c) is the position of the maximum load, a and b are the half-widths of contact patch in X (rolling direction) and Y (lateral direction), respectively. The schematic of the movement span in each block of cycle and Hertzian distribution of load are shown in Fig. 3-4. The method is implemented in Abaqus using the DLOAD subroutine.

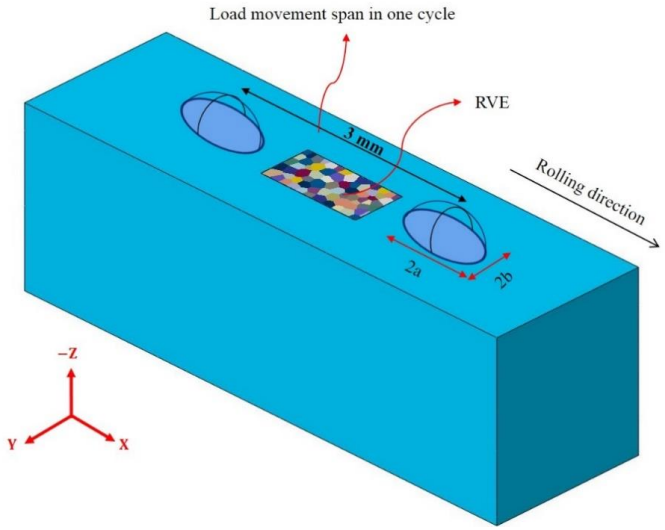

Fig. 3-4. Schematic of Hertzian load movement on the top surface of the model

3.3.4. Tangential traction loads

Tangential traction loads are present in rolling contact because of micro-slippage between contact surfaces. The ratio of tangential load (F_x) to normal load (F_z) is defined by

$$\mu_{tr} = \frac{F_x}{F_z} \tag{3-18}$$

where, μ_{tr} is known as the traction coefficient (or adhesion coefficient). The limiting value for μ_{tr} is friction coefficient μ. The ratio of μ_{tr} to μ is defined by

$$\zeta = \frac{\mu_{tr}}{\mu} \tag{3-19}$$

where ζ is called normalized traction or partial slip ratio. ζ is a variable between 0 and 1 that defines the amount of slip in partial slip region. When ζ is equal to zero, pure rolling contact (stick) condition exists, and for $0 < \zeta < 1$, the contact region is divided into a slip region and a stick region. When ζ is equal to one, full slip contact occurs, and traction force is approximately equal to the Coulomb friction force. A schematic of slip and stick regions in the contact patch is illustrated in Fig. 3-5a. Partial and full slip conditions happen in the wheel-rail contact patch because of the relative speed difference of wheel and rail known as creepage. For creepages between 0 and approximately 1-2% [158], partial slip condition is present, and for larger values full slip happens. Full slip can happen in higher creepages; however, we use normalized values of $\zeta = 0$ to 1 for zero slip to full slip ranges, and creepage percentage that full slip occurs does not affect our study. The relation between the normalized applied traction (ζ) and normalized slip length ($\frac{c}{a}$) is derived by Haines et al. [159] and illustrated in Fig. 3-5b.

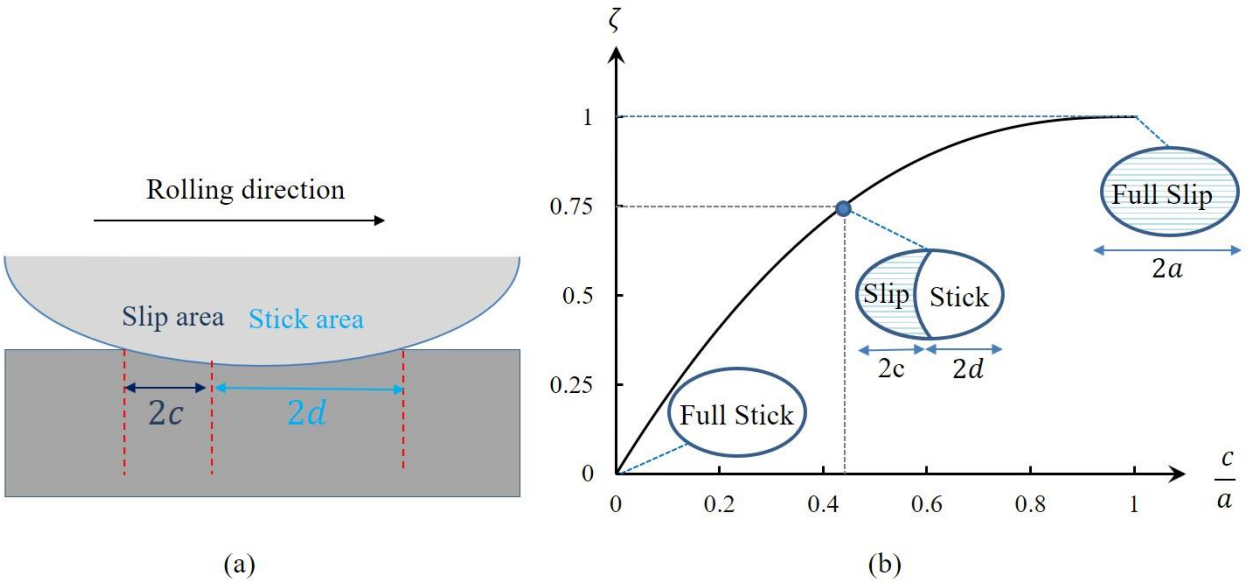

Fig. 3-5. (a) Schematic of slip and stick areas under partial slip condition. (b) The relation between the normalized traction ($\boldsymbol{\zeta}$) and normalized slip length

In full slip condition, tangential traction distribution (q) is proportional to the normal load distribution (p); however, in partial slip condition, this distribution depends on the slip and stick regions length (see Fig. 3-5 for definition of slip and stick length c and d). Haines et al. [159] presented the strip theory that illustrates the 3D shape of traction under partial slip condition. In this theory, the elliptical contact patch is divided into a series of strips parallel to the rolling direction (Fig. 3-6a). Each strip is studied with Carter's theory perpendicular to the contact surface as shown in Fig. 3-6b. The tangential traction $q(x)$ for each strip is defined as [160-162]

$$q(x) = q_1(x) + q_2(x) \tag{3-20}$$

where

$$q_1(x) = \mu p_{max} \sqrt{1 - \left(\frac{x}{a'}\right)^2} \tag{3-21}$$

$$q_2(x) = -\frac{c'}{a'}\mu p_{max}\sqrt{1-\left(\frac{x+d'}{c'}\right)^2} \tag{3-22}$$

The values of a', c' and d' are illustrated in Fig. 3-6a and Fig. 3-6b. The above formulations are implemented into our model using the UTRACLOAD subroutine. The resulting traction distribution for $\zeta = 0.25$ is illustrated in Fig. 3-6c. The tangential traction distribution for different ζ values are utilized to study the effect of partial slip on RCF, and different cases are studied.

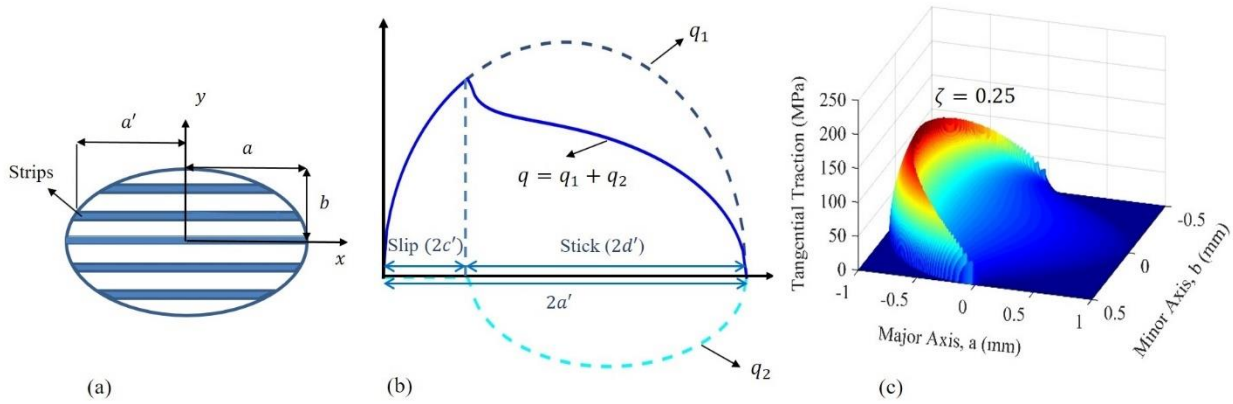

Fig. 3-6. (a) Schematic of the contact patch area and strips that are used by Haines et al. [159] to build the 3D distribution of partial traction loads. (b) Distribution of applied load perpendicular to each strip under partial slip condition. The final load distribution ($\boldsymbol{q}$) is a combination of slip ($\boldsymbol{q_1}$) and stick ($\boldsymbol{q_2}$) traction loads. (c) 3D tangential traction distribution for $\boldsymbol{\zeta = 0.25}$

3.4. Results and discussions

3.4.1. Determination of material properties

In order to find the proper material properties for constitutive models, the material models need to be calibrated with the experimental data. Macroscopic stress-strain data of manganese rail steel is obtained from [150]. For the calibration purpose, a cubic grain structure is created and meshed. The model contains 500 grains (shown in Fig. 3-7a) and cohesive elements are applied

between grains. The number of grains is adequate to simulate the behavior of polycrystalline material based on the previous research by Brommesson et al. [163]. The crystal plasticity material model is used for the grains, with the traction-separation law applied to cohesive elements. A random orientation is applied to each grain to have a more realistic simulation of polycrystalline material. It is not readily possible to determine which boundary condition is better for an RVE with strain localization and damage. Different boundary conditions like Neumann, Dirichlet or periodic boundary conditions are used in the literature and discussed in [164]. For simplicity, boundary conditions corresponding to uniaxial tension are utilized in this research, similar to boundary conditions in [163]. Displacement is controlled in loading direction by limiting left surface displacement and applying displacement to the right surface (other surfaces are traction free). The reaction forces and displacement in loading direction are extracted, and the average stress and strain of the whole model are obtained. Fig. 3-7b and Fig. 3-7c show the surface cracks and internal cracks due to the tensile loading of the generated RVE.

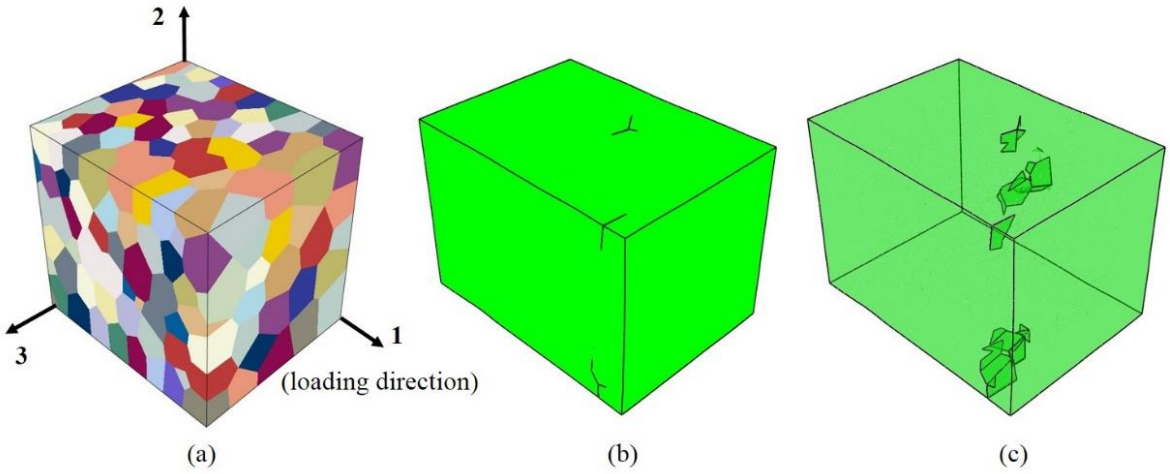

Fig. 3-7. (a) Cubic microstructure with 500 grains and cohesive boundaries at interfaces of grains. (b) Surface cracks and (c) internal cracks at interfaces of grains in the deformed geometry

In order to fit the stress-strain curve from simulation to the experimental data, a two-step calibration method is used in this research. The first step is to calibrate the crystal plasticity constitutive model parameters by assuming grain interfaces have perfect bonds. Anisotropic

elastic moduli were taken as $c_{11} = 174\ GPa$, $c_{12} = 85\ GPa$, and $c_{44} = 99\ GPa$ from a study on high manganese steels by Pierce et al. [165]. Although these elastic constants are for 25% manganese steel, they are used for 12% manganese steel in our study and in [166], and the results fit well with the elastic section of experiments. Plastic properties (h_0, τ_0, and τ_s) that affect plthe astic region of macroscopic stress-strain curve were calibrated by trial and error based on [167]. The initial hardening modulus, h_0, affects the initial slope of the plastic region, while τ_0 defines the yield stress and saturation stress, τ_s, determines the reference stress that large plastic flow initiates. Fig. 3-8a shows a few cases that were used to match the simulation results to the experimental result. The blue line is the best fit to the experimental macroscopic stress-strain curve of manganese rail steel before failure. The plastic constants for each case and the best match are presented in Table 3-2. By looking at similar researches for strain rate sensitivity values (n), Lindroos et al. [166] used $n = 10$ for Hadfield steel in nearly similar strain rate equation of crystal plasticity model. Furthermore, El Shawish et al. [168] used $n = 20$ to have negligible viscous behavior for Austenitic steel. Using larger values for the strain rate sensitivity ($n \to \infty$) results in rate independent behavior; however, some numerical problems would occur during the analysis. We have used $n = 10$ in this research, and other crystal plasticity parameters q and $\dot{\gamma}_0$ are assumed to be 1.0 and 0.001, respectively [155].

The second step is matching the fracture behavior of our simulation with the experiment. To this end, cohesive element parameters should be calibrated to simulate the fracture behavior. Due to a large number of parameters, and very limited data on cohesive behavior near the crack tip, it is hard to determine which method works best for representing the cohesive behavior. Tvergaard and Hutchinson [169] showed that the most important parameters are the fracture energy (G^c) and maximum traction stress (t^0). Based on researches by Simonovski and Cizelj [122, 170], shear stiffnesses, tractions, and fracture energies are related to their normal values by Equation (3-9) and change accordingly by changing E_n, t_n^0 and G_n^c. Also, they used Young's modulus as their cohesive stiffness. Similar assumptions are made in this research, and only maximum traction and fracture energy are changed by trial and error to fit the experimental fracture data. Cohesive element normal stiffness is chosen equal to the Young's modulus of material as $E_{nn} = 200\ GPa$. Original constitutive cohesive element thickness (T_0) needs to be small enough to not affect the overall stiffness of the model. $T_0 = 0.01\ mm$ was used in this study as the

cohesive element thickness. Initial critical normal traction (t_n^0) value was considered 500 MPa to be near the yield strength, and then it was increased to fit the experimental data. Furthermore, increasing fracture energy (G^c) shifts the failure toward larger strains. By considering all of these effects, different cases were examined to find the best fit to the experimental data. Fig. 3-8b shows trials to find the best fit, and the blue curve shows the best match for the elastic, plastic and fracture part of macroscopic stress-strain experimental data. Cohesive element parameters for each case and the best fit are presented in Table 3-2.

Table 3-2. Calibrated material constants for crystal plasticity model, and cohesive parameters

Plastic constants for crystal plasticity model				Cohesive parameters		
Case number	h_0 (MPa)	τ_s (MPa)	τ_0 (MPa)	Case number	t_n^0 (MPa	G_n^c (mJ/mm^2)
1	100	270	236	1	600	0.3
2	580	290	190	2	600	0.6
3	240	290	188	3	800	0.6
4	190	290	180	4	800	1.1
Best fit	190	290	188	5	800	0.9
				Best fit	800	0.75

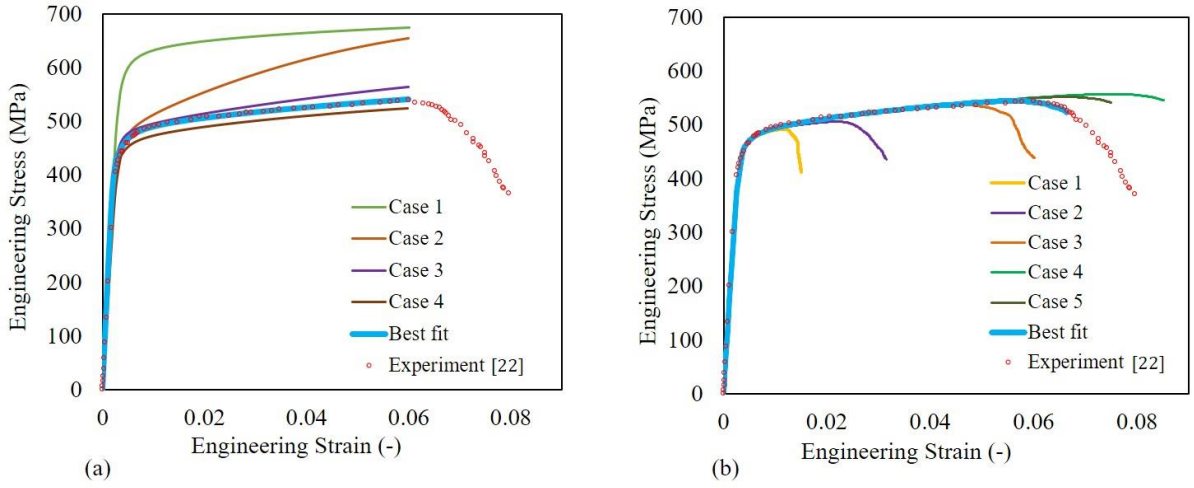

Fig. 3-8. (a) First step: calibration of crystal plasticity model with changing plastic properties ($\boldsymbol{h_0}$, $\boldsymbol{\tau_0}$, and $\boldsymbol{\tau_s}$). (b) Second step: calibration of cohesive model parameters.

3.4.2. Effect of grain shape and orientation randomness

In order to study the effect of grain shape and orientation randomness, five models with the same size and number of grains but the different initial distribution of seed points are created and meshed. Material properties presented in section 3.4.1 are used in these simulations. The stress-strain results are presented in Fig. 3-9a. Model 1 is the calibrated model described above. All models show similar behavior in elastic and plastic regions up to the softening initiation point. After this point a scatter in the fracture region is present, and fracture strain changes in different models. This scatter occurs because of different crack initiation and propagation behavior in different models. Fig. 3-9b illustrates formed cracks in different models in the uniaxial stress contour plot. By comparing Model 1 and Model 5, it is clear that there is a dominant crack in Model 5, while dispersed small cracks are present in Model 1. This causes more brittle behavior for Model 5, and fracture happens sooner compared to Model 1. The crack planes are also effective in fracture behavior. Cracks in Model 1 have a larger deviation from a straight crack plane compared with the main crack in Model 5. The results clearly show the effect of randomness in the shape and orientation of grains on fracture strain under tensile loading.

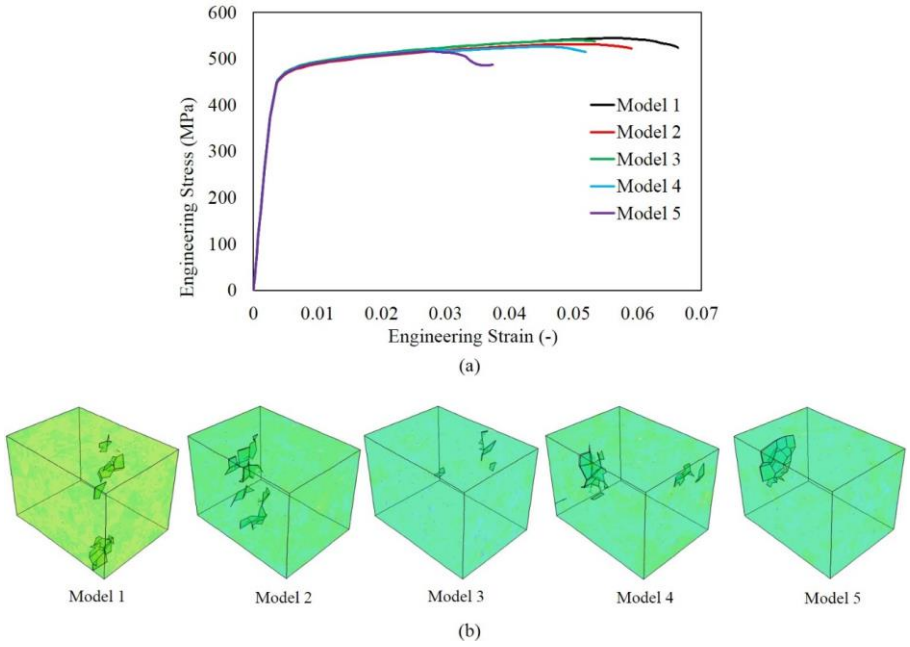

Fig. 3-9. Effect of microstructural randomness is demonstrated by (a) stress-strain response of five randomly distributed models with 500 grains, and (b) corresponding crack pattern in the uniaxial stress contour plot.

In order to find the effect of grain shape and orientation on RCF, five models with different RVEs were tested under the Hertzian normal cyclic load. The life of each model is reported in Table 3-3. These lives are obtained at the average damage of 0.004 in all cohesive elements for each model. The results indicate that the RCF lives lie within the 5% difference of the average life. Although these five models have considerable scatter in fracture strain under tensile loading, there is less variation in RCF life with Hertzian cyclic loading. Model 1 has nearly the same life as the averaged life; therefore, we have used Model 1 as our RVE in the RCF studies.

Table 3-3. RCF lives for models with different grain and orientation distribution

Model number	1	2	3	4	5	Average
Life (cycles)	228341	239687	223100	226511	223924	228711

3.4.3. Model Validation and static results

We have compared the results of crystal plasticity, and an equivalent isotropic model under the static condition with Hertzian loading distribution. Both isotropic and calibrated crystal plasticity models follow the stress-strain behavior of Manganese steel shown in Fig. 3-8. The goal is to find out how the crystal plasticity behaves compared to the isotropic model under Hertzian loading. The normalized stresses versus depth are illustrated in Fig. 3-10.

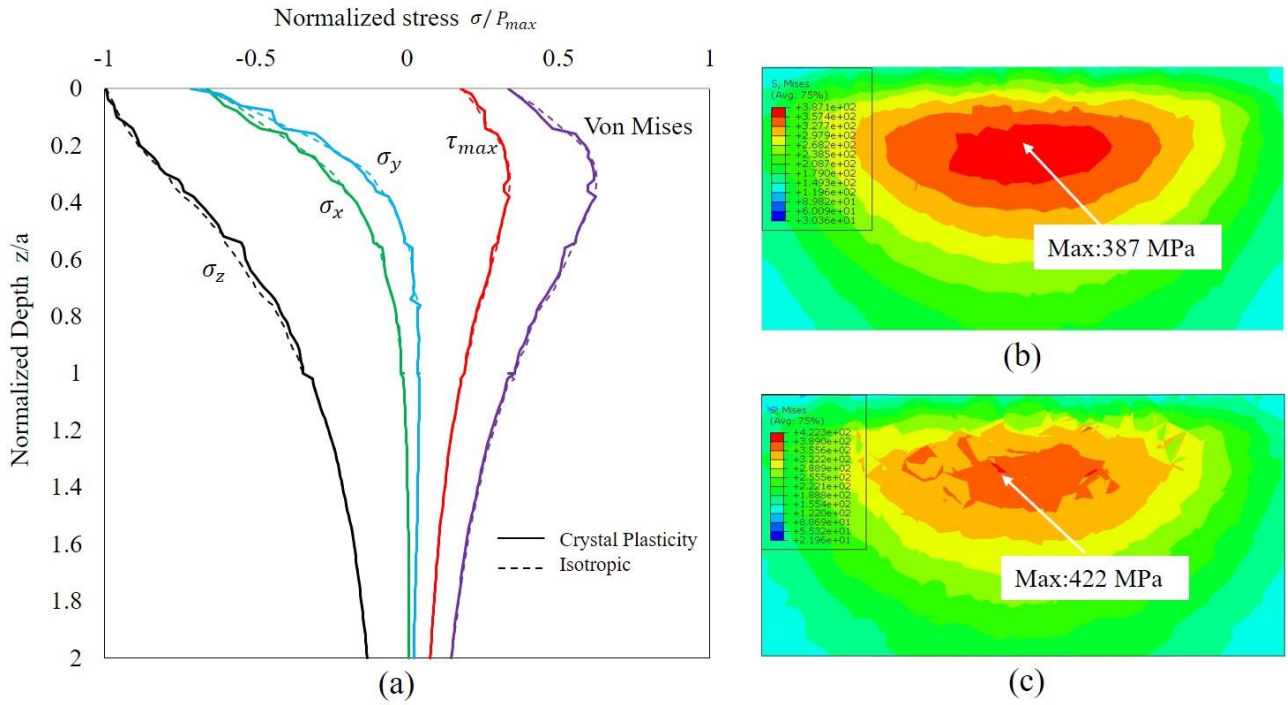

Fig. 3-10. (a) Centerline stresses for crystal plasticity and isotropic models under static Hertzian point load contact. Von Mises stress distribution for (b) isotropic and (c) crystal plasticity models

It is clear from Fig. 3-10a that the crystal plasticity model with anisotropic behavior follows the isotropic model. Stresses from the crystal plasticity model have some deviations from the isotropic model, which is due to the different orientations of grains. Stress variation in the subsurface follows the same trend as theoretical Hertzian centerline line contact distribution if we compare our results with results in [35]. The equations of Hertzian line contact and point contact are different. Therefore, in our point-contact analysis (shown in Fig. 3-10a), we observed similar σ_x and σ_y pattern with different values (because of the elliptical shape of contact patch); however, σ_x and σ_y have different patterns compared to each other in line contact analysis (because of half space assumption) [35]. Fig. 3-10b and Fig. 3-10c show Von Mises stress distribution in the isotropic model and crystal plasticity model, respectively. More deviation and a higher value for Von Mises stress are found in the crystal plasticity model compared to the isotropic model similar to the results observed in [36].

3.4.4. Effect of friction coefficient and partial slip on RCF

Upon calibrating the material models, the model is used to study the effect of loading conditions on RCF. The presented method has several attractive characteristics. The key advantage of this method is considering the effect of microstructural features like shape and orientation of grains in RCF studies. Another valuable feature of the model is considering fatigue at the grain interfaces. Although there are a few assumptions on the calibration of the grain interfaces and fatigue parameters, the performance of the model is promising, as will be elaborated on next. Due to the localization of stress and anisotropic definition of the model, mesh size can affect the results. The current mesh is selected to be very small; however, a model with finer mesh was created, and the results were compared with the current model results. No noticeable difference was observed between the results, so we used the current mesh in our studies. Different friction coefficients ($\mu = 0.0$, 0.15, 0.30 and 0.45), and normalized tractions ($\zeta = 0.05, 0.25, 0.50, 0.75$ and 1.0) are studied in this section. For each ζ, the corresponding normalized slip region size based on Fig. 3-5b is used in the model as presented in Table 3-4.

Table 3-4. Normalized traction (ζ), and corresponding normalized slip region size (c/a)

ζ	0.05	0.25	0.50	0.75	1.0
$\frac{c}{a}$	0.022	0.114	0.250	0.440	1.0

The term "damage" presented in the following results refers to the averaged damage in cohesive elements of the RVE, so it is clear that the value of damage will be small since many of cohesive elements do not experience much damage. The number of cycles, as well as damage, are calculated and stored in solution-dependent state variables (SDV) at each block of cycles during the simulation. The final life is determined when the damage evolution slope becomes large. This generally occurs when the numerical solution diverges because of the high number of damaged elements. The damage-life curve is plotted for different friction coefficients and normalized tractions in Fig. 3-11. This figure shows a clear trend in the effect of the friction coefficient. Models with higher friction coefficients, experience a shorter life at the same damage value. In order to compare the life values for each model, the damage value of 0.001 is selected (shown in Fig. 3-11). The life values for different friction coefficients and ζ values at selected damage are depicted in Fig. 3-12. The results indicate that changing friction coefficient significantly affects

the life of the model. For instance, the predicted life at $\zeta = 0.25$ for $\mu = 0.45$ is 6671 cycles, while at the same ζ, the life for $\mu = 0.15$ is 71592 cycles, amounting to one order of magnitude longer life. This example clearly shows the importance of friction management at the contact areas of rolling components.

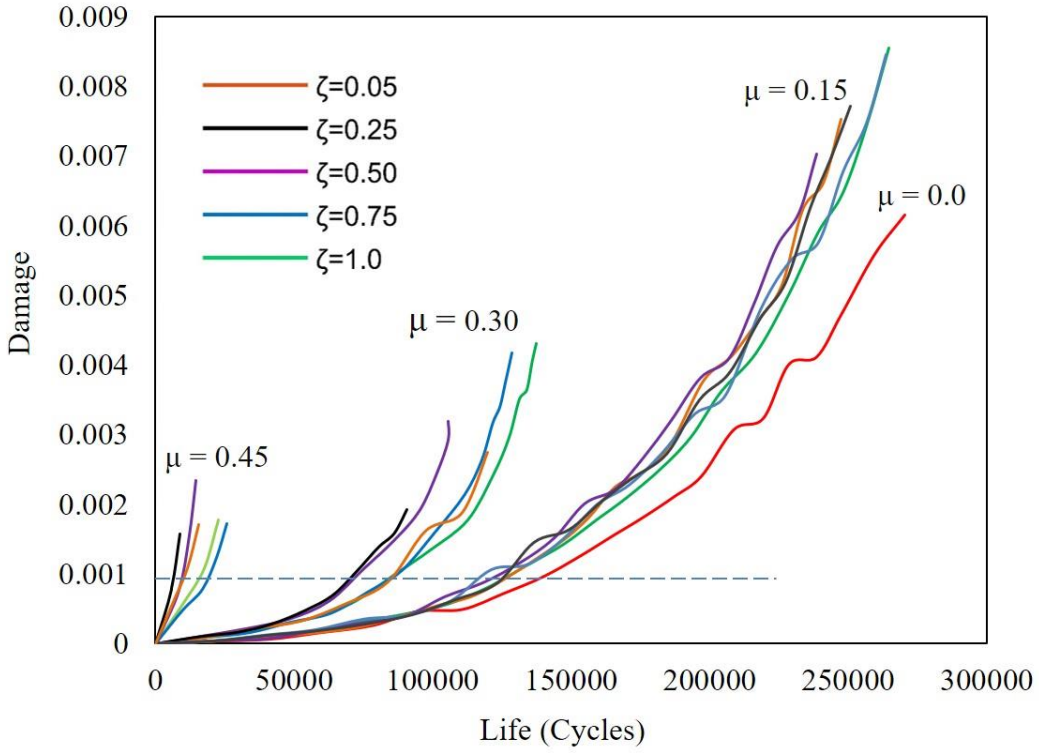

Fig. 3-11. Damage-life plots for different friction coefficients and normalized tractions. The friction coefficient has more effect on RCF life than changing partial slip conditions (changing $\boldsymbol{\zeta}$), and higher friction coefficient reduces the life significantly.

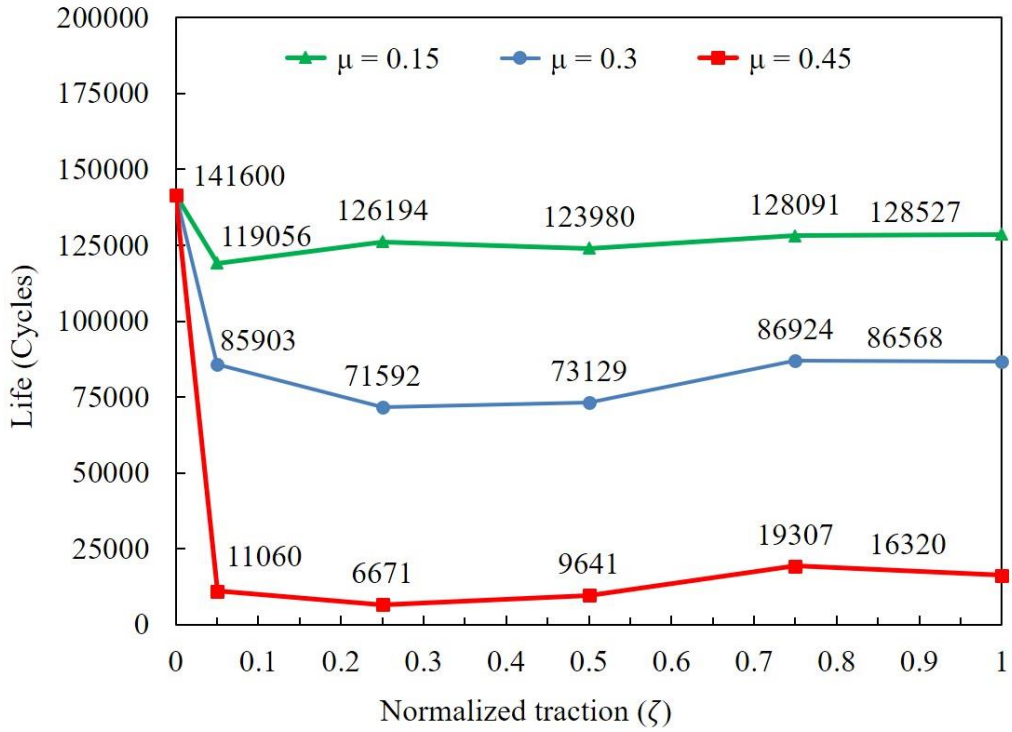

Fig. 3-12. Life versus normalized traction at the averaged damage of 0.001. Each number on the plots indicates the calculated life value at the specified condition. Lower friction coefficients exhibit a longer life.

Partial slip conditions (various ζ) have less effect on RCF life compared to friction coefficient; however, they are showing interesting results at a specific friction coefficient. By looking at Fig. 3-12, we were expecting a descending pattern in life because of increasing traction forces; however, a noticeable pattern in life was observed. When ζ changes from 0 to 1 in higher friction coefficients ($\mu = 0.30, 0.45$), predicted life has the lowest value in $\zeta = 0.25$ and then the life shows a slight upward trend. To ensure that this trend doesn't happen because of the grain shapes and orientation distribution of model, similar simulations were done on another model with different grain and orientation distribution, and the results are presented in Fig. 3-13a. As it is apparent from Fig. 3-13a, the same trend is present in both models, so we can conclude that this behavior does not happen because of grain shapes and orientations. In order to find out the possible explanation for this behavior, we looked at the research performed by Clayton et al. [171]. The research studied the fatigue behavior of pearlitic and bainitic rail steels under water-

lubricated conditions. In one of their experiments using a twin-disk rolling/sliding testing machine, they observed a similar pattern in four different pearlitic rail steel. Their experiments revealed that RCF life falls significantly with a small increase in slide to roll ratio (creepage) from 0 to 0.3%, but it increases with changing creepage from 0.3% to 1%. One of their results is presented in Fig. 3-13c. Since this pattern was not observed in the previous researches at that time, they were not able to find an explanation for this pattern. Another research confirming the same observation is performed by Wang et al. [172] on the effect of slip ratio on rolling contact fatigue in rail materials under wet conditions (shown in Fig. 3-13d). In this research, they noticed the same pattern as was seen by Clayton et al. They have discussed several possible descriptions for this pattern including the effect of the distribution of slip and stick areas in the contact zone on the hydraulic crack growth rate, and competitive relation between wear damage and RCF. They mentioned that this is a complicated pattern and can be result of combination of various parameters. Since our model does not consider the effect of hydraulic cracks and wear rate, we believe this pattern is related to distribution of loading in slip and stick areas. The load distributions for different ζ values are depicted in Fig. 3-13b. By looking at Fig. 3-13b, with assumption of Carter's theory on loading distribution in partial slip condition, we can see a sharp transition from stick to slip regions in smaller ζ values. This sharp transition in load distribution can increase the crack growth rate and inducing more damage. Clearly, there may be other reasonable explanations for this behavior, and it needs more simulations and experiments until it becomes clear.

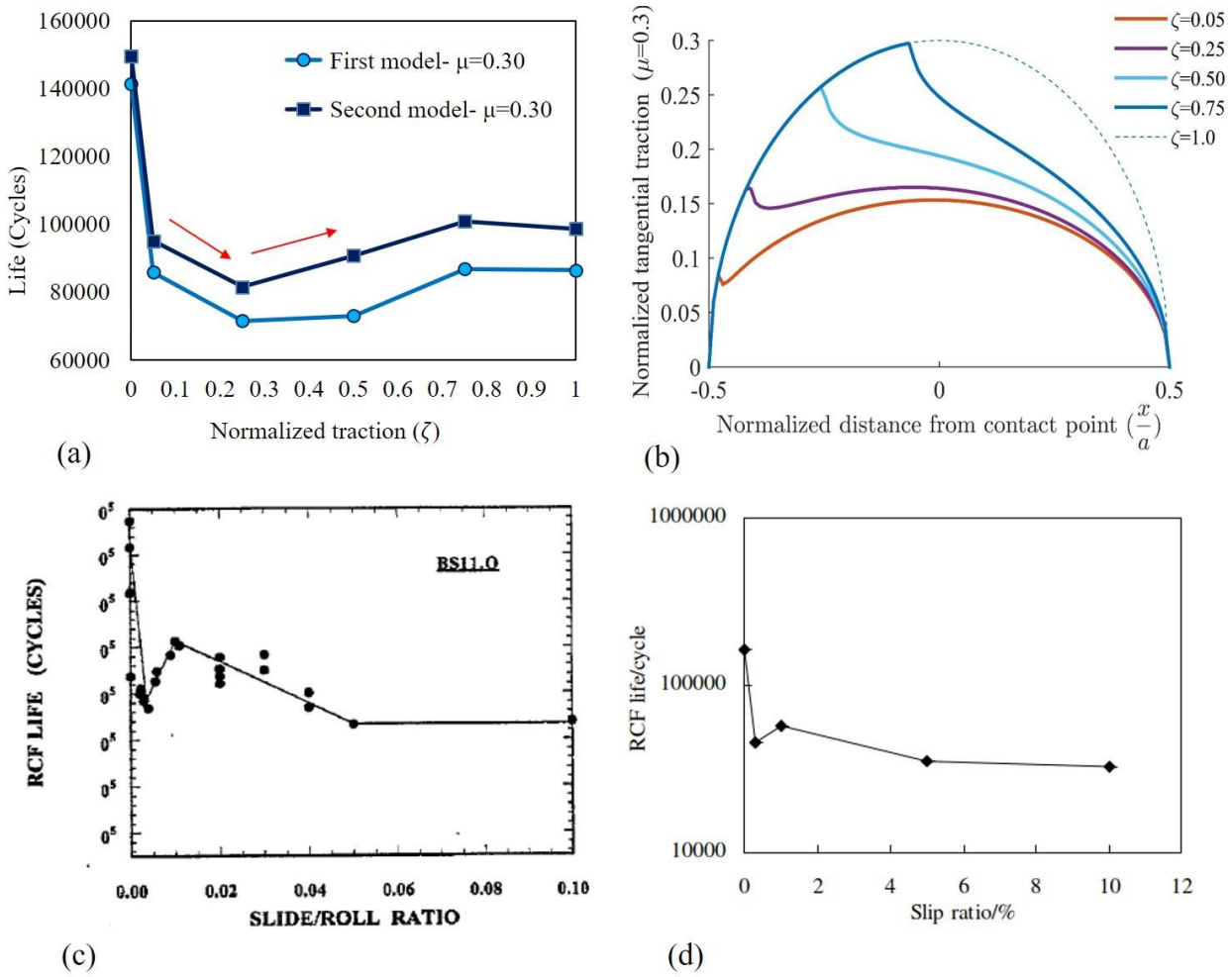

Fig. 3-13. (a) Life versus normalized traction of two different models shows a similar pattern for life drop at $\boldsymbol{\zeta = 0.25}$, and following slight rise in life. (b) Normalized tangential traction distributions for different values of $\boldsymbol{\zeta}$ show sharp transition from slip to stick regions in lower $\boldsymbol{\zeta}$ values. (c) and (d) are RCF life versus slip ratio experimental data obtained from researches by Clayton et al. [171] and Wang et al. [172], respectively. Both results show a decrease in RCF life by changing the slip ratio from 0 to 0.3%, and a slight increase in life by changing the slip ratio from 0.3% to 1%.

Considering the stress-strain behavior of rolling contact with different friction coefficients yields valuable results. Fig. 3-14 shows different contour plots in the RVE at the end of the simulation for different friction coefficients. The plots are taken from the middle section of RVE ($Y = 0$) and show the results in XZ plane. The first plot illustrates the accumulated plastic strain for the RVE, which is the total cumulative shear strain γ on all FCC slips. For $\mu = 0$, all of the plastic

deformations occur underneath the surface. By increasing μ to 0.30, and then to 0.45, plastic deformations tend to move toward the surface. The same pattern exists for the shear stress plot. Since RCF is known as a shear-dominated phenomenon, the location of maximum shear stress is important for studying RCF. In the last plot, failed cohesive elements due to RCF are shown. The depth of these failed elements is the same as the depth of maximum plastic strain and shear stress. Magel [24] stated that for low friction conditions, cracks form at the subsurface in the place of maximum shear stresses, which confirms current model observations. For lower friction coefficients, cracks from beneath the surface, while for higher friction coefficients the cracks form, mostly, on the surface. Ma et al. [140] observed several spalling and surface cracks for high friction coefficients which validate the current results.

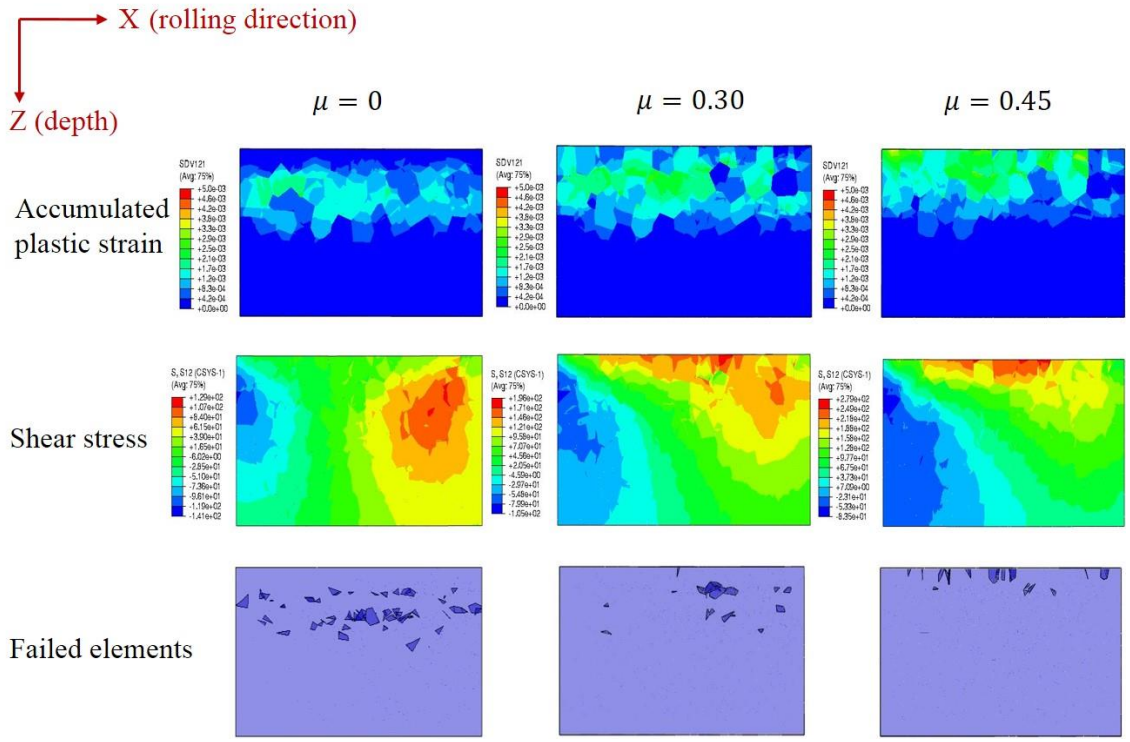

Fig. 3-14. Contour plots of accumulated plastic strain, shear stress and failed cohesive elements in the RVE for different friction coefficients. The plots show that increasing the friction coefficient will move plastic strain and shear stress toward the surface of the sample. The RCF cracks occur at shallower depths with a rise in friction coefficient since RCF mostly occurs at maximum shear stress.

Fig. 3-15 shows the accumulated plastic strain versus depth for $\mu = 0.30$ with different normalized tractions (ζ). The results are taken at the center of RVE for various depths ($X = Y = 0$, and variable Z), when the maximum load passes this point (middle of first cycle). For the "no friction" case, the plastic strain on the surface (depth=0.0) is zero, and maximum plastic strain occurs at higher depths. Adding a small value of tangential traction (i.e. $\zeta = 0.05$) causes plastic strain on the surface. $\zeta = 0.05$ and 1.0 have the smallest plastic strain on the surface, while in the range between 0.05 and 1.0 plastic strain is higher at surface. The maximum plastic strain for cases with traction occurs nearer the surface compared with the case with no friction. It is worth mentioning that $\zeta = 1.0$ case (i.e., full slip condition) does not have maximum plastic strain at either of surface and subsurface compared with other ζ values, despite higher traction forces. This can be attributed to the distribution of traction forces at the stick and slip areas for different ζ values, deliberated previously in Fig. 3-13.

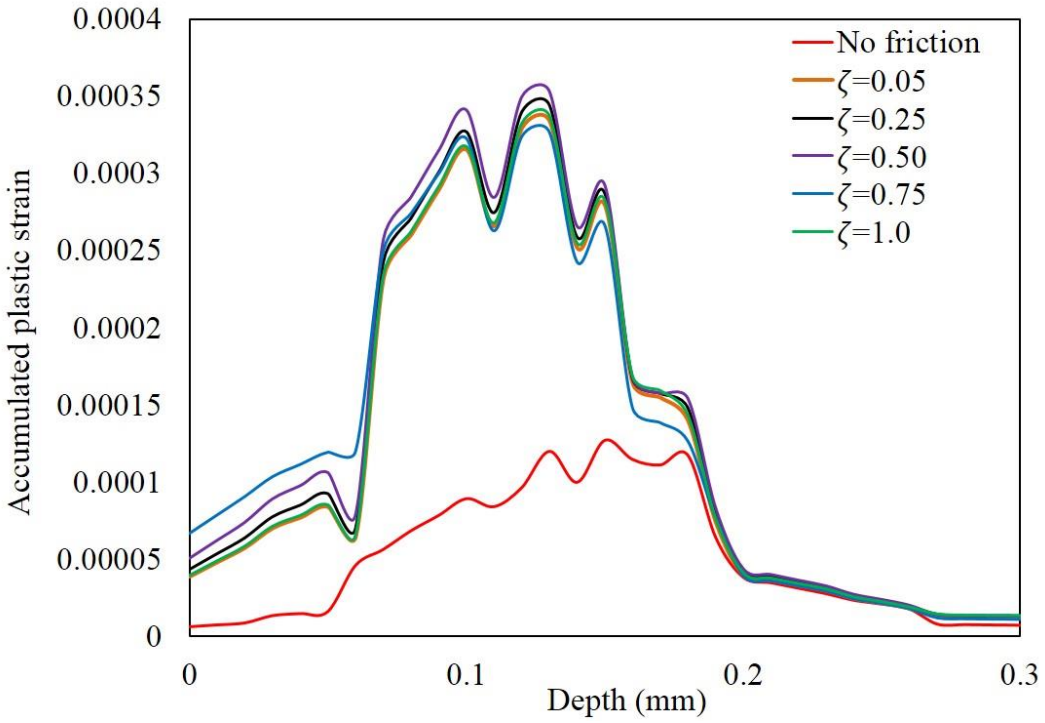

Fig. 3-15. Accumulated plastic strain versus depth for different normalized traction ratios ($\boldsymbol{\mu = 0.30}$). In case of "no friction", no plastic strain is present on the surface (depth=0.0). The maximum strain occurs in the subsurface. Adding a slight traction force ($\boldsymbol{\zeta = 0.05}$) causes plastic strain on the surface. The depth of maximum plastic strain also shifts toward the surface by adding tangential traction. $\boldsymbol{\zeta = 1.0}$ reveals that this case is not the critical case at either surface or subsurface despite higher traction forces.

Our main purpose in this study was finding the relative trend in RCF life considering microstructure and comparing the results for different conditions. Finding the exact life needs more detailed data, due to the large number of parameters that can affect RCF. Considering RCF experiments in the literature, no clear data is reported for many parameters such as residual stress, bending stresses, and surface conditions. Also, the current model is not intended to be an all-inclusive model in terms of the RCF parameters such as the interaction of RCF with wear or a detailed microstructure. Extensive testing is needed to measure the effect of all of the parameters on RCF; which, of course, then the results can be used for model calibration purposes. Furthermore, a significant amount of additional work is needed to include effects such as more detailed loading, exact contact patch configuration, and more realistic microstructure

3.5. **Conclusions**

A finite element model considering crystal plasticity, cohesive zone approach, and the microstructure of the material is developed to study the RCF. Voronoi tessellation algorithm is employed to create the microstructure of grains. Cohesive elements are applied at the interfaces to simulate the grain boundaries. Crystal plasticity is used to provide a precise stress-strain behavior within the grains, while the Jiang-Sehitoglu fatigue damage evolution law is used for representing the degradation of grain boundaries with increasing the number of loading cycles. The "Jump-in-cycles" approach is also used for simulating the high number of cycles and improving computational efficiency. A two-step calibration method is employed to find the proper material properties. Upon successfully calibrating the material models to experimental data, the effect of friction coefficient and partial slip within the contact area on RCF is studied. It is found that increasing friction coefficient moves the accumulated plastic strain and maximum shear stress. It is further shown that the initiation of cracks moves from slightly beneath the surface toward the surface, by increasing the friction coefficient. For partial slip, we obtained comprehensive results showing that there is a significant decrease in fatigue life by adding a small amount of tangential traction, although life increases by further adding traction forces until full slip condition is reached. In addition to revealing novel deformation mechanisms, the results validate similar experimental findings in the literature, in the sense that there is a satisfactory agreement between the predicted results and experiments. Future work should concentrate on a

more detailed microstructure model including elongated grains near the surface and developed texture at the surface and subsurface.

Chapter 4

4. Fracture and fatigue analysis of 3D printed metallic alloys at the microstructural level

Selective laser melting (SLM) as a part of metal additive manufacturing (AM) technologies, is altering the manufacturing processes very fast, and fundamental research in this area is vital at this stage of development. In this work, we have analyzed fracture and fatigue behavior of 3D printed samples developed by the SLM method at the microstructural level. The first part of this chapter is focused on the fracture study of melt pools and melt pool boundaries. In the second part of this chapter, we have studied fatigue in the cellular microstructure that is created during the 3D printing process of metallic alloys by the SLM method. We have developed a model for fatigue damage modeling and examined the effect of geometric parameters on the fatigue life of cellular microstructures. It needs to be mentioned that discussions in this chapter apply only to the microstructures developed in 3D printing of metals by the SLM method.

4.1. Fracture modeling of metallic alloys made by SLM additive manufacturing method

4.1.1. Overview

To study the fracture behavior in the 3D printed metallic alloys developed by the SLM method, a computational framework is developed in collaborative work with the University of Michigan [173]. Based on the actual microstructure (Fig. 4-1a), a realistic geometry is created [173], which consists of melt pools joined together by cohesive surfaces (shown in Fig. 4-1b). Each melt pool consists of several grains as shown in Fig. 4-1b (grains are not visible in Fig. 4-1a).

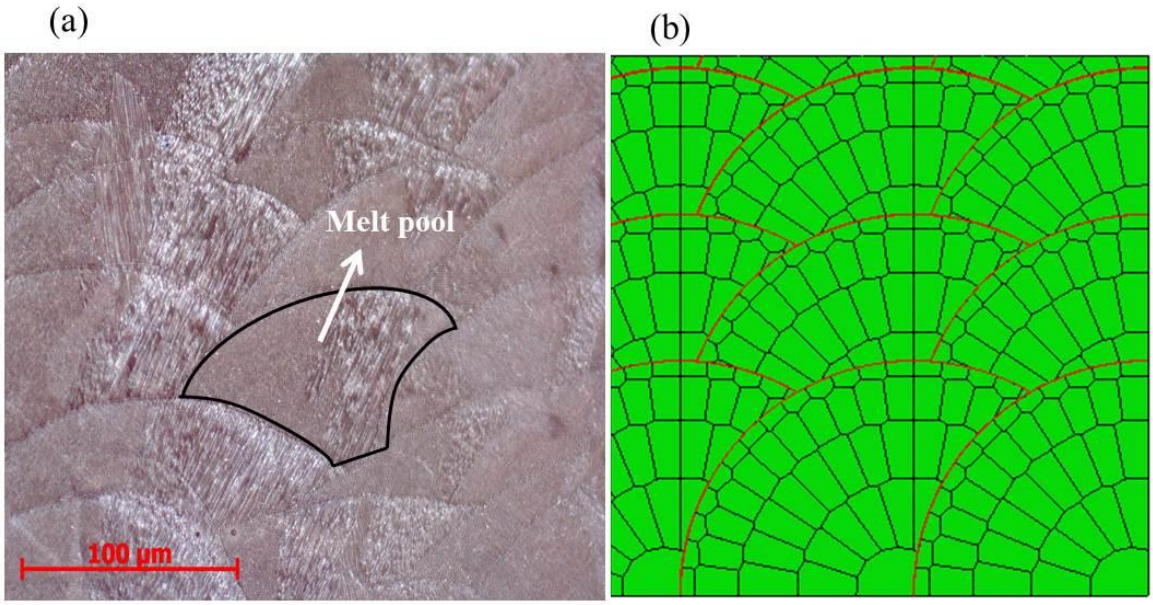

Fig. 4-1. (a) Optical microscope image of the SLM part shows melt pools in the microstructure. (b) A realistic geometry of melt pools is created [173], and cohesive surfaces are used as melt pool boundaries (highlighted with red color). Each melt pool consists of several grains, and these grains are considered in the model.

The following sections discuss our contribution to this research, which includes the calibration, methodology development and numerical analysis of fracture in the generated microstructure. Although works in the current study focus on selective laser melting technique, the findings are expected to extend to other AM powder-based processes that have similar mechanisms, such as direct metal deposition.

4.1.2. Material and methods

3D printed 316L stainless steel is used in this study. The most noticeable feature of SLM 316 stainless steel compared to the materials produced by conventional manufacturing techniques is its high yield strength. The possible reason behind this observation is the presence of a larger amount of grain boundaries in microstructures of SLM 316L stainless steel which would block the dislocation movements [173].

Cohesive surfaces are defined between the neighboring melt pools, in order to simulate the process of crack initiation and crack propagation in the melt pool boundaries. This approach,

which is known as cohesive zone modeling (CZM), is similar to using cohesive elements, and traction-separation law is applicable to the cohesive surfaces. Similar traction-separation law to what was discussed in section 2.2.2 is utilized here. However, in this approach, there is no real element between the melt pools, and cohesive interactions are applied as contact properties. For modeling material behavior of melt pools, crystal plasticity model is employed in this framework. The crystal plasticity model was discussed previously in section 3.2.1.

4.1.3. Calibration of materials models with experiments

Crystal plasticity parameters and cohesive zone modeling constants are calibrated by simultaneously fitting the stress-strain data derived from tensile tests. As a general guideline on the initial estimations, the model parameters calculated for 316L stainless steel in other studies are used [30]. A good agreement between the simulation and experimental results can be observed in Fig. 4-2. The calibrated crystal plasticity constants are reported in Table 4-1. Moreover, the cohesive zone method (CZM) constants are derived to be $t_n^0 = t_s^0 = t_t^t = 700\,MPa$ for damage initiation tractions and $G_n = 13.9\,mJ/mm^2$ for total fracture energy. A small value of damage stabilization (0.001) is used to increase the convergence of the problem near the softening region.

Table 4-1. The calibrated elastic and plastic material constants used to define the properties of grain structures

Constants	C_{11} (GPa)	C_{12} (GPa)	C_{44} (GPa)	h_0 (MPa)	τ_s (MPa)	τ_0 (MPa)	q
Value	107.10	46.80	70.10	100	270	96	1.0

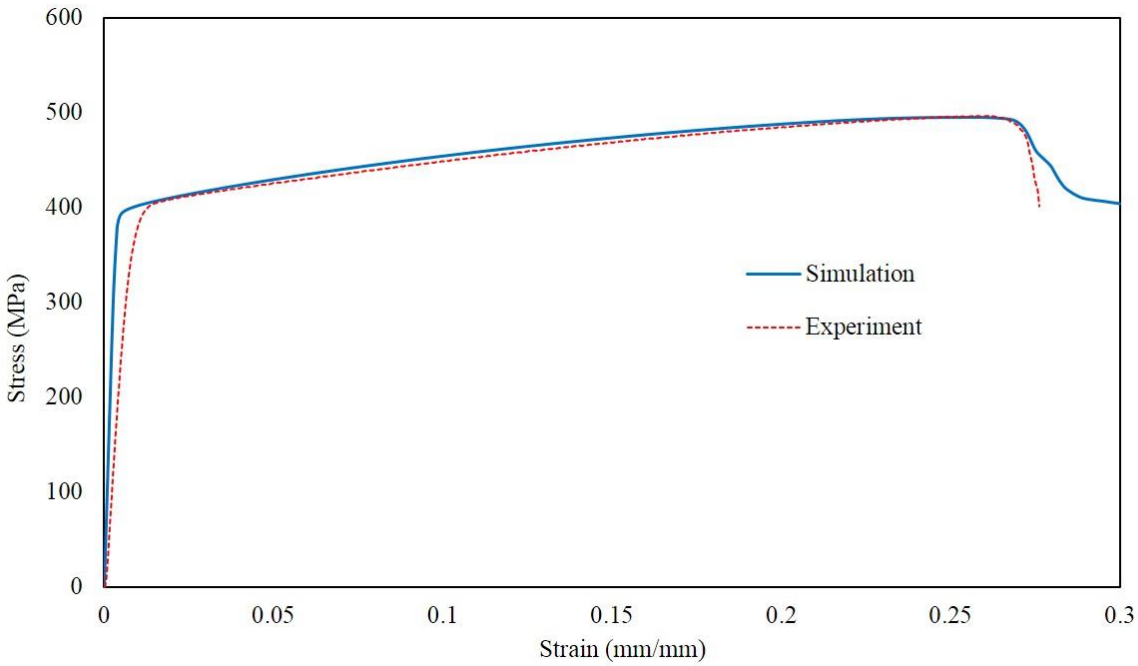

Fig. 4-2. The comparison of experimental data and simulation results using the calibrated crystal plasticity and cohesive zone constants. A good agreement can be observed.

4.1.4. Numerical study of effective parameters on damage properties of SLM products: static analysis

Several case studies are considered in this section to help further understand the capability of the developed model in studying some of the important phenomena in the damage properties of metals made by SLM. In section 4.1.4.1 the role of pre-existing cracks in melt pools, 4.1.4.2 the role of texture, and 4.1.4.3 the melt pools size on mechanical response and fracture behavior of polycrystalline 316L stainless steel made by SLM are investigated.

4.1.4.1. Effect of pre-cracks in melt pools

The AM of metallic alloys consists of complicated physics, such as materials evaporation [48], solidification of material, absorption and transmission of laser energy [174], and microstructure evolution [175]. The process is consequently affected by these factors to induce defects of cracks, unmelted regions induced by spatter particle, porosities, and impurities, etc. [71, 176]. These defects are detrimental to the mechanical and physical behavior of final parts, which limit the application of metals produced by AM. Cracks as one of the most commonly observed

defects during the AM process are induced by rapid melting and rapid solidification under a high energy input. It has been shown that the cooling rate of the molten pool reaches 10^8 K/s [177], which results in a great temperature gradient and therefore a large residual thermal stress in the final AM part. The high-temperature gradient along with the great residual stress creates cracks in the fabricated parts especially in the weak regions such as the melt pool boundary as shown in Fig. 4-3. To understand the effect of these pre-existing cracks on the fracture responses of SLM parts, randomly cracks are created in the RVE as shown in Fig. 4-4(a) and Fig. 4-4(b). Fig. 4-4(a) and Fig. 4-4(b) are the schematic representation of the RVEs with 3.5% and 7% of defects on the melt pool boundaries, respectively. The level of defects is determined by the volumetric ratio of the MPBs with cracks to the total MPBs. The stress-strain responses for the models with two levels of defects induced by cracks are given in Fig. 4-4(c). The obtained results are compared with the model without any cracks. As shown in Fig. 4-4(c), cracks in melt pool boundaries of SLM parts, cause a significant loss in ductility and the level of fracture stress. The ductility and the level of fracture stress for the RVE with 7% cracks on MPBs, RVE with 3.5% cracks on MPBs, and the RVE without any cracks are 7% and 422 MPa, 22% and 474 MPa, and 27% and 494 MPa, respectively. The observed significant difference in failure responses of dense and the RVEs with defects highlights the detrimental effects of cracks on the mechanical response of SLM parts.

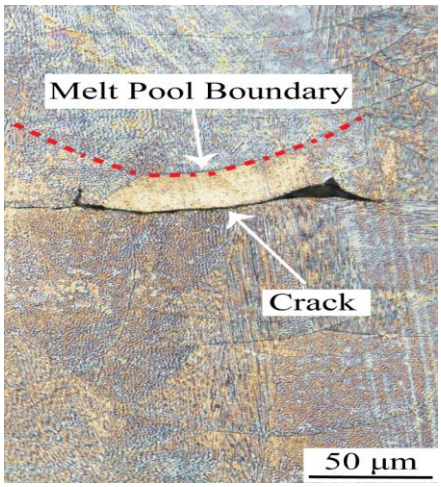

Fig. 4-3. Optical microscopy images of 316L stainless steel made by SLM which showing the presence of cracks on melt pool boundaries (adapted from our recent submitted work [173]).

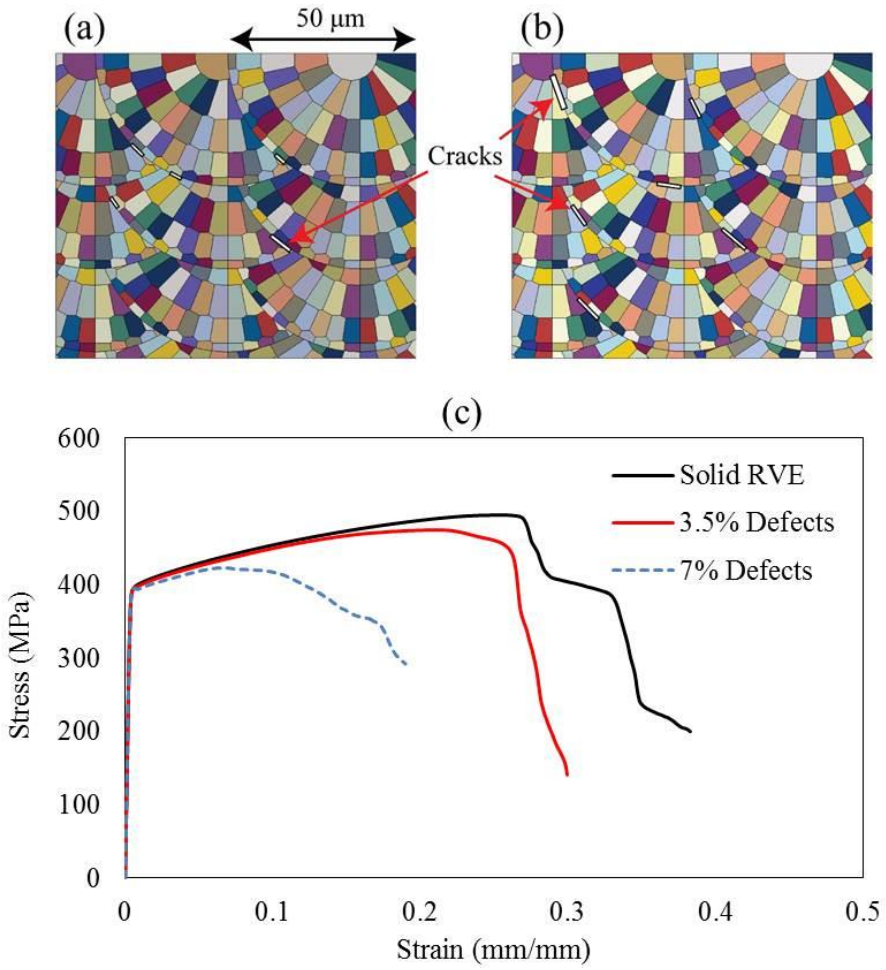

Fig. 4-4. Schematic representation of the RVE models including (a) 3.5%, (b) 7% defects from pre-existing cracks in the melt pool boundaries. (c) Stress (along y-axis) - strain (along x-axis) responses of the solid RVE and RVEs with 3.5% and 7% defects. The results show the significant role of pre-existing cracks in the fracture behavior of SLM products.

Fig. 4-5 presents the stress contour of the model with 7% defects for two stages of crack initiation and crack propagation. Fig. 4-5a shows the model at 7% strain, and first cracks (cohesive surface debonding) initiate at the melt pool boundaries, where the pre-existing cracks were present. After 21% of strain (as shown in Fig. 4-5b), the initial cracks that are perpendicular to the loading direction become the main cracks. These cracks propagate toward the edges and become large and unstable.

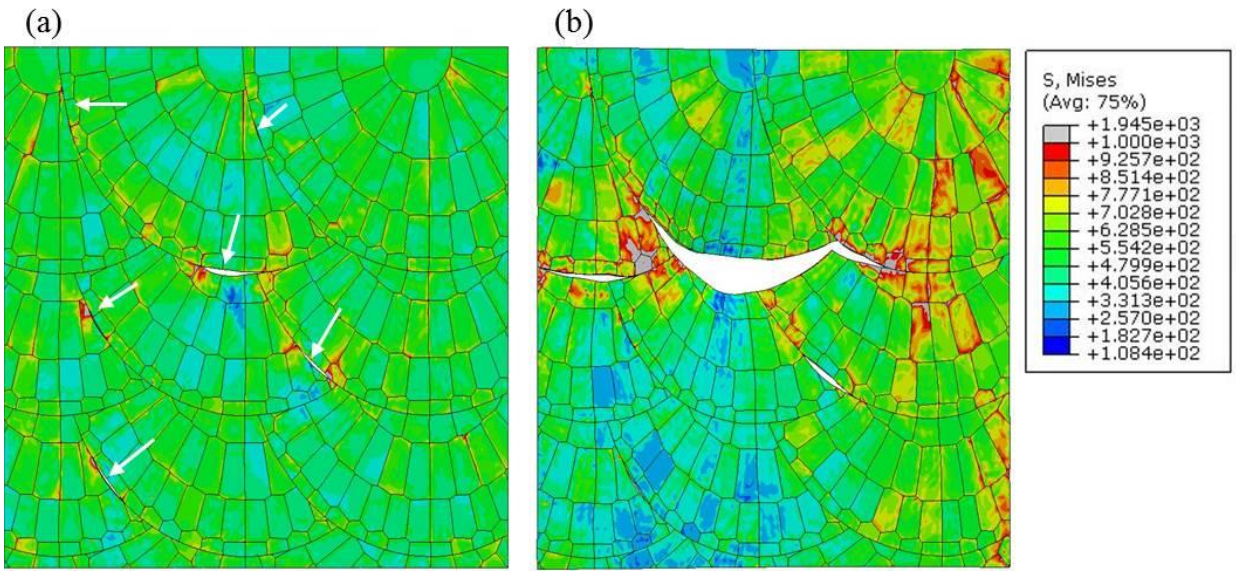

Fig. 4-5. Stress contour plot after (a) 7% strain and (b) 21% strain for the model with 7% pre-existing cracks. (a) Initial cracks start growing from pre-existing cracks are shown in (a), and cracks perpendicular to the loading become main cracks and propagate to final failure.

4.1.4.2. The Role of Crystal Orientation

The texture of metals made by AM techniques is highly dependent on processing parameters [57]. Dinda et al. found the high energy density of the laser during 3D printing of an Al-Si alloy, results in directional heat transfer and therefore a directional solidification [178]. The directional solidification is causing both morphological texture and crystallographic texture along $< 100 >$. In another study, Thijs et al. [48] show the length of scan vectors and laser scan strategy are effective on the crystal orientations of fabricated material. Long laser scan vectors would result in a strong $< 100 >$ texture along the laser scanning direction and a weaker $< 110 >$ texture along the building direction of the part. Moreover, the bidirectional scanning strategy in which the scanning direction is rotated by 90° every layer causes the overall crystallographic texture to be significantly reduced. In order to understand the effect of crystallographic texture on the failure response of polycrystalline SLM 316L stainless, two different distributions of crystal orientations in the grains are considered. A random orientation is assigned to each grain for modeling the untextured material and texture orientation is applied to each grain, in a way that $< 111 >$ orientations of the lattice structure are distributed aligned along the x-direction and $< 001 >$ directions are randomly distributed, to simulate the textured materials [179]. Fig. 4-6

shows the mechanical responses of both cases. The ductility of textured materials (~37%) and the level of fracture stress (~508 MPa) are superior to the ductility (~27%) and fracture stress (~494 MPa) of the untextured materials. Comparing these simulation results with the reported experimental findings, it is clear that the present model is predicting the effect of the crystallographic texture of AM materials on the fracture properties of the materials accurately [48].

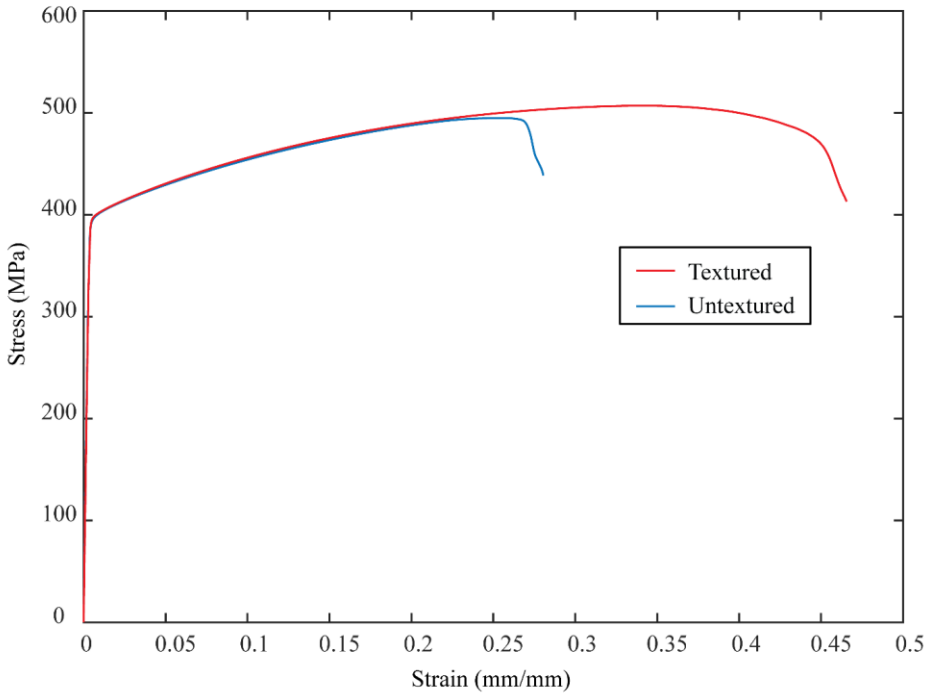

Fig. 4-6. The stress (along y-axis)-strain (along x-axis) response of textured and untextured RVE models. The results show the textured model has higher ductility and fracture strength compare to the untextured RVE model.

4.1.4.3. The melt pool size effect

In this section, the effect of size (or the number) of melt pools on the failure response of polycrystalline 316L stainless steel made by SLM is studied. A controllable melt pool size can be achieved by changing the hatch space (the distance between consecutive parallel laser beam tracks). Previous works showed the melt pool size and morphology directly impact the microstructure and mechanical properties of the final part [180]. To investigate this effect using the developed model, the stress-strain response of an RVE with 20 melt pools (Fig. 4-7(a)) is

compared with an RVE with 12 melt pools (Fig. 4-7(b)). The stress-strain curves for the uniaxial loading of both cases are shown in Fig. 4-7(c). It is observed the fracture in the RVE with the smaller melt pool sizes occurs faster than the one with larger melt pools. The ductility and the level of fracture stress of the RVE presented in Fig. 4-7(a) are ~16% and ~5401 MPa, respectively. However, the RVE illustrated in Fig. 4-7(b) shows a stronger response with the ductility of ~27% and the fracture stress of ~494 MPa. This difference in the fracture responses is related to the fraction of melt pool boundaries, which are considered as the weak regions in the SLM materials as described in section 4.1.2, in each RVE. The RVE with 20 melt pools has a greater fraction of melt pool boundaries compare to the model with 12 melt pools and therefore exhibits a weaker response to the fracture.

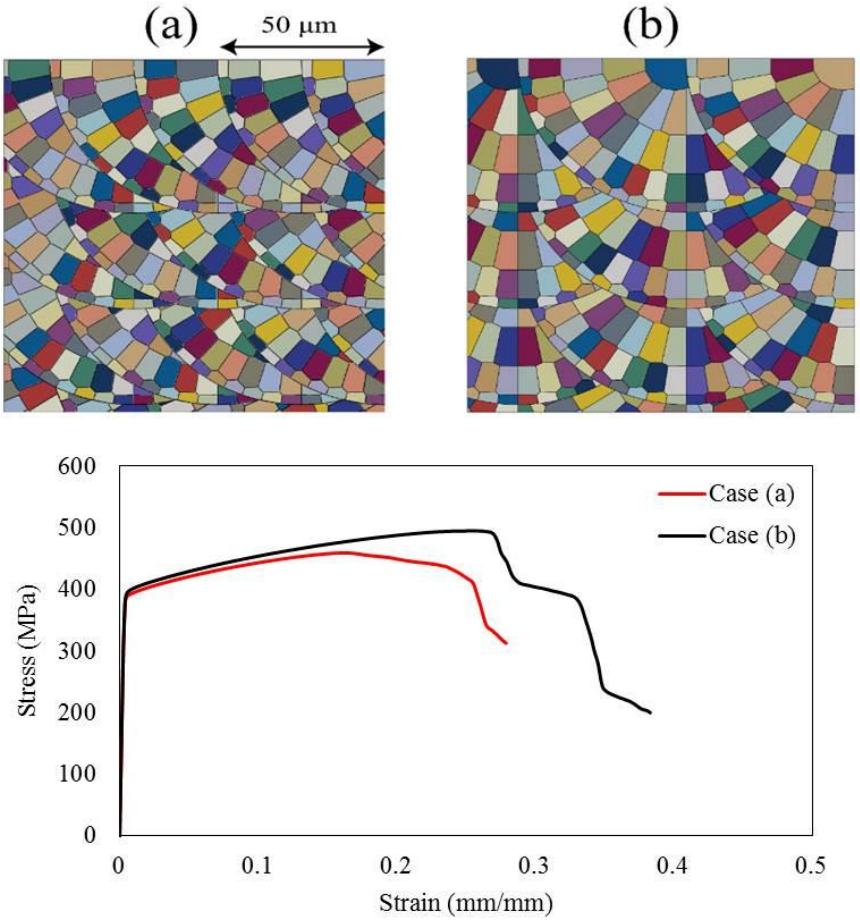

Fig. 4-7. (a) The RVE size with 20 melt pools, (b) The RVE size with 12 melt pools, (c) the stress (along y-axis)-strain (along y-axis) responses of (a) and (b) show increasing the number of melt pools (decreasing the hatch space) results in decreasing the fracture strength and the ductility of SLM products.

4.2. Computational Study of Fatigue in Sub-grain Microstructure of 3D Printed Alloys Developed by Selective Laser Melting Method

4.2.1. Overview

Additively manufactured materials exhibit shorter low and high cyclic fatigue lives compared to their wrought form. Shorter fatigue life can be related to different effects like defects, residual stresses, surface finish, geometry, size, layer orientation, and heat treatment. One of the main contributors to the shorter fatigue life of additively manufactured alloys is their unique and complex microstructure. In this research, we study this challenge from an unexplored perspective in which the interaction between the microstructure and fatigue life is explored. Among different microstructural features in the 3D printed alloys, here we focus on the cells which form inside the grains during fabrication. While this microstructural feature is not always the prominent site for the fatigue initiation, it always has a significant role in the fatigue failure, particularly in high cycle fatigue because it occupies a high percentage of the volume in the material. A phenomenological-based fatigue damage model is developed and verified to predict the life of cellular microstructures present in the 3D printed metal microstructure. It is shown that the life of a cellular microstructure, which is composed of an arrangement of cells and cell boundaries is lower than a single-phase material without such an arrangement. We investigate how the arrangement if cells can govern the fatigue life, and analyze different cellular geometries to find the best performing cellular microstructure. By changing the geometrical parameters, the considerable variation in life can be as high as 95% in some strain amplitudes. Since the microstructure of cells in 3D printed alloys can be tailored by changing the processing parameters, our results can be used as a guide to 3D print alloys with improved fatigue-resistance.

4.2.2. Cellular microstructure

In this research, we consider the Selective Laser Melting (SLM) 3D printing method and focus our studies on 316L stainless steel as a representative model alloy system to understand the basic principles of fatigue mechanisms. However, the findings are mostly comprehensive and can be extended to other fabrication methods or other alloy systems.

In the SLM method, due to very high cooling rates (105-107 K/s), "cells" (also known as sub-grains) with a systematic arrangement of squares, pentagons, or hexagons are formed. The formation mechanism of these intra-granular cells at different fabrication conditions is still an open question. However, studying the formation of cells is beyond the scope of this research, and we will particularly focus on investigating the fatigue behavior in an arrangement of cells, as shown in Fig. 4-8. A microstructural image of 3D printed 316L stainless steel taken with a Scanning Electron Microscope (SEM) is shown in Fig. 4-8a. The close-up view of this cellular microstructure (shown in Fig. 4-8b) reveals the connection of cells (black regions) and cell boundaries (white regions). The cellular microstructure (shown in Fig. 4-8c) is modeled and meshed by finite element software for the fatigue analysis. As shown, cells in the 316L microstructure have the average diameters in the range of 200 nm to 1 μm.

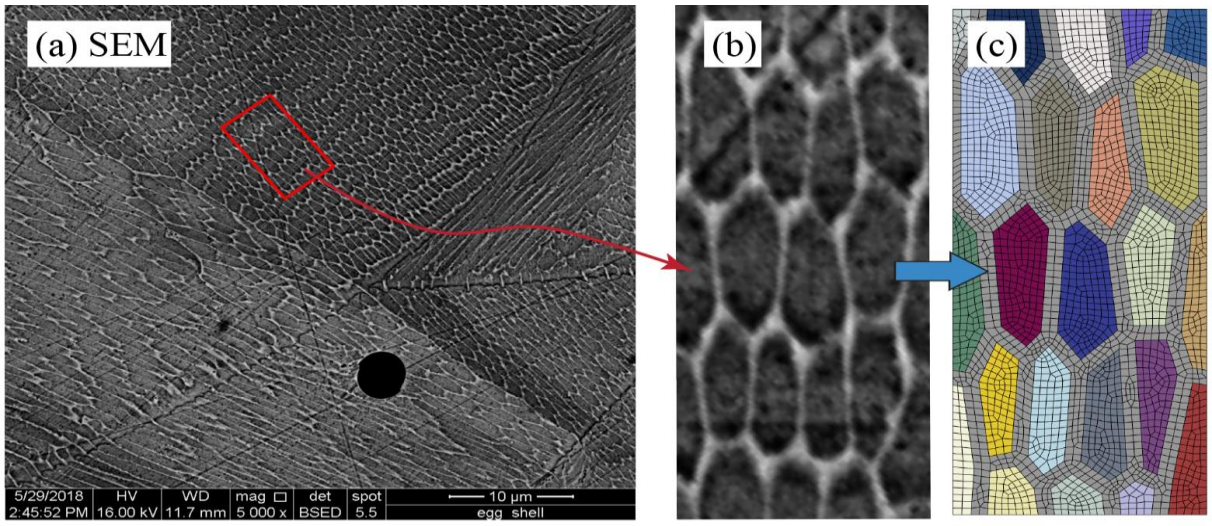

Fig. 4-8. (a) SEM image of the microstructure of 3D printed 316L stainless steel and (b) close up view of cellular microstructure. (c) Finite element meshed model of cellular microstructure

Further investigation of cells and cell boundaries reveals their properties are distinctly different from the grains and grain boundaries. Cell boundaries have a relatively large thickness, in the range of 10-50 nm. The alloy composition might differ inside the cell, and on the cell boundary. Based on the previously reported works [181-185], in 316L stainless steel Mo, Si and Cr have a slightly higher concentration at the cell boundaries compared to these in the cell interiors, which has a more concentration of Ni. The higher concentration of mentioned elements at cell boundaries makes them stronger than the material inside the cell. Therefore, we have utilized

fatigue properties of 316L stainless steel for the cell material and relatively stronger material properties for the cell boundaries which will be discussed more in section 4.2.4.2.

4.2.3. Material models

In order to study fatigue behavior and model the plastic deformation in cyclic loading correctly, using the appropriate material model is essential. In this research, a continuum-based material model is used to simulate the behavior of cells and cell boundaries at the microstructure of 3D printed alloys. In addition to modeling cyclic behavior, a fatigue damage approach with the jump-in-cycles method is also employed to degrade the material due to cyclic loading and predict fatigue initiation life. These models are described in the following sections.

4.2.3.1. J_2 continuum cyclic plasticity

The von Mises yield criterion (J_2 plasticity) combined with nonlinear isotropic and kinematic hardening is employed to specify the elastic-plastic deformation of materials under cyclic loading. Based on J_2 theory, strain tensor can be written as the sum of elastic and plastic strains as

$$\varepsilon_{ij} = \varepsilon_{ij}^{E} + \varepsilon_{ij}^{P} \tag{4-1}$$

The relationship between stress tensor and elastic strain is presented by

$$\sigma_{ij} = C_{ijkl}^{E}\, \varepsilon_{ij}^{E} = C_{ijkl}^{E}\, (\varepsilon_{ij} - \varepsilon_{ij}^{P}) \tag{4-2}$$

where C_{ijkl}^{E} is the elastic tensor. The plastic strain rate is defined by

$$\dot{\varepsilon}_{ij}^{P} = \dot{\lambda} \frac{\partial f}{\partial \sigma_{ij}} \tag{4-3}$$

where $\dot{\lambda}$ is the plastic multiplier and f is the von Mises yield criterion. $\dot{\lambda}$ can be demonstrated as

$$\dot{\lambda} = \dot{p} = \sqrt{\frac{2}{3}\,\dot{\varepsilon}_{ij}^{P}\,\dot{\varepsilon}_{ij}^{P}} \tag{4-4}$$

where $\dot{p}$ is the time derivative of accumulated plastic strain.

Hardening of materials can be represented by a combination of isotropic and kinematic hardening. Isotropic hardening defines the expansion/contraction of yield surface while kinematic hardening represents the translation of yield surface. Isotropic hardening function (r) is defined as

$$\dot{r} = b(Q - r)\dot{p} \tag{4-5}$$

where b and Q are material constants. Consideration of kinematic hardening is necessary for an accurate representation of cyclic loading due to the Bauschinger effect. Armstrong-Fredrick nonlinear kinematic hardening model which is the most common evolution law for describing kinematic hardening is defined as

$$\dot{x} = \frac{2}{3}\,c\,\dot{\varepsilon}^{p} - \gamma\,x\,\dot{p} \tag{4-6}$$

where x is the back stress, and c and γ are kinematic hardening material constants. The yield surface is defined by:

$$f = \left(\frac{3}{2}\,(\sigma' - x'){:}\,(\sigma' - x')\right)^{\frac{1}{2}} - r - \sigma_y \tag{4-7}$$

where σ' and σ_y are deviatoric stress and initial yield stress, respectively.

4.2.3.2. Fatigue damage model

To predict fatigue life for a multi-material sample, the fatigue damage approach with the jump-in-cycles method is employed. The fatigue damage parameter (D) can vary from the undamaged state ($D = 0$) to a fully damaged state ($D = 1$) in each element. The jump-in-cycles method extrapolates current damage results to predict the next damaged state. This method eliminates the

need for simulating every single cycle and significantly reduces computational costs. A control function is considered in the algorithm to automatically find the cycle jump (ΔN) based on the element with critical damage value. At the end of each cycle block, damage in all elements is calculated, and stress state and damage will be updated based on the new damage value. This algorithm is developed by using USDFLD and UEXTERNALDB Fortran subroutines linked with Abaqus. More details about this approach are presented in [156, 186]. The damage rate in all elements should be calculated and feed into the jump-in-cycles approach. Therefore, the following method is used for calculating the damage rate in each block of cycles.

Damage rate in each block of cycles is assumed to be constant (Miner's rule) as

$$\frac{dD}{dN} = \frac{\Delta D}{\Delta N} = \frac{1}{N_f} \tag{4-8}$$

where N_f is the fatigue life of the material. The strain-life method is widely used as an experimental method to find the fatigue behavior of a material. We have used the strain-life experiments of 316L stainless steel in our modeling approach. The relationship between fatigue life and elastic strain range in the strain-life approach is defined by Basquin's equation as

$$\frac{\Delta \varepsilon_e}{2} = \varepsilon_e^a = \frac{\sigma_f'}{E} \left(2\, N_f\right)^b \tag{4-9}$$

where ε_e^a, σ_f' and b are elastic strain amplitude, fatigue strength coefficient, and fatigue strength exponent, respectively. The relation between plastic strain and life is defined by Manson-Coffin as

$$\frac{\Delta \varepsilon_p}{2} = \varepsilon_p^a = \varepsilon_f' \left(2\, N_f\right)^c \tag{4-10}$$

where ε_p^a, ε_f' and c are plastic strain amplitude, fatigue ductility coefficient, and fatigue ductility exponent, respectively. Total strain can be written as a summation of elastic and plastic strain ranges as

$$\varepsilon_a = \frac{\Delta\varepsilon_e}{2} + \frac{\Delta\varepsilon_p}{2} = \frac{\sigma_f'}{E}\left(2\,N_f\right)^b + \varepsilon_f'\left(2\,N_f\right)^c \tag{4-11}$$

Using equations 4-8 to 4-10, elastic and plastic damage rates can be determined as

$$\left(\frac{\Delta D}{\Delta N}\right)_{elastic} = 2\left(\frac{\sigma_f'}{E\ \varepsilon_e^a}\right)^{\frac{1}{b}} \tag{4-12}$$

$$\left(\frac{\Delta D}{\Delta N}\right)_{plastic} = 2\left(\frac{\varepsilon_f'}{\varepsilon_p^a}\right)^{\frac{1}{c}} \tag{4-13}$$

Fatigue damage evolution for a pure elastic condition is only dependent on the state of stress. However, if material yields, the damage will be dependent on the plastic strain. Both elastic and plastic damage rates are considered in this research to accurately simulate the total damage evolution rate. By inspiration from [187], a weight function is added to the damage rate equation. In this case, the plastic damage rate would be dominant in low cycle fatigue where there is more plastic strain in the material, and elastic damage rate would be prevailing in high cycle fatigue. Total damage rate can be written as a combination of elastic and plastic damage rate by

$$\left(\frac{\Delta D}{\Delta N}\right)_{total} = \omega\left(\frac{\Delta D}{\Delta N}\right)_{elastic} + (1-\omega)\left(\frac{\Delta D}{\Delta N}\right)_{plastic} \tag{4-14}$$

where ω is a weight function defined as

$$\omega = \frac{\Delta\varepsilon_{elastic}}{\Delta\varepsilon_{elastic} + \Delta\varepsilon_{plastic}} \tag{4-15}$$

By adding the weight function to the total damage rate equation, the plastic damage rate would be dominant in low cycle fatigue where there is more plastic strain in the material. Elastic damage rate would be dominant in high cycle fatigue where major strain is the elastic strain. This method helps to predict the damage in both low cycle and high cycle fatigue conditions. By knowing total damage rate and cycle jump, the new value of damage will be calculated, and

material properties will be updated at the end of each cycle block to reflect the material degradation as [188]

$$E^{i+1} = E^{i}\,(1 - D) \tag{4-16}$$

$$c^{i+1} = c^{i}\,(1 - D) \tag{4-17}$$

$$\gamma^{i+1} = \gamma^{i}\,(1 - D) \tag{4-18}$$

$${\sigma_y}^{i+1} = {\sigma_y}^{i}\,(1 - D) \tag{4-19}$$

The fatigue initiation life is calculated when a few elements become fully damaged resulting in unstable solutions. This method works better for low cycle fatigue since the total life is almost equal to the fatigue initiation life, while for the high cycle fatigue condition a considerable amount of life is spent at the macro crack propagation stage.

4.2.4. Finite element model

4.2.4.1. Geometry

Fig. 4-8b shows a small section of cellular microstructure that contains several cells. A similar microstructure is initially generated and employed in Abaqus for fatigue studies. However, in order to make the geometry generation process automatic and study various microstructures, a simpler hexagonal model with different parameters is considered as shown in Fig. 4-9. The structure is planar and a small thickness through the inward direction makes it a three-dimensional geometry. Each cell in the microstructure has four geometrical properties *t*, *H*, *w*, and *l*. A simplified finite element representation of a finite volume of such a system is created, and material properties are assigned to the material in each of the cells and cell boundaries. Using an initial sensitivity analysis we observed that the cell thickness in this special case is the least sensitive parameter, and can be eliminated from the list of parameters. By considering three values for each of the remaining parameters (*H*, *w*, and *l*) a total of 27 geometries has been generated. Simple boundary conditions are used as shown in Fig. 4-9 and cyclic displacement ($R = -1$) is applied to the top surface.

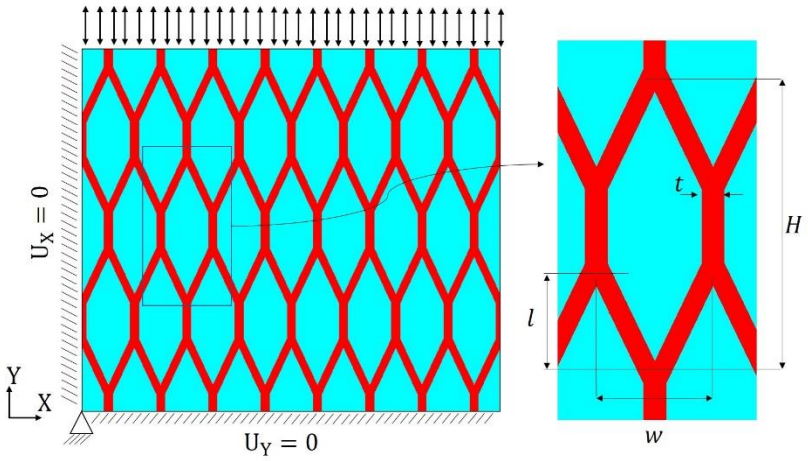

Fig. 4-9. Cellular microstructure boundary conditions and geometric parameters

4.2.4.2. Material properties

Material properties for cells are obtained from a study on fatigue behavior of 316L stainless steel [189]. The fact that cell boundaries have stronger yield strength and fatigue properties is attributed to more strengthening elements like nickel, chromium, and molybdenum located at the cell boundaries. 317L stainless steel which has a similar element composition to 316L stainless steel has higher strength and fatigue properties compared to 316L since it has slightly more strengthening elements. Therefore, we have assumed higher yield strength and fatigue strength for cell boundaries in this study. Isotropic hardening behavior is neglected, but kinematic hardening behavior is considered in this study. Cell and cell boundary material properties are presented in Table 4-2.

Table 4-2. Fatigue damage model parameters.

Material	J_2 continuum cyclic plasticity constants			Fatigue damage model constants				"Jump-in-cycles" constant
	σ_{0_y} (GPa)	C (GPa)	γ (-)	σ_f' (GPA)	b (-)	ε_f' (-)	c (-)	ΔD_f (-)
Cell	211	57805	619	1444	-0.159	0.294	-0.494	0.025
Cell boundary	250	57805	619	2438	-0.159	0.386	-0.494	

4.2.4.3. Verification of model

With the intention of verifying that the model predicts the correct fatigue lives, the model is tested separately for both cell and cell boundary materials. The geometry shown in Fig. 4-9 is used for this verification. The geometry doesn't affect the results much since only one material is used in each simulation and the stress-strain distribution is homogenous in all elements. We have applied several strains cyclically to the geometry and using the developed model, we have predicted the life. Life is measured when the damage in the geometry increases and the solution becomes unstable because of the low stiffness of the model. The predicted results are shown in Fig. 4-10 for cells and cell boundaries. Similar curves from experiments are plotted in Fig. 4-10 using equation (4-11) and fatigue constants in Table 4-2.

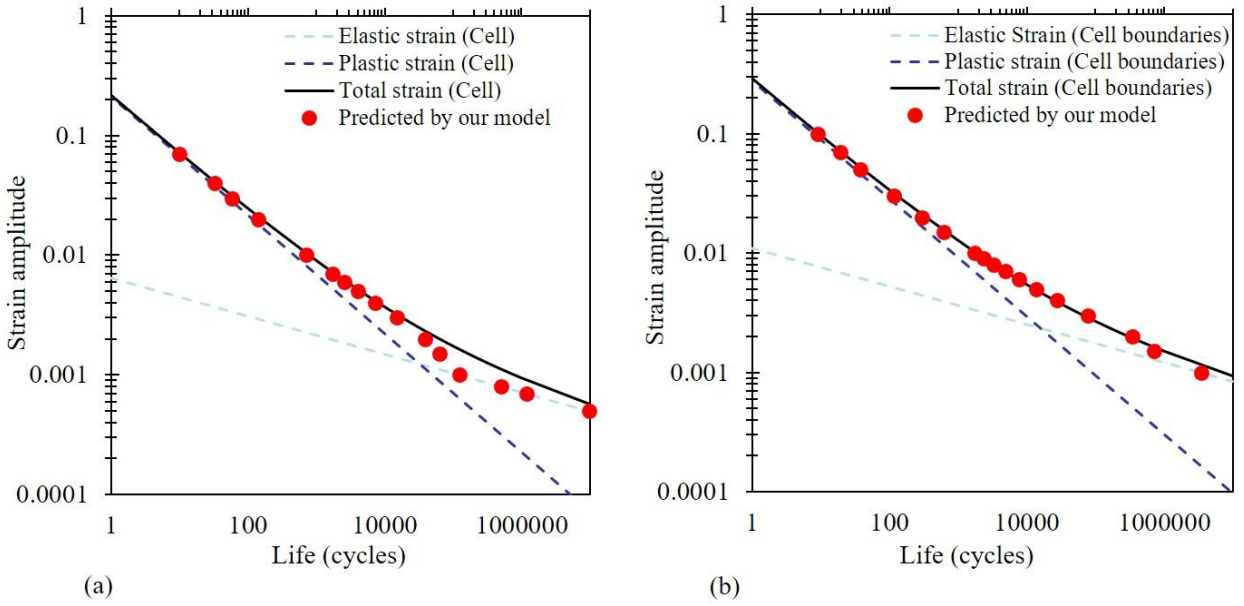

Fig. 4-10. Total strain amplitude versus life for (a) cell material and (b) cell boundary material. The model predicts the correct lives for both materials.

The results show a good fit between predicted lives by our model and experimental fit for both cell and cell boundary materials. It means the model is developed correctly and damage evolution law with weight function gives satisfactory results. There are other suggested methods in the literature [188, 190] for finding total damage rate like using the maximum or sum of elastic and plastic damage rates. These methods are examined within our model; however, none of them was predicting life as accurate as of the current approach. There is a slight difference

between predicted life and experimental fit in Fig. 4-10a in the high cycle fatigue region. This mismatch can be ascribed to the fact that experimental fit does not act perfectly at the transition between low cycle and high cycle fatigue.

4.2.5. Results and discussions

4.2.5.1. Life prediction of cellular microstructure

After verification of the model, two geometries are tested to find out the behavior of 3D printed cellular microstructure. One geometry is a cellular microstructure that makes the automatic generation of geometry easier for exploring various designs (Geometry 1 in Fig. 4-12). The other geometry is created based on the actual SEM images (Geometry 2 in Fig. 4-12). Strain-life curves for these geometries are obtained by running the simulations for various strain amplitudes as presented in Fig. 4-11. The results are compared to the cell and cell boundary fatigue responses. Predicted results are showing lower life compared to their constituent materials. One reason for decreased life can be that material strength mismatch causes stress concentrations at the interfaces or other places and reduces fatigue life. The damage will initiate at these local high stress or strain points and progress to the other areas. When there is no stress concentration in uniform material, it will degrade uniformly and can tolerate more cycles. Also, the realistic microstructure (Geometry 1) shows a slightly lower life compared to the other geometry (Geometry 2). The lower life can be associated with a less organized and non-uniform distribution of cell boundaries within cells in geometry 1.

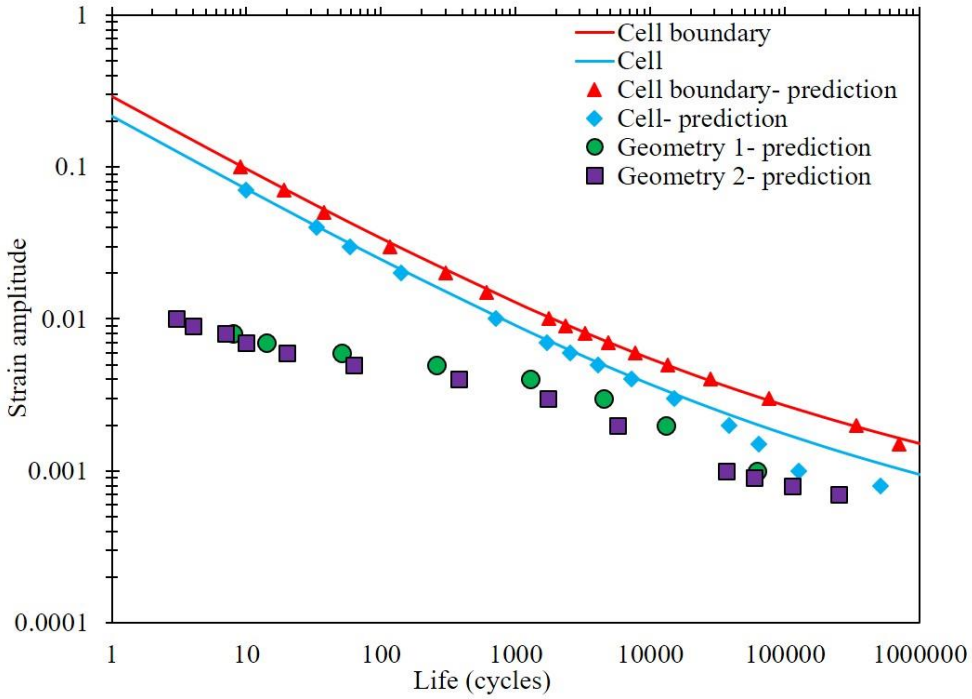

Fig. 4-11. Strain-life curves for two different geometries are plotted and compared to their constitutive materials (cell and cell boundaries) fatigue behavior. The results show lower life for a cellular microstructure compared to the cell or cell boundary fatigue life at the same strain level.

Fatigue damage contour plots of these two cellular microstructures with 0.5% strain amplitude are shown in Fig. 4-12 in progressive steps. Stages 1-3 show progressive damage initiation, propagation, and failure in the cellular microstructure.

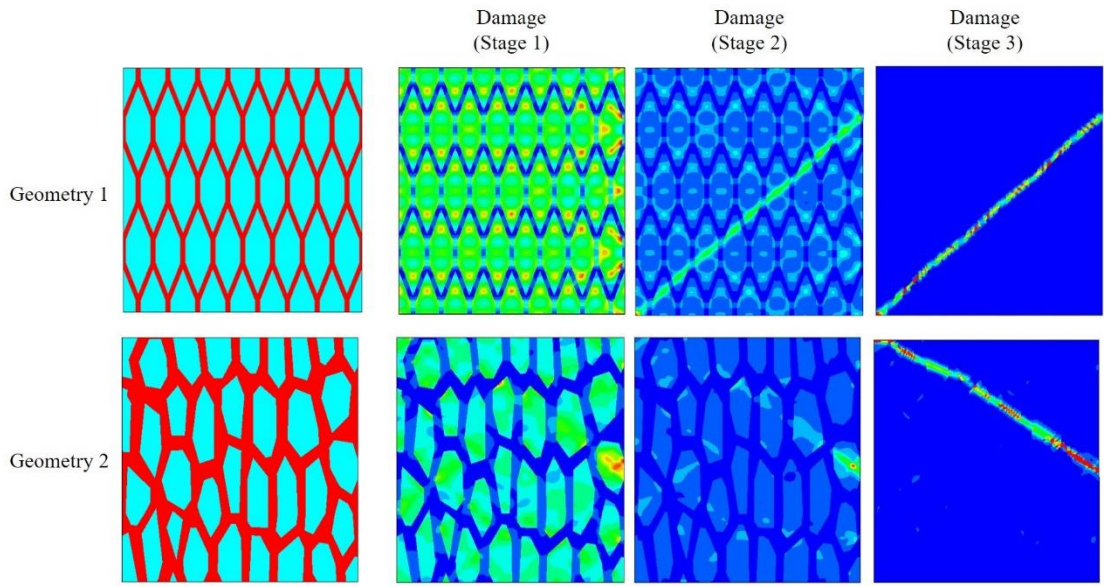

Fig. 4-12. Fatigue damage contour plots show different stages of damage initiation and propagation in two distinct geometries.

By looking at stress and strain contours, it was found that contour plots of damage are similar to the plastic strain distribution. The plastic strain is the most effective factor in the calculation of fatigue in high strains. Damage can initiate in any place on the basis of the geometry and initial maximum plastic strain. Damaged sites in different locations of the geometry finally reach together and form a linear damage pattern as shown in Fig. 4-12.

The cyclic stress-strain curve for geometry 2 is determined from reaction forces and displacement history of the bottom and top surfaces, and is plotted in Fig. 4-13a. Cyclic curve shape changes because of the damage parameter introduced into the model. The evolution of hysteresis loop peaks by increasing the number of cycles is illustrated in Fig. 4-13b. This figure shows the progressive damage that occurs in the structure where absolute values of maximum and minimum stresses decrease with cyclic loading. Near the end of the structure's life, damage evolves faster and peak stresses move toward zero.

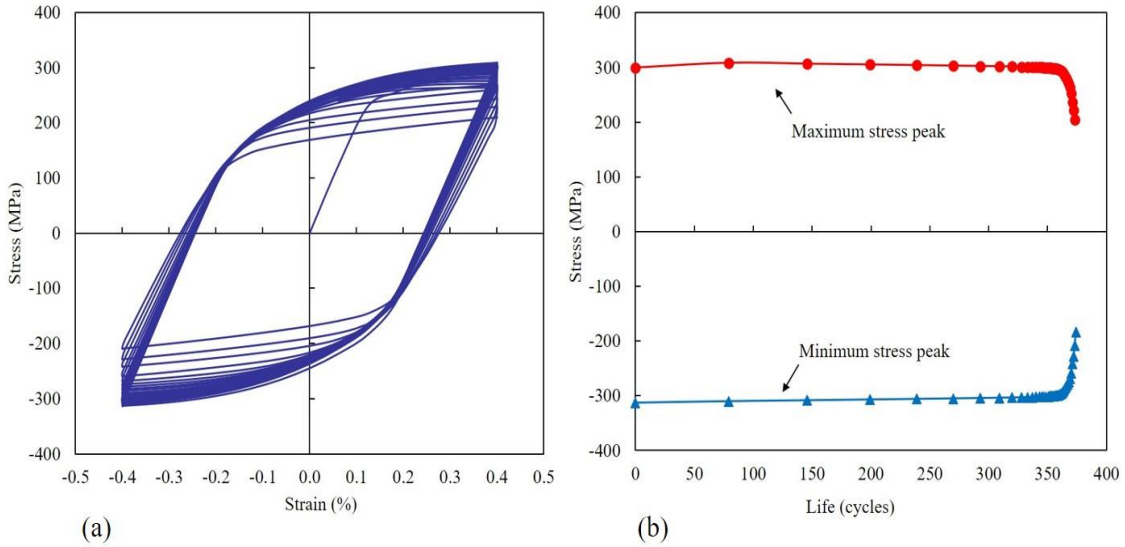

Fig. 4-13. (a) Stress-strain behavior of cellular microstructure (Geometry 2) under 0.4% cyclic strain amplitude. (b) Maximum and minimum stresses versus life curve that is obtained from peak stresses of (a)

4.2.5.2. Exploring various designs of cellular microstructure

After finding the fact that cellular microstructure reduces fatigue life, the question is how we can improve it. To answer this question, we have studied the effect of geometry parameters to find a way to improve fatigue performance. Cyclic displacement is applied to 27 geometries as explained in section 4.2.4.1, and five different strain amplitudes from 0.1 to 0.5% are tested (135 simulations in total). The strain-life plot obtained from these simulations is shown in Fig. 4-14. Changing geometric parameters of cellular microstructure causes variation in fatigue life. This variation is from 15% to 95% for 0.1% and 0.4% strain amplitudes, respectively.

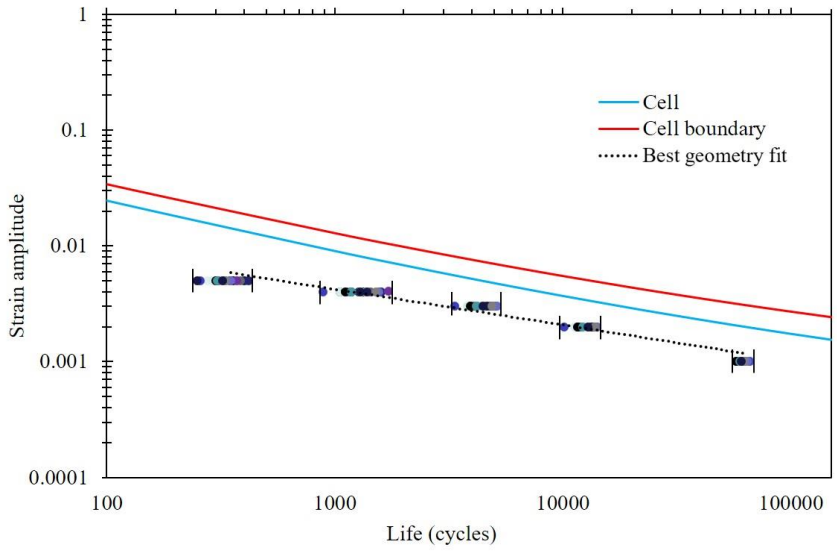

Fig. 4-14. Fatigue life estimation for different geometries and strains. Each point shows the life of a specific geometry and strain. Fatigue life in a specific strain amplitude for various geometries can change up to 95%.

In Fig. 4-15, the fatigue damage contour plots for the geometries with worst and best life (0.4% strain) are illustrated. The life changes from 890 to 1732 cycles in worst and best geometries, respectively. By looking at the damage plot of the worst geometry it can be seen that damage occurs inside the cell and also on the cell boundaries. For the best geometry, the damage is present mostly inside the cell.

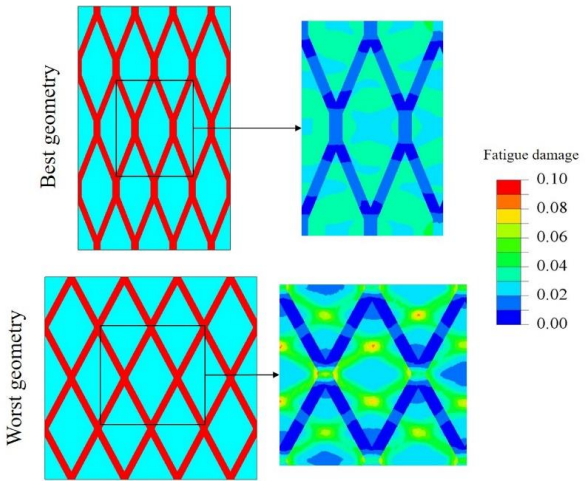

Fig. 4-15. Geometries with the best and worst fatigue life and their fatigue damage contour plot in the same cycle (146^{th} cycle)

In order to find out the effect of each geometric parameter in fatigue life, a life contour is presented in Fig. 4-16 (for 0.4% strain) by fixing one parameter and changing the other two parameters. For instance, the first row shows life variation by changing height and width for a fixed length. By looking at all plots it can be concluded that by increasing height and length, and reducing the width, life will be increased. In other words, elongated hexagons along the loading direction give the best life while the diamond shape cellular structure (like Fig. 4-15) has the worst life.

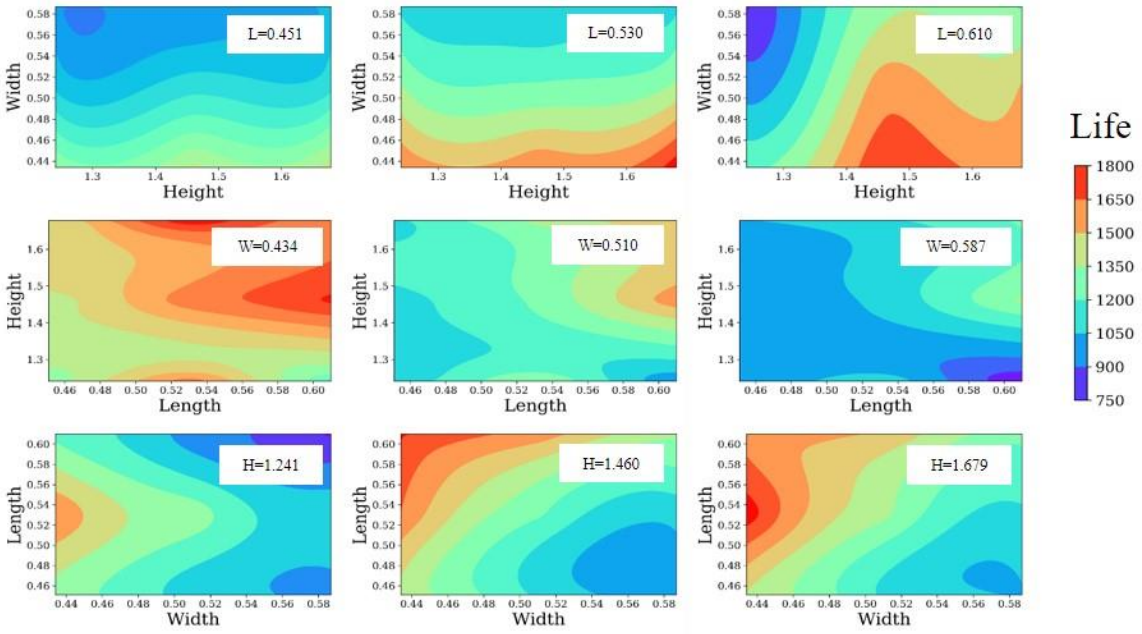

Fig. 4-16. Effect of geometric parameters on fatigue life of cellular microstructure

The results obtained from the fatigue damage model were also fitted to a Weibull distribution for characterizing the fatigue scatter. As discussed previously, 27 geometries and 5 strain amplitudes were considered. Weibull distribution is plotted for each strain amplitude in Fig. 4-17. The scatter in fatigue lives is more significant in high strains compared to low strains, which indicates that the effect of cellular microstructure on fatigue life is more dominant in low cycle fatigue. Furthermore, when strain amplitudes change from 0.1% toward 0.5% the Weibull slope decreases, which shows that life change due to cellular microstructure decreases. It can be concluded that cell geometry is more influential on fatigue life in lower cycles.

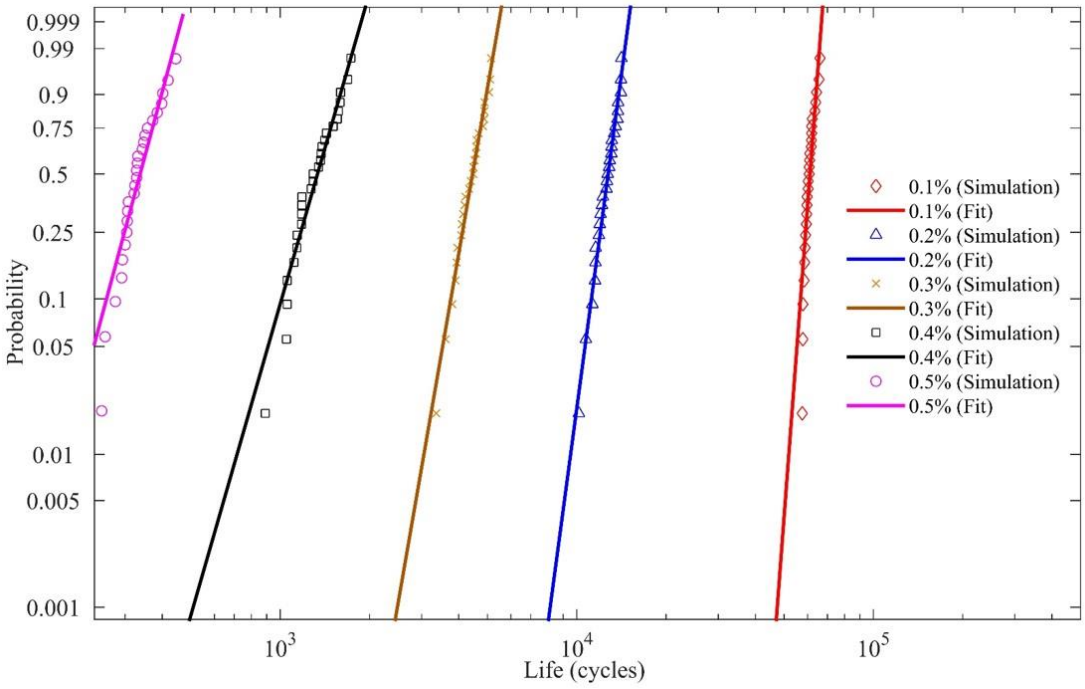

Fig. 4-17. Weibull distribution of predicted fatigue lives for different cellular microstructures (27 geometries) and 5 different strain amplitudes

4.2.6. Conclusions

In this research, the fatigue response at the microstructure of 3D printed alloys fabricated by SLM method is investigated. Our focus is on studying the interaction between the sub-grain cell structures and the low and high cycle fatigue lives. Damage-based fatigue models are employed to predict the fatigue life of the cellular microstructure. Different cellular microstructure topologies are created and fatigue life in these geometries under various loadings is compared together. The results show that elongated hexagons along the loading direction give the best life while diamond shape cellular structure has the worst life. The microstructure can be tailored by changing the processing parameters, and by knowing the geometrical features of microstructure which corresponds to an improvement in fatigue life, our results can be used as a guideline for 3D printing of alloys with an improved fatigue resistance. This study will be extended in future work by the authors to include all the microstructural parameters in the melt pools, grains, and cells that affect fatigue life.

Chapter 5

5. Fracture analysis and optimization of bio-inspired composites

Hybrid materials are created by combining the attractive mechanical properties of materials into one system. Combining materials with different mechanical properties, size, geometry, and order of different phases can lead to fabricating a new material with a wide range of properties. In the first part of this chapter, we discuss the computational modeling of damage propagation in a designed hybrid material inspired from biological materials like nacre. The second part of this chapter describes the optimization method we employed to find the optimum design for bio-inspired damage-tolerant structures instead of assuming one pre-designed structure. Different bio-inspired designs are presented in the literature and proposed a better mechanical behavior like toughness, strength and damage tolerance compared to their building blocks. Our goal is to look at this problem from another perspective. We found the optimum distribution of soft and stiff phases in composite material to improve the strength and toughness of the material.

5.1. Fracture analysis of bio-inspired composites

5.1.1. Overview

Biological materials like nacre or bone have shown superior mechanical behavior compared to their simple building blocks. This feature belongs to the specific geometry and arrangement of building blocks. Studying these structures will help us create hybrid materials with improved mechanical behavior. With the help of 3D printing technology, we are able to fabricate and test different designs and compare them with the building components. Computational methods are also useful to reduce the cost and increase the efficiency of analysis.

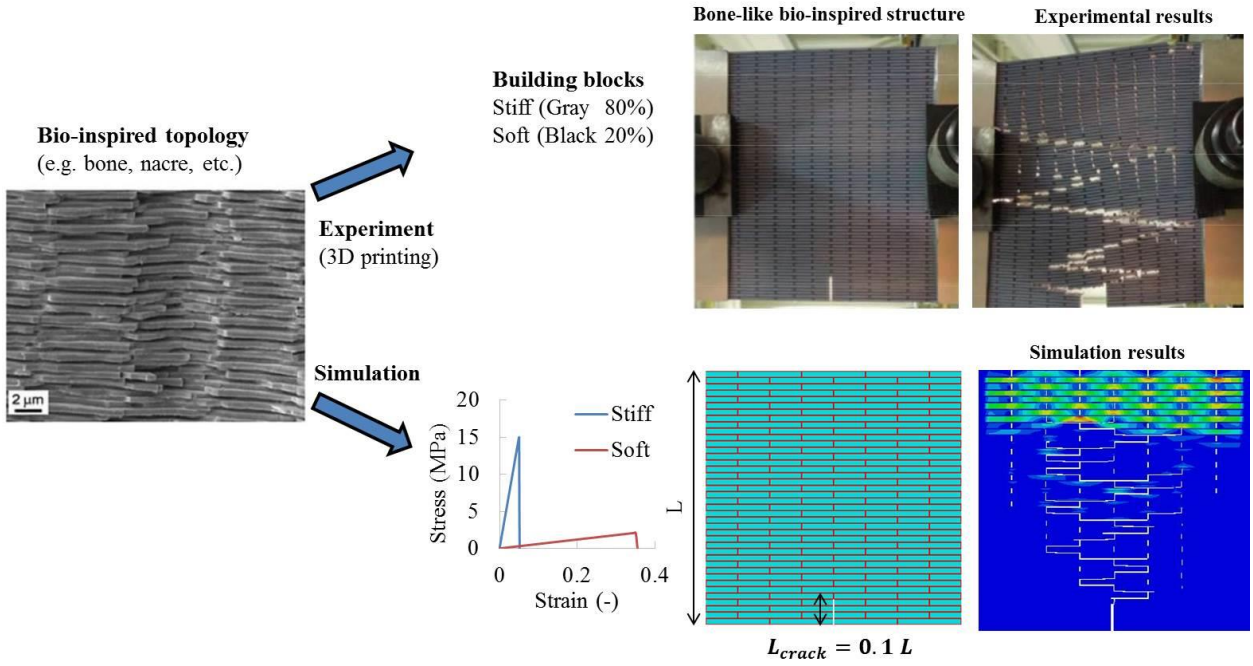

Fig. 5-1. Approach used in this research for fracture analysis is illustrated. Computational results show a similar crack propagation pattern to the tensile test result of the bio-inspired 3D printed structure [101].

A process flow for our approach is shown in Fig. 5-1. Based on simple building blocks (stiff and soft materials) and inspired from biological materials, we have created a computational model to compare the findings with the experimental results [101] of tensile tests.

5.1.2. Computational approach: Finite Element Model

In this work, our focus is mostly on computational approaches for damage propagation analysis. Geometry and material models for damage analysis are described in the following.

5.1.2.1. Geometry

A bone-like structure similar to the designed structure in [101] is simulated with the finite element method. The hierarchical structure helps delocalizing stress and increasing cracks propagation time by restricting cracks movements. The stiff and soft phases are shown in blue and red in Fig. 5-2, respectively, with 20% soft and 80% stiff phase. A pre-existing crack is defined in the model to study the fracture behavior in the bone-like composite.

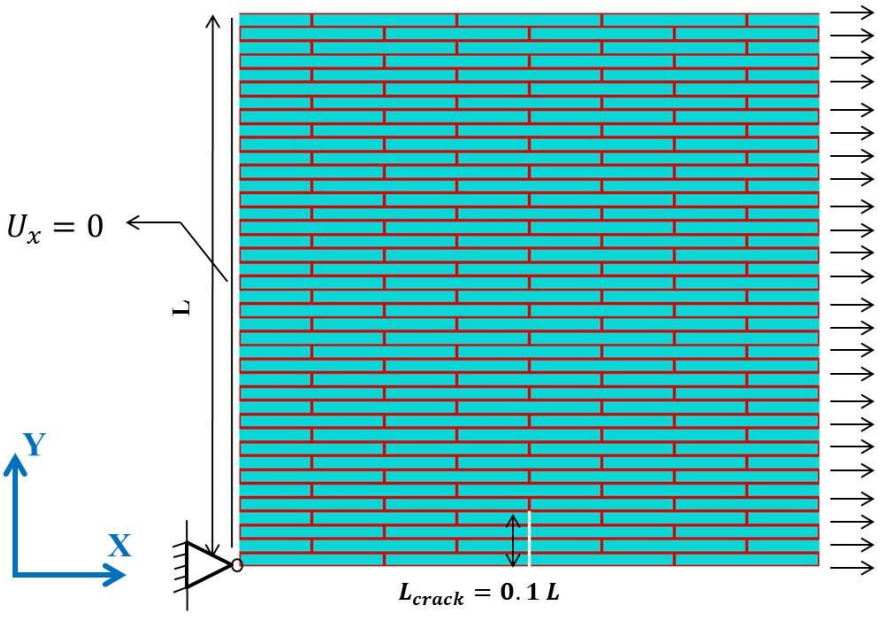

Fig. 5-2. Bone-like geometry used in this study, which has two stiff (blue) and soft (red) phases. A pre-crack is implemented in geometry to study the fracture behavior.

5.1.2.2. Material model

In order to compare computational results with experiments, we need to define material properties similar to experiments (3D printed materials). For the tensile tests [101], an Objet Connex500 multi-material printer was used to manufacture bio-inspired designs, using two polymers with distinct mechanical properties. VeroWhitePlus (VW+) and TangoBlackPlus (TB+) polymers were used for stiff and soft phases, respectively. VW+ has the stiffness of 2000-3000 MPa and elongation of 15-25 %, while TB+ has stiffness of lower than 1 MPa and elongation of 170-220 % [101, 191]. The difference between the stiffness of materials is very high and it makes computational analysis unstable. In addition, it is found that 3-4 % of materials at the interfaces are mixed with each other during manufacturing, which makes the soft material stiffer. Therefore, the stiffness ratio is lower compared to the actual stiffness ratio.

We used the stiffness ratio of 50 as suggested in [101], and assumed near-identical toughness for both polymers. Fracture strain for stiff and soft phases is assumed to be 5% and 35%, respectively (shown in Fig. 5-3).

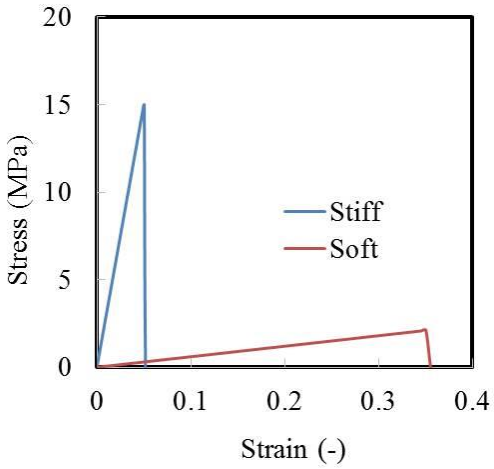

Fig. 5-3. Material behavior defined for stiff and soft phases in the finite element analysis.

The ductile damage criterion in Abaqus is used to implement element deletion in the model. A very small plastic strain is defined for damage evolution, which means we have elastic-damage behavior for both materials, and plastic strain is neglected. When stress in a material reaches its yield strength, failure happens in the element and Abaqus removes the failed element from the simulation. By using this method, we can see the evolution of damage inside the bone-like structure.

5.1.3. Results and discussions

In order to simulate the tensile test correctly, it is important to apply proper boundary conditions. To this end, a displacement is applied to the right boundary of bone-like geometry (see Fig. 5-2), and the left boundary is constrained in the loading direction. The lower-left corner is constrained in all directions to eliminate the rigid body motion. The Quasi-static step in Abaqus is used for analysis since it provides more stability than the Static step in the current study. The geometry is meshed with a 4-node bilinear plane stress element (CPS4). A blunt crack (10% and 30% of the geometry dimension) is introduced in the geometry, and results are compared with geometry without crack. In Fig. 5-4, a comparison is made between simulation and experimental results [101] for the composite geometry with a 10% pre-crack. A zigzag pattern is observed for the crack propagation path, which is very similar in both cases.

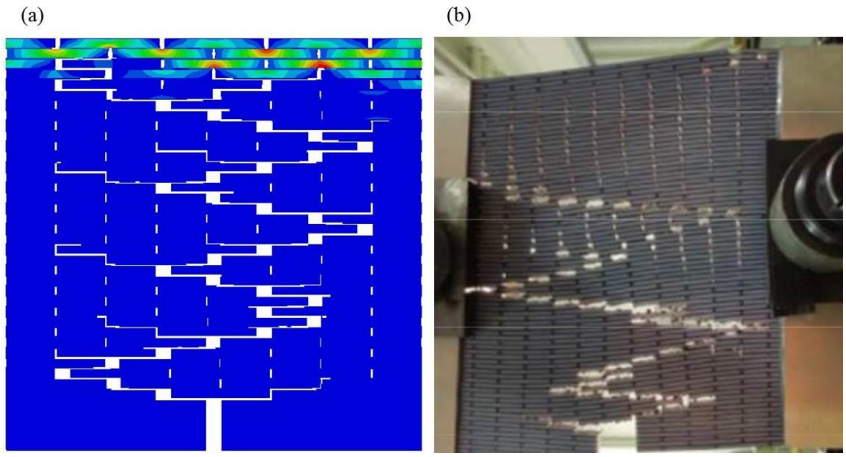

Fig. 5-4. Crack pattern for bio-inspired composite (with 10% pre-crack) is very similar in a) simulation, and b) experiment [101].

Crack bridging exists in several locations in the geometry, and many small cracks form in different places before the failure happens. Distribution of soft materials in the structure reduces the propagation rate, and interlock cracks.

Stress-strain plots for simulated case studies are plotted in Fig. 5-5. Stiff material shows a sudden fracture after yield, while composite material absorbs energy after the start of crack propagation.

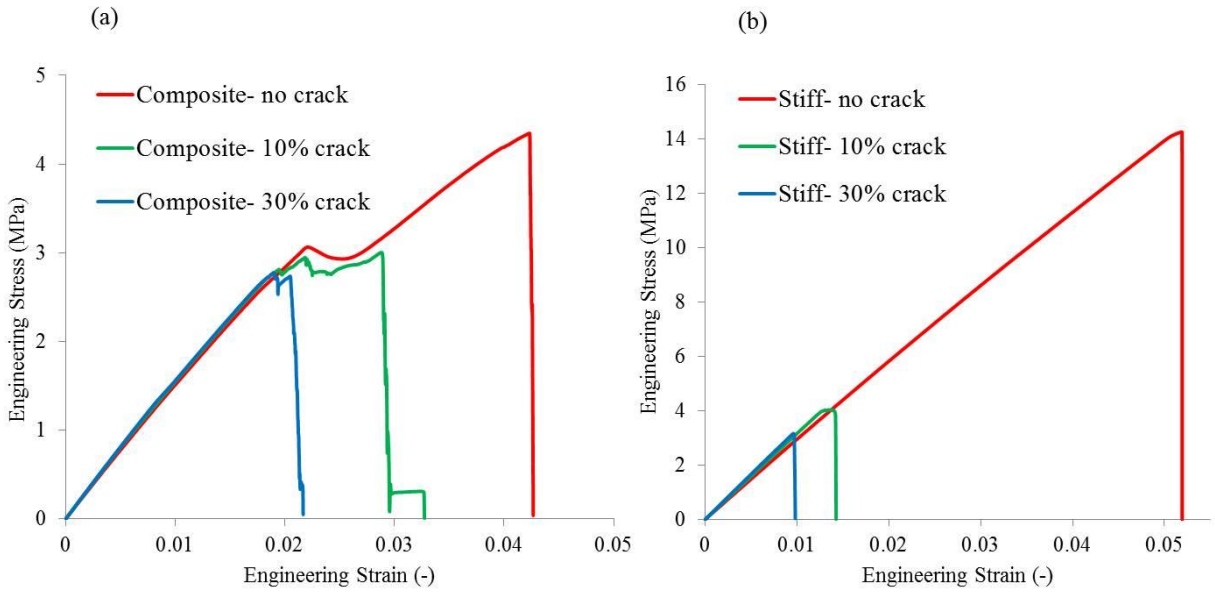

Fig. 5-5. Stress-strain response for (a) composite and (b) stiff materials for cases without crack, and with 10% and 30% crack length.

Stiff material loses most of its fracture strength when a pre-crack is implemented in the geometry. It does not happen for the composite geometry, and fracture strengths for 10% and 30% geometries are near to the fracture strength of without crack geometry. This effect is shown in Fig. 5-6a. For Stiff material, the fracture strength reduces to 26% and 21% of its original value, by introducing 10% and 30% pre-crack in the model, respectively. In the composite structure, the fracture strength reduces to 74% and 68% of its original strength for the same pre-cracks. This means that the combination of soft and stiff materials in a designed structure maintains most of its original strength by reducing the crack propagation rate, and the sensitivity of structure to the presence of crack is much smaller than stiff material. For the stiff material, crack directly propagates through the pre-existing crack as shown in Fig. 5-6b, while the crack changes its direction in the composite material (shown in Fig. 5-6c).

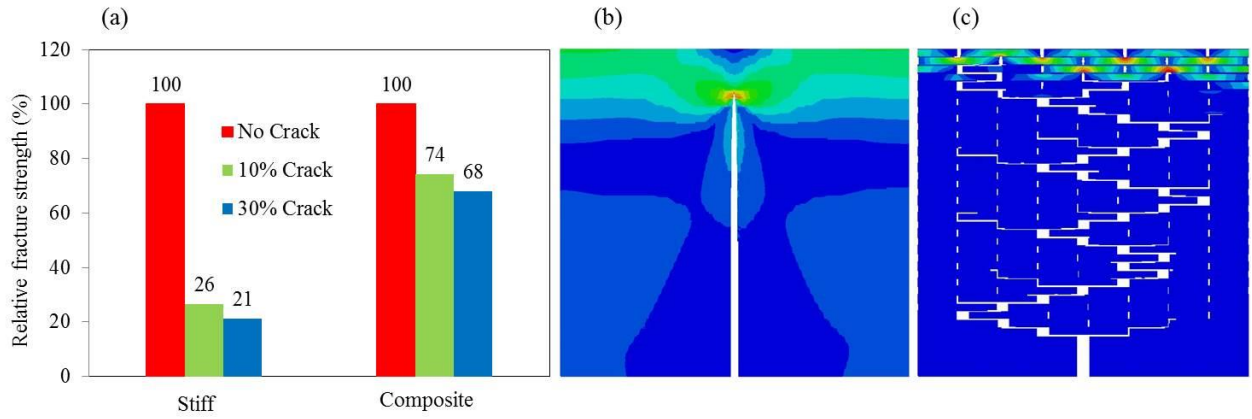

Fig. 5-6. (a) relative fracture strength (%) for stiff and composite material for different pre-cracks shows that stiff material loses most of its strength with defining pre-crack in the geometry, while composite material maintains most of its strength. It shows that hierarchical structure shows lower sensitivity to the presence of crack compared to stiff material. Crack propagates directly through the pre-crack for (b) stiff material while it has a zigzag pattern for (c) composite material.

In addition, the stress-strain response of stiff material with a 10% crack is compared with the composite material with the same pre-crack. The results depicted in Fig. 5-7, show that the hierarchical structure is adding toughness to the structure, while 20% of constituents are made of very low strength material (soft material).

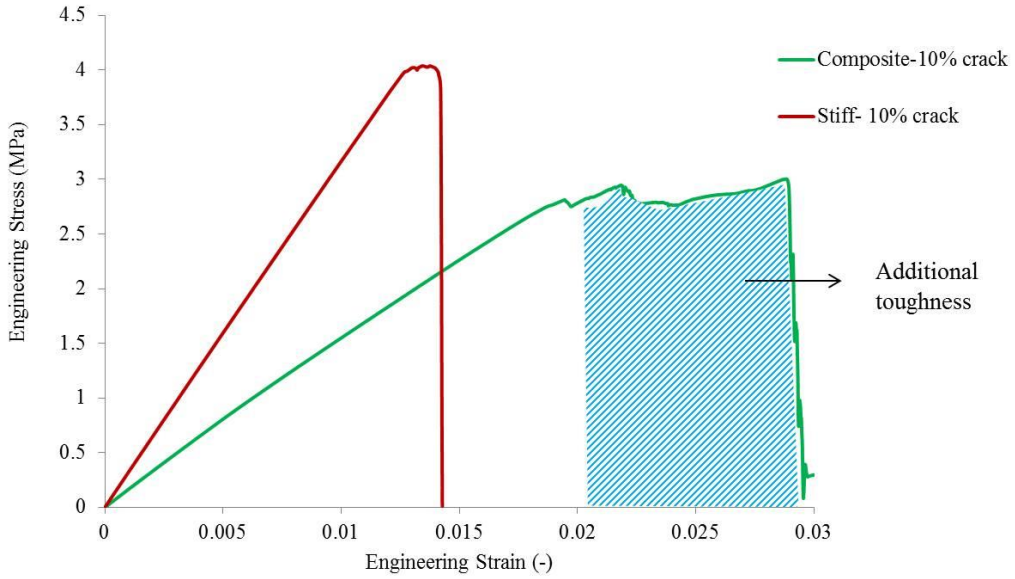

Fig. 5-7. Composite material with 10% pre-crack shows a higher toughness compared with the stiff material with the same pre-crack, due to hierarchical structure.

Furthermore, it is observed that there are two peaks in the stress-strain curve of composite structure [101], and a similar trend is found in the simulation results (see Fig. 5-8). This behavior is studied by comparing different stages of loading. At point 1 in Fig. 5-8a, first cracks initiate in the structure and cause a drop in the stress-strain curve. This drop continues up to point 2, where most of the soft elements perpendicular to the loading reach failure. After this point, the hierarchical structure blocks the initiated cracks, and the material stretches along with the gradual propagation of cracks. The horizontal soft layers bind the structure together through shear strain action. At point 3, local cracks join and rapid failure occurs. Fig. 5-8b shows the experimental results of the composite structure. The trend is similar to simulation results (Fig. 5-8a), with more nonlinearity due to the nonlinear behavior of photopolymers used in the 3D printed composite.

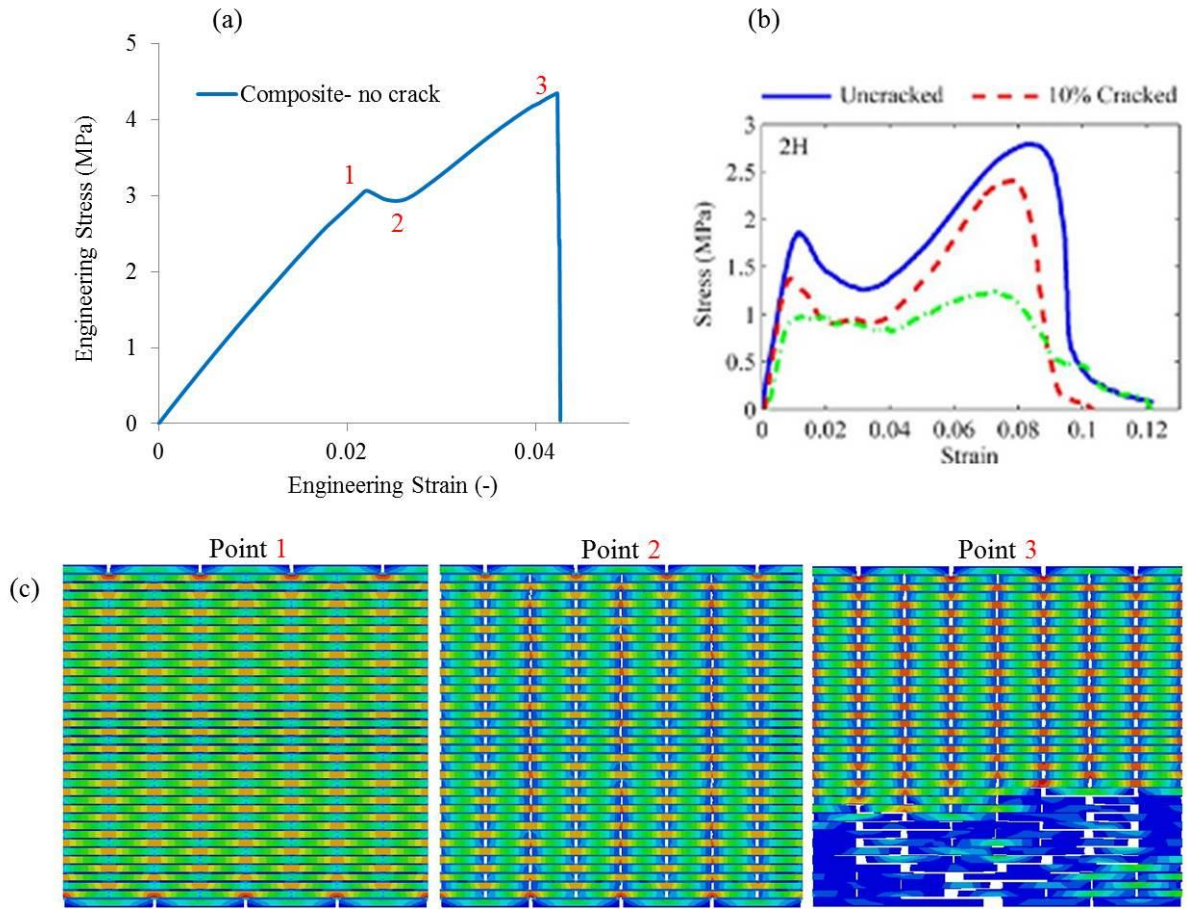

Fig. 5-8. Comparison of stress-strain curve for bio-inspired composite without crack yields similar trends in both (a) simulation, and (b) experiments [101]. The stress-strain curve shows two peaks at points 1 and 3 in (a). At point 1 first cracks initiate, and stress drops because of failed vertical soft elements as shown in (c). Then, structure resists more up to point 3, where cracks join and propagate rapidly up to complete failure.

Fig. 5-8c shows the stress contour of the deformed structure at different points mentioned in Fig. 5-8a (points 1, 2, 3). This figure illustrates initial cracks at point 1, distributed failed soft material at point 2, and final unstable crack at point 3.

The same response is observed in the tensile test of the composite without crack as shown in Fig. 5-9. Vertical soft elements at different places fail initially, and cause delocalization and distribution of stress. With applying more loads, horizontal soft layers fail and join previous cracks, and structure fails rapidly.

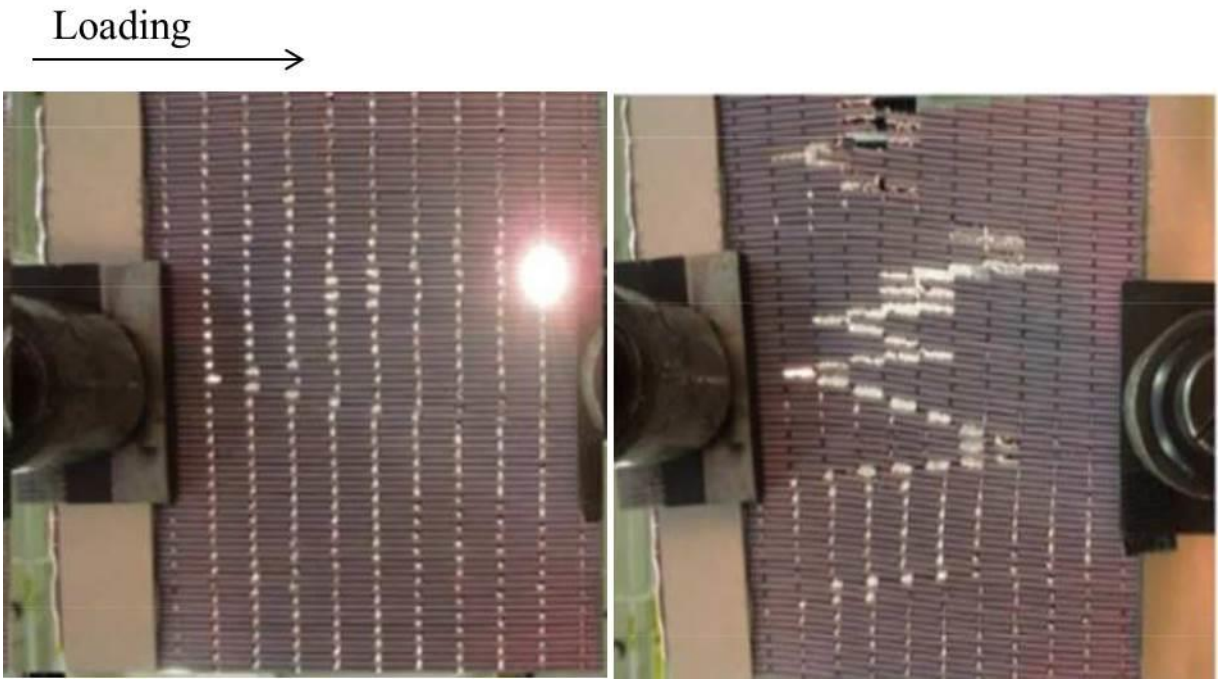

Fig. 5-9. Two different stages of tensile test of the bio-inspired composite without crack show the initial failure of soft materials in different locations, and then the final failure of structure with more loading [101].

5.2. **Optimum design for damage-tolerant multi-material composites**

5.2.1. Overview

Creating a composite with superior properties by mixing multiple constituents of inferior mechanical performance has been a long-standing problem. To address this problem, we propose a novel framework that is constructed on the concurrent integration of computational mechanical analysis and optimization. The goal is to mimic nature's capability of producing multi-phase materials with complementary properties, but with a generality for selecting any loading condition, and the property to be optimized. For this purpose, we pose a design problem to find the optimum distribution of soft and stiff phases in composite materials to improve the strength of the material. A finite element analysis is first coupled with a numerical scheme for optimizing the distribution of stiff and soft blocks to achieve the best mechanical performance. Next, machine learning techniques are applied to create a reduced-order representation of the problem to achieve the optimum design in a computationally efficient way. Two case studies with one and

three cracks are studied. The results showed 289% and 171% increase in toughness compared to the base material toughness for one crack and three cracks models, respectively. Furthermore, the current optimization process resulted in a 54% increase in toughness compared to similar research in the literature.

5.2.2. Methods

An optimization problem is defined by finding the optimum distribution of soft and stiff phases in a composite structure. A method that combines an optimization algorithm and finite element method is used to solve this problem. A detailed description of each method is presented in the following sections.

5.2.2.1. Finite element model

A composite structure of 8×8 elements is created from soft and stiff phases. The volume fraction of the soft phase is assumed to be 12.5% of the total material, and the remainder will be the stiff phase. The stiffness of stiff and soft phases is considered 1000 and 100 MPa, respectively. Toughness is defined as the area under the stress-strain curve and assumed to be equal for both materials. Fracture strain of stiff material is presumed to be 10%, and the corresponding strain for soft material will be 31.6% (based on the equal toughness for stiff and soft phases). Each element that reaches its fracture strain limit will be removed from the simulation. The stress-strain behavior of stiff and soft phases is illustrated in Fig. 5-10a. A displacement-controlled boundary condition is applied to the right side of the model, and symmetric boundary condition is applied to the left side as shown in Fig. 5-10b. The symmetric boundary condition will cause a considerable decrease in computational time. An edge crack with 25% of specimen length is introduced at the lower boundary normal to the loading direction. In order to compare the performance of our model with literature, the structure and material properties are selected similar to [192].

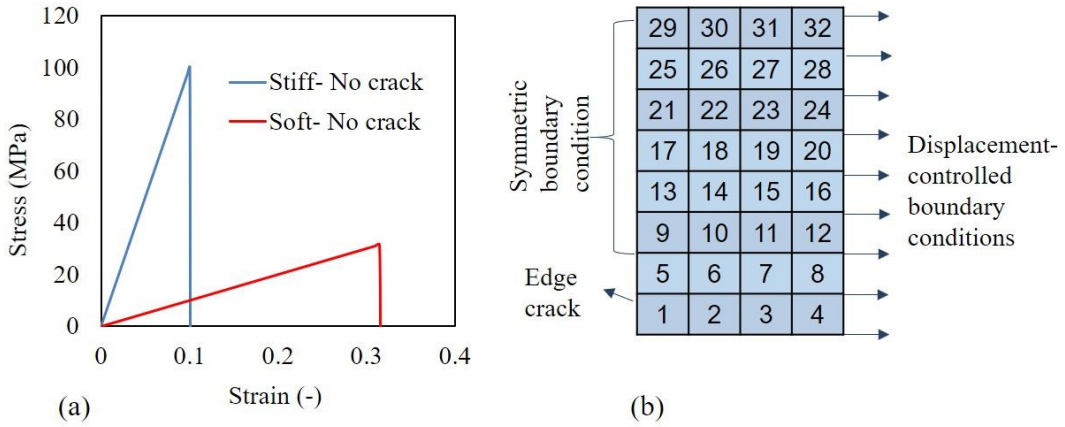

Fig. 5-10. (a) Stress-strain behavior of stiff and soft materials, and (b) schematic of the computational model with boundary conditions and an edge crack

5.2.2.2. Optimization strategy

The main goal of the optimization problem is to find the distribution of the soft and stiff phases that improves several performance metrics. These include the maximization of the toughness and minimization of the stress concentration factor (SCF), as will be discussed in section 5.2.2.4. The structural model introduced in the previous section is a high-fidelity model, where the computational time requirement of each simulation is directly correlated with the finite element mesh density. The mesh resolution also defines the number of variables to be optimized as each element is assumed to be made of either the soft or stiff phase. Our optimization strategy is based on the identification of the distribution of the soft elements, as the number of soft elements will be less than the stiff elements in our applications. The optimum distribution of the soft phase is found by obtaining numbers that represent the particular elements having soft material. This leads to a design optimization problem, where the design variables are discrete element numbers.

The optimization problem is solved with the Non-Dominated Sorting Genetic Algorithm (NSGA-II) [193-195], which is a computational time-efficient genetic algorithm (GA) solver that can also handle several discrete variables. A combination of the GA and finite element method has generated satisfactory results in different applications [196-198]. The selection of the NSGA-II algorithm guarantees the identification of the global optimum solution as against the gradient-based optimization algorithms, even for the problems having discrete design variables. However, with the increase in the problem dimension and number of design variables, the main structural

model becomes infeasible due to the computational time requirement since a considerable number of iterations are needed to achieve the optimum solution. Therefore, we introduce a novel computational strategy based on the use of ML algorithms to create a surrogate of the original structural model. The ML techniques require the training step by generating samples to identify the relationship between the input and output parameters. This step involves the computational simulations that are performed with the structural model. To enable a computationally efficient strategy for surrogate model generation, the number of design variables is minimized by introducing a sensitivity analysis before the training of the ML algorithm. The number of design variables is determined with the sensitivity analysis in the first step, and the surrogate model is generated for the reduced number of variables. Next, the NSGA optimization is performed on the ML-generated surrogate model.

A similar problem for the determination of the optimized phase distributions in nature-inspired materials was studied in [192] using an ML-reinforced strategy. This strategy was focused on the generation of labels to classify the outputs of the simulations and optimization with respect to the information collected by the labels [192]. However, in this approach, the stored information is limited by the definition of different labels as well as the number of training samples, which can lack achieving a global optimum solution. In addition, the label classification typically leads to a more expensive computational problem because of the need for more training samples compared to the regression-type ML algorithms. Therefore, in this work, we use a regression-type supervised learning strategy to build the surrogate model. To handle the discrete optimization variables, we use the GA algorithm solution, which also guarantees to find the global optimum designs. Although the GA algorithms are known to be computationally expensive compared to the widely-used gradient-based optimization, we improve the computational efficiency using the NSGA-II algorithm and utilizing the surrogate model with ML. A visual representation of our computational solution strategy is given in

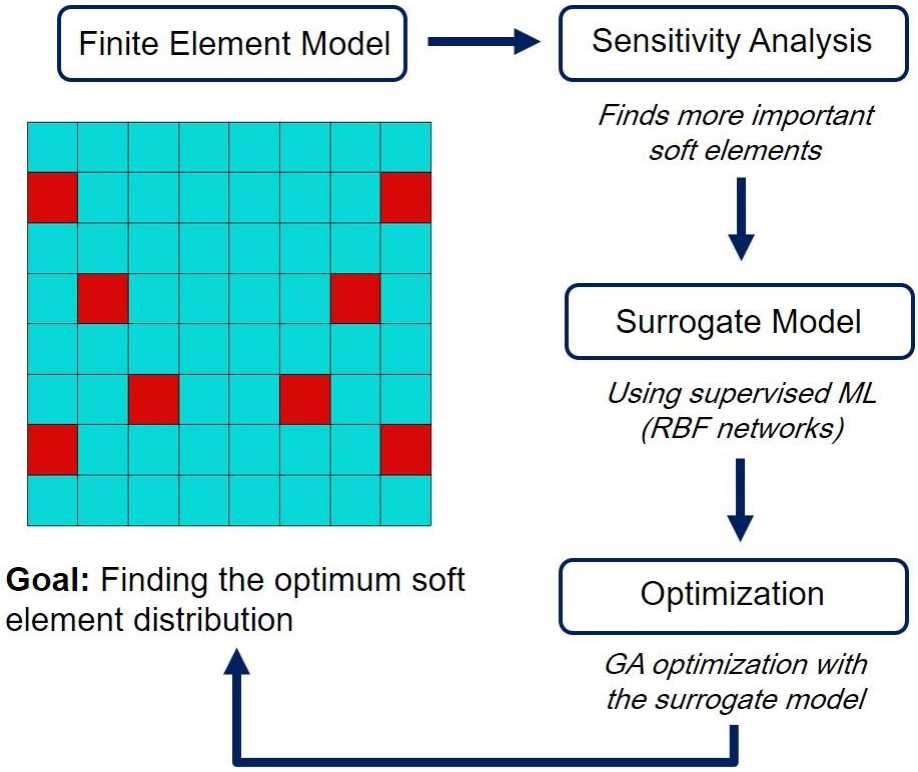

Fig. 5-11. Visualization of our optimization strategy

The first step is the sensitivity analysis that computes the relative changes in the objective functions with the change in the soft element numbers. The structural model is used to perform the sensitivity study by assuming constant soft element numbers, except one. This particular element is changed in each iteration to understand how individual elements affect the objective function values. With the sensitivity analysis, the more important elements, which are observed to lead more changes in the objective functions, are defined as the optimization variables. This approach significantly reduces the size of the design space from all potential elements to all important elements. The training of the ML algorithm is performed with the samples that are generated for the important elements.

The second step involves the generation of the surrogate model using the supervised ML approach, RBF network. The RBF network includes an input layer, hidden layer(s), and output layer as shown in Fig. 5-12. The input layer stores the information for the optimization variables, hidden layers define the relationship between optimization variables and objective functions, and the output layer describes the objective functions. Each of the components of the n-dimensional input vector, $\boldsymbol{x}$, feeds the system information and forwards to m basis

functions on the hidden layer. The outputs of the basis functions (or the hidden layers in general) are linearly combined with the weights, w (w_1, w_2, …, w_m), to compute the objective function, $f(x)$.

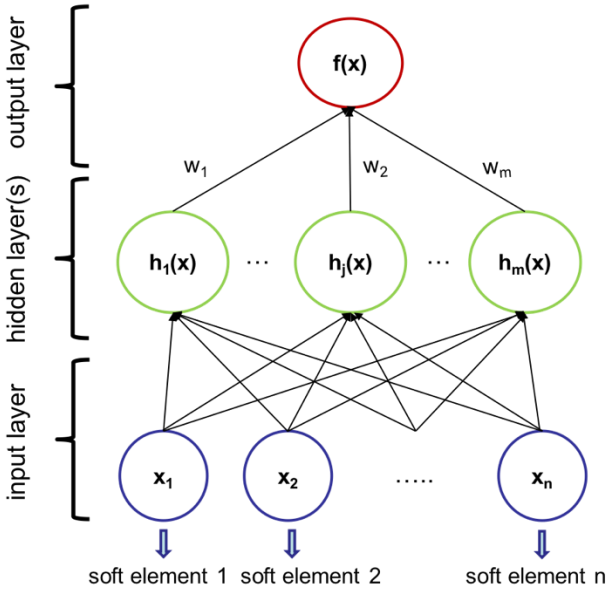

Fig. 5-12. A generic representation of the RBF network

The RBF network is generated with 25 hidden layers in this work using the Gaussian function representation given as [111]:

$$h(x) = \exp\left(\frac{-(x-c)^2}{r^2}\right) \tag{5-1}$$

where c (center) and r (radius) are the hyper-parameters of the Gaussian RBF and they are solved with the following minimization problem:

$$min\ z = ||Y_* - Y|| \tag{5-2}$$

where Y_* and Y are the objective function values of the RBF prediction and training samples respectively. The number of training samples is determined for each application by solving the minimization problem with Sequential Quadratic Programming for $z < 10^{-12}$.

5.2.2.3. Benchmark study for validation

Our optimization strategy is verified with a benchmark study to find the optimum distribution of the soft elements using a finite element mesh (8×8) with no crack. In this problem, half of the total elements are assumed to be made of the soft phase. The training of the ML model is performed with 100 design samples for soft elements. The GA optimization is performed on the ML-generated surrogate model to maximize the stiffness. To verify our solution, we compute the stiffness values of all possible combinations using the main structural model owing to the small problem dimension. The maximum stiffness values and optimized structures are shown in Fig. 5-13. The optimized stiffness solution is also validated with the theoretical result (rule of mixture) [199].

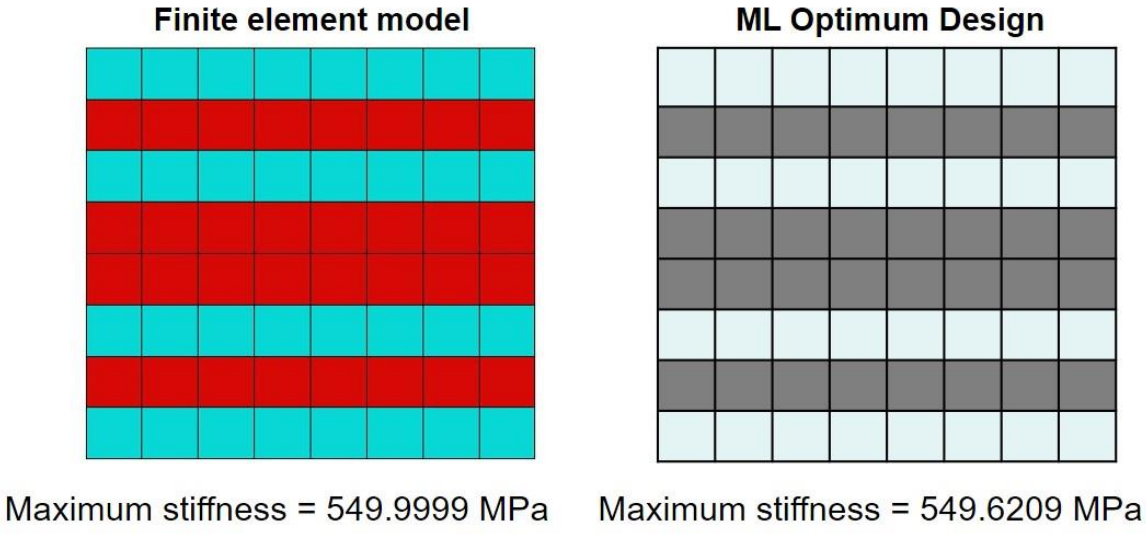

Fig. 5-13. Optimum results obtained with the main structural model and the presented design strategy

5.2.2.4. Definition of objective functions

Objective functions can change based on the application of composite [200, 201]. In this study, we want to optimize toughness, stress concentration, and a combination of toughness and stress concentration. At the same time, we do not want to lose the stiffness of the composite; however, with the current volume fraction of (12.5%) soft phase, stiffness does not change a lot. Toughness is the ability of a material to absorb energy and can be calculated as the area under the stress-strain curve. We want to distribute stress in the structure and avoid places with high stresses. Therefore, we have defined a parameter called stress concentration factor (SCF) as

$$SCF = \frac{Maximum\ von\ Mises\ stress}{Average\ von\ Mises\ stress} \tag{5-3}$$

where maximum and average von Mises stresses are the maximum and averaged von Mises stress values respectively, that are computed in the elastic region for all elements. By combining the toughness and SCF, we have defined another parameter with the goal of maximizing toughness and minimizing SCF at the same time. Since orders of toughness and SCF are different, we have normalized each parameter by its stiff (or soft) phase. For instance, T_0 and SCF_0 are defined as the toughness and stress concentration factor of the stiff (or soft) phase, respectively. It is worth mentioning that toughness values of stiff and soft phases were assumed to be equal, and the stress concentration factor is independent of the material in single-phase. Therefore, T_0 and SCF_0 are equal for stiff and soft materials. Three objective functions are introduced as

$$\begin{aligned} f_1 &= max\ (\frac{T}{T_0}) \\ f_2 &= min\ (\frac{SCF}{SCF_0}) \\ f_3 &= min\ (\frac{T_0}{T} \times \frac{SCF}{SCF_0}) \end{aligned} \tag{5-4}$$

These objective functions are calculated after each finite element simulation and were utilized for optimization purposes.

5.2.3. Results and discussion

Different cases have been studied to find the optimum solution for the composite structure. Firstly, a 16×16 model with one edge crack is created, and three objective functions are evaluated. After selecting one of the objective functions, a larger model (64×64) is created and evaluated by the selected objective function. In order to study the effect of different crack positions, a model with three cracks is generated, and the optimum distribution is found by our optimization approach. These cases are discussed in the following sections.

5.2.3.1. Comparison of different objective functions

A 16×16 model consisting of an edge crack is created, and three different objective functions introduced in section 5.2.2.4, are studied. The distribution of soft and stiff elements is shown in Fig. 5-14a for each objective function. The results are compared with their constituent materials toughness and SCF (T_0 and SCF_0). Employing maximum toughness objective function resulted in a 101% increase in the toughness of base material. Using minimum stress concentration objective function yielded an 18% decrease in stress concentration. Combined toughness and stress concentration factor objective function (min SCF/T) showed 59% decrease compared to the stiff material value (SCF_0/T_0). Fig. 5-14b illustrates stress-strain plots for different objective functions. Minimum SCF/T shows better results compared to other objective functions since it has the largest stiffness and strength value. Furthermore, the corresponding toughness to this objective function is almost the same as the value found by the maximum toughness objective function. Therefore, the combined toughness and stress concentration factor objective function (minimum SCF/T) will be used for the larger models and other case studies.

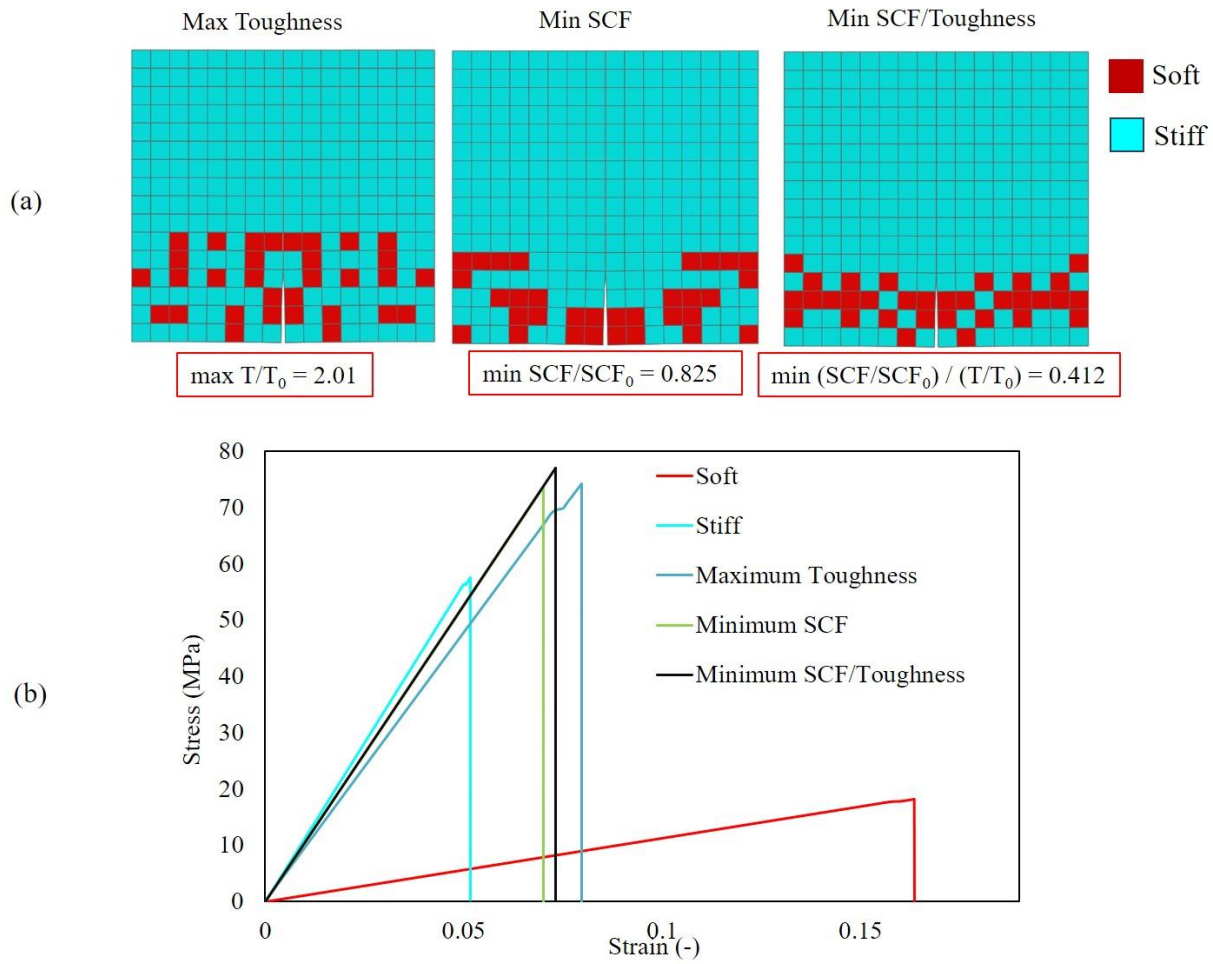

Fig. 5-14. (a) Distribution of soft and stiff elements in a pre-cracked structure for different objective functions. (b) Stress-strain response of different objective functions compared to the stiff and soft response

5.2.3.2. Comparison with literature

In order to validate the performance of the current approach, the results are compared to a similar study in the literature by Gu et al. [192]. All the material properties, size of pre-crack, soft element percentage, and objective function (toughness) are the same for both models. Fig. 5-15a depicts the stress-strain behavior for these two cases as well as soft and stiff material behavior. By comparing the results, it is found that our optimum design shows 54% better performance (more toughness) compared to the literature results. Furthermore, the current optimum design has more strength and stiffness based on the stress-strain plot in Fig. 5-15a. The distribution of soft and stiff elements for these two studies is illustrated in Fig. 5-15b and Fig. 5-15c. In both cases,

soft elements are distributed near the crack, while our result shows more dispersed soft elements in stiff matrix compared to the literature results.

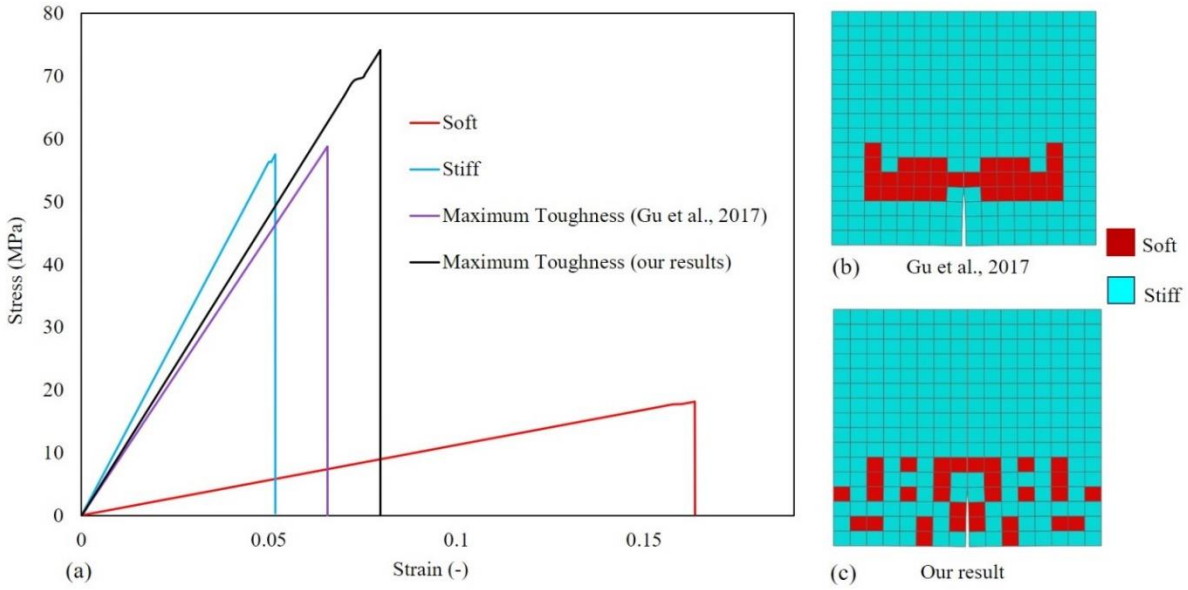

Fig. 5-15. (a) Stress-strain behavior of current approach compared to similar research [192] with maximum toughness objective function. (b) Distribution of soft and stiff elements in [192] and (c) our results

5.2.3.3. Effect of crack position and number of cracks

A larger model of 64×64 elements is generated to increase the accuracy of the results. The combined objective function of stress concentration factor and toughness (SCF/T) had the best performance in section 5.2.3.1 and therefore is employed in further studies. Firstly, an edge crack is introduced to the model, and the stress-strain response is plotted in Fig. 5-16a. The optimum design led to a 289% increase in toughness and a 38% decrease in stress concentration. The distribution of soft elements in the composite is presented in Fig. 5-16b, which shows dispersed soft elements near the middle crack. These soft elements near crack cause delocalization of strain and make the structure tougher and stronger.

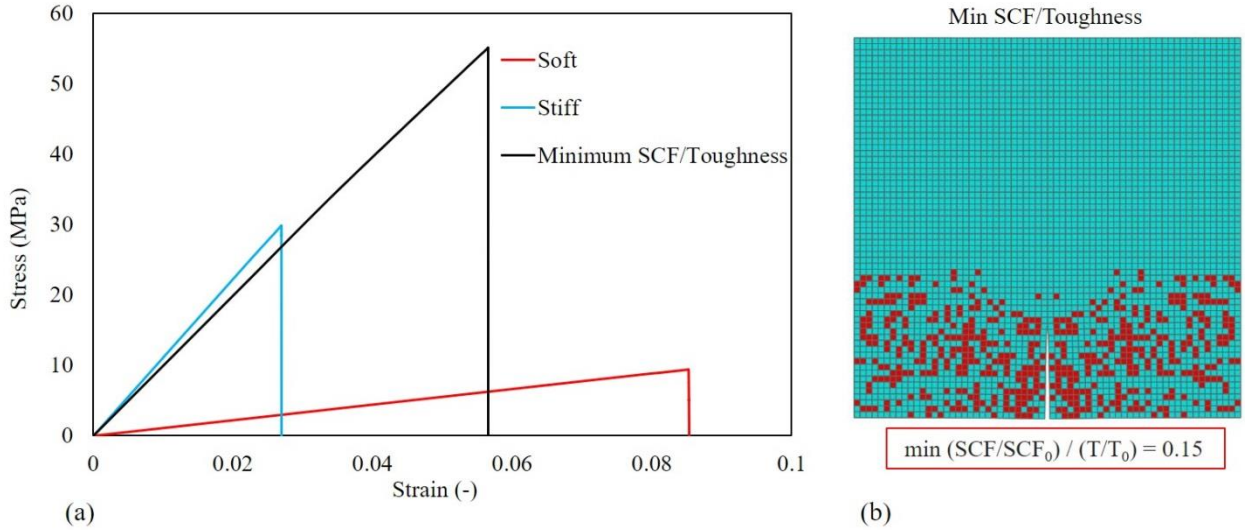

Fig. 5-16. (a) Stress-strain response of 64×64 model with optimized SCF/toughness objective function compared to soft and stiff responses. (b) Optimum distribution of soft and stiff elements

In order to study the effect of crack position and number of cracks, two additional oblique cracks with the same size as the edge crack, are introduced into the previous model. Fig. 5-17a depicts the stress-strain response of the new model with three cracks. It is found that toughness is increased by 171%, and stress concentration is reduced by 23% compared to their base material behavior. Optimum distribution of soft and stiff elements is illustrated in Fig. 5-17b. In this figure, soft elements are distributed around the crack tip, which reduce the stress concentration at the crack tip and distribute the stress and strain.

A stress decrease and the following increase are observed in the stress-strain response of three cracks model in Fig. 5-17a. In order to study this behavior, von Mises stress contour plots of the model along with the failed elements are shown in Fig. 5-17c for points 1 to 3 of Fig. 5-17a. First elements fail at the lower edge of the oblique crack, and damage propagation continues perpendicular to the loading direction up to point 2. At this point, the damage reaches soft elements near the lower edge crack and damage propagation stops. Structure resists damage propagation up to point 3, and at this point damage near the upper edge of oblique crack propagates and structure fails after point 3. It is interesting that first failure and further propagation did not occur near the lower edge crack. It can be due to the delocalization of stress near the crack caused by a larger number of soft elements.

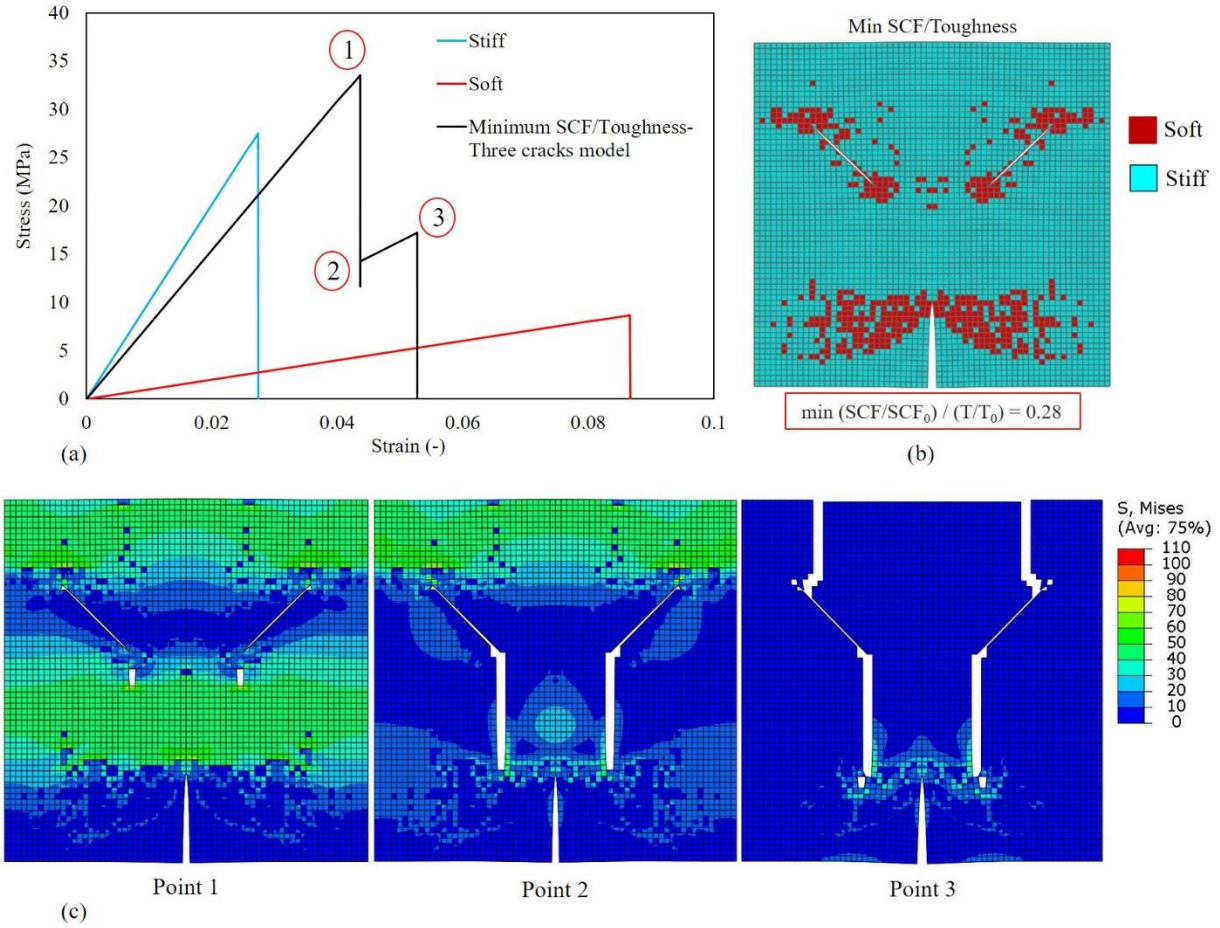

Fig. 5-17. (a) Stress-strain response of three cracks model with 64×64 elements and optimized SCF/toughness objective function compared to the base material response. (b) Optimum distribution of soft and stiff elements. (c) von Mises stress contour plots show damage initiation and propagations sites of three points marked in (a)

5.2.3.4. Discussion

Due to the former limitation of manufacturing processes, it was not easy to combine different phases of materials with the desired design. Nowadays, with 3D printing technology, we are capable of fabricating various combinations of materials. With the growth in computational power and optimization processes, we can design enhanced composites, and by utilizing 3D printing, we can validate and then fabricate our design. Based on the presented results in this research, it is clear that the proposed optimization process can lead to a significant improvement

in the mechanical performance of the composite structure of stiff and soft materials. Adding a small percentage of soft material can increase the toughness of a composite up to 2-3 times, and make it more damage tolerant. Soft elements cause stress delocalization, and more uniform stress distribution is observed around the cracks, compared to large stresses near crack tips in single-phase materials. The proposed method can be applied to various structures with a different combination of materials depending on the application. Further efforts are required to make the current method more efficient in solving larger problems. It is also important to have finer mesh near the crack tips, and optimize fracture mechanics parameters like fracture toughness, energy release rate and crack growth rate.

5.2.4. Conclusions

To sum up, our study provides a framework for a new way to optimize the composite structures of stiff and soft building blocks with single or multiple cracks. The proposed framework utilizes the finite element method, genetic algorithm, and machine learning to find the optimum design. By adding the soft material to the stiff phase, the distribution of stress around the cracks changes and causes a tougher and stronger structure. By comparing three different objective functions, it was found that maximizing toughness and minimizing stress concentration factor at the same time leads to the better mechanical performance of the structure. In the case of a model with one pre-crack, an increase of 289% in toughness and a 38% decrease in stress concentration factor were obtained from the optimum design. The model with multiple cracks showed an increase of 171% in toughness and a 23% decrease in stress concentration factor. A considerable increase in toughness (54%) has been achieved using the current approach compared to the efforts in the literature. Obtained results show significant improvement in structure compared with the base constituent, and increases motivation for further research in this area. Further efforts are intended to improve the efficiency of the method for larger structures, and employing smaller mesh around the crack tips. From a fracture mechanics perspective, objective functions like fracture toughness, energy release rate and crack growth rate can be considered for different applications.

Chapter 6

6. Contributions to the field and future studies

The major outcome of this research is establishing a novel computational framework to study fatigue and fracture across different scales. This framework will significantly improve the accuracy of currently available methodologies for investigating the fatigue and fracture response of materials in a broad range of applications. We particularly have focused on applying our multiscale method to study the fatigue and fracture response of rolling contact in rails (chapters 2 and 3), additively manufactured metals (chapter 4), and bio-inspired hierarchical structures (chapter 5). The developed model helps manufacturers to design more fatigue and fracture resistant microstructure in rails, 3D printed metals, and bio-inspired materials.

The results in each mentioned application can also help to find novel methodologies to improve the mechanical properties of the material in the other applications as well. The study on bio-inspired materials that consist of stiff and soft layers can be extended to study the effect of lamellar microstructure in pearlitic rails consisting of cementite (brittle) and ferrite (ductile) layers. The arrangement and thickness of each layer can be engineered by methods we employed in studying bio-inspired materials to find the best performing rail material against wear and RCF. Furthermore, the developed model for studying RCF in addition to the results we found in 3D printed metal applications can be used as a comprehensive tool to investigate RCF failure in 3D printed knee implants fabricated by selective laser melting method.

In this final chapter, we provide our contributions and future works in detail for each chapter.

6.1. Contributions to the Field

There are lots of experimental and computational studies on rolling contact fatigue with applications in rails, bearings, and gears in the literature; however, explicit simulation of microstructure at the contact patch of wheel and rail, and computational study of rolling contact fatigue in the rails at the microstructural level, as considered in our method, is a new contribution to the field. This research has a significant impact on the field of studying contact fatigue since

microstructure plays an important role in RCF behavior, and including a more detailed microstructure in the computational studies will help to fabricate more RCF-resistant rails. Furthermore, the numerical study of the ambient temperature effect on RCF is performed for the first time. The results suggest more frequent inspections of rails during cold weather because of the higher chance of RCF failure. Also, with the help of finite element analysis, we studied the effect of partial slip condition on the RCF from a new perspective and validated the results with the experimental observations. The method we developed and employed for our fatigue study of RCF can be used by researchers to solve the complex behavior of steel under rolling contact condition. This study on RCF confirms the previous observation of subsurface cracks in the rail, and it suggests to the railroad industry to use appropriate inspection methods to find a network of subsurface cracks that form in case of lower traction forces.

The research on 3D printed alloys specifically SLM is relatively new, and most of the researches in this area are experimental studies. Since experiments on 3D printed alloys are considerably time-consuming and expensive, computational analysis is a proper alternative to reduce cost and time. Our method for studying the fatigue at the microstructural level of 3D printed alloys is pioneering with no similar work is available in the literature. Our studies can be a first step toward establishing comprehensive numerical frameworks to investigate fatigue behavior of 3D metallic devices with complex geometries, fabricated by 3D printing. Changing 3D printing processing parameters like laser speed and power leads to fabricating samples with various microstructures. By knowing the fracture and fatigue resistant microstructures, we can change the processing parameters to reach the desired microstructure. Although this is an ongoing field of research, our study moves these efforts one step forward.

In chapter 5, we combined the fracture analysis with designing bio-inspired materials. An optimization methodology is implemented into the designing procedure for the first time, which enables us to perform the bio-inspired material design with the target of finding the most efficient geometries that can resist defects in their structure. In this research, we use novel optimization methods and also combine these methods with machine learning. This study can be used as an effective reference for creating damage-tolerant structures with improved mechanical behavior.

6.2. **Future Works**

In chapters 2 and 3, we covered the methods we developed to study rolling contact fatigue at the microstructural level, and how we implemented these methods into a finite element model. The research on the rolling contact fatigue can be extended to study the effect of texture (distribution of grain orientations). The initial study was performed on the effect of texture by comparing untextured with textured microstructure. Textured microstructure had <111> orientations of the lattice structure aligned along the rolling direction while an untextured microstructure had random orientation distribution. Preliminary results showed that textured microstructure has a better life than an untextured microstructure. This study needs to be performed with a higher detailed microstructure and to be validated with experiments. Furthermore, a series of experiments can be performed to find the effect of texture and suggest modifications to the manufacturers. Another suggested work is to use the developed framework to study the RCF in biomedical applications like knee implants which are important areas of research for the medical industry.

The performed research on 3D printed metallic alloys (chapter 4) is part of a more detailed study that needs to be continued to get more details on fracture and fatigue behavior of 3D printed alloys. Additional research on the effect of different types of melt pool boundaries on fracture behavior can be performed. It is observed that there are two kinds of melt pool boundaries (layer-layer and track-track), which behave differently under mechanical loading. The effect of these two melt pool boundaries can be studied in future studies. Furthermore, we assumed perfect grain boundaries at grain interfaces. Actual grain boundary properties based on microhardness experiments can be considered in future studies to see which one of melt pool boundaries and grain boundaries are more susceptible to fracture.

In the research on the fatigue behavior of cellular microstructure in 3D printed metals, the geometry was a simplified assumption for cellular microstructure. We used simplified geometries in order to be able to use an automated process for creating and exploring high number of geometries. A similar study can be performed by considering more realistic geometries obtained from SEM images of various 3D printed samples. In this way, we will move one step forward to find the cellular microstructure effect on the fatigue life of 3D printed metals by the SLM method. The current best geometry for fatigue performance in cellular

microstructure is not the optimum solution since only 27 geometries have been explored and simulated. Further studies can be performed on finding the optimum solution using the current best geometry as a starting point for optimization with a gradient based method. Another assumption made in this study was that fatigue life is attributed to the cellular microstructure only; however, it is necessary to include other microstructural features like grains, grain boundaries, melt pools, melt pool boundaries, and porosities into fatigue studies of 3D printed metals at the microstructural level, since cellular microstructure is not the only effective microstructural feature on the fatigue behavior. In order to include all these features, it is suggested to use multiscale approaches to create more accurate models due to computational efficiency and coupled analysis. In addition, the effect of temperature and residual stresses, as well as more complicated loading, can be considered.

In chapter 5, we studied the fracture behavior of bio-inspired materials and then we focused on finding an optimum design to improve the toughness and strength of bio-inspired composite materials. Despite extensive research on fracture analysis of bio-inspired materials, there is no specific effort on studying these materials under cyclic loading. Mechanical fatigue is the cause of almost 90% of all failures in materials; therefore, it is important to study the fatigue behavior of bio-inspired materials. Future works can be focused on finding the fatigue properties of building block materials and use the computational approach to simulate fatigue damage in bio-inspired composite structures.

The optimum results can be 3D printed by different materials like steel and polymer to gain a better understanding of bio-inspired structures. An interesting field of research can be studying fracture and fatigue in multi-material structures and trying to find the optimum solution for these structures that can be 3D printed by mixing different percentages of materials in a 3D printer to obtain different stiffness and strength. Optimization algorithms also can be improved to perform faster and simulate larger structures. Furthermore, the current optimum result can be used as a starting point for future studies.

List of Publications

Journal Papers

- M. Ghodrati, M. Ahmadian, R. Mirzaeifar, "Three-dimensional study of rolling contact fatigue using crystal plasticity and cohesive zone method", *International Journal of Fatigue*, 2019
- MT. Andani, M. Ghodrati, MR. Karamooz-Ravari, R. Mirzaeifar, J. Ni, "Damage modeling of metallic alloys made by additive manufacturing", *Material Science and Engineering A*, 2019
- M. Ghodrati, M. Ahmadian, R. Mirzaeifar, "Modeling of Rolling Contact Fatigue in Rails at the Microstructural Level", *Wear*, 2018
- M. Ghodrati, P. Acar, R. Mirzaeifar, "Optimum design for damage-tolerant multi-material composites with improved toughness and strength", (under review)
- M. Ghodrati, R. Mirzaeifar, "Computational Study of Fatigue in Sub-grain Microstructure of 3D Printed Alloys", (under review)

Conference Proceeding

- M. Ghodrati, M. Ahmadian, R. Mirzaeifar, "Studying the Effect of Tangential Forces on Rolling Contact Fatigue in Rails Considering Microstructure", *ASME Joint Rail Conference*, 2019
- M. Ghodrati, M. Ahmadian, R. Mirzaeifar, "Investigating the rolling contact fatigue in rails using finite element method and cohesive zone approach", *ASME Joint Rail Conference*, 2018
- MT. Andani, MR. Karamooz-Ravari, M. Ghodrati, R. Mirzaeifar, J. Ni, "Development of a Microstructural-based Computational Model for Predicting the Mechanical Properties of Metals Manufactured by Additive Manufacturing", *TMS Annual Meeting & Exhibition*, 2019
- M. Ghodrati, P. Acar, R. Mirzaeifar, "A Generalized Nature-Inspired Optimization Method: Additively Manufactured Materials with Superior Mechanical Performance", *TMS Annual Meeting & Exhibition*, 2019

References

1. Grassie, S.L., *Rolling contact fatigue on the British railway system: treatment.* Wear, 2005. **258**(7): p. 1310-1318.
2. Magel, E.E., *Rolling contact fatigue: a comprehensive review.* 2011. p. No. DOT/FRA/ORD-11/24. 2011.
3. Ringsberg, J., M. Loo-Morrey, B. Josefson, A. Kapoor, and J.H. Beynon, *Prediction of fatigue crack initiation for rolling contact fatigue.* International Journal of Fatigue, 2000. **22**(3): p. 205-215.
4. Weinzapfel, N., F. Sadeghi, and V. Bakolas, *An Approach for Modeling Material Grain Structure in Investigations of Hertzian Subsurface Stresses and Rolling Contact Fatigue.* Journal of Tribology, 2010. **132**(4): p. 041404.
5. Ekberg, A., E. Kabo, J.C.O. Nielsen, and R. Lundén, *Subsurface initiated rolling contact fatigue of railway wheels as generated by rail corrugation.* International Journal of Solids and Structures, 2007. **44**(24): p. 7975-7987.
6. Dirks, B., R. Enblom, A. Ekberg, and M. Berg, *The development of a crack propagation model for railway wheels and rails.* Fatigue & Fracture of Engineering Materials & Structures, 2015. **38**(12): p. 1478-1491.
7. Brouzoulis, J. and M. Ekh, *Crack propagation in rails under rolling contact fatigue loading conditions based on material forces.* International Journal of Fatigue, 2012. **45**: p. 98-105.
8. Zhang, J. and Y. Jiang, *Fatigue of polycrystalline copper with different grain sizes and texture.* International Journal of Plasticity, 2006. **22**(3): p. 536-556.
9. Bennett, V.P. and D.L. McDowell, *Polycrystal orientation distribution effects on microslip in high cycle fatigue.* International Journal of Fatigue, 2003. **25**(1): p. 27-39.
10. Guilhem, Y., S. Basseville, F. Curtit, J.M. Stéphan, and G. Cailletaud, *Investigation of the effect of grain clusters on fatigue crack initiation in polycrystals.* International Journal of Fatigue, 2010. **32**(11): p. 1748-1763.
11. Raje, N., T. Slack, and F. Sadeghi, *A discrete damage mechanics model for high cycle fatigue in polycrystalline materials subject to rolling contact.* International Journal of Fatigue, 2009. **31**(2): p. 346-360.
12. Sadeghi, F., B. Jalalahmadi, T.S. Slack, N. Raje, and N.K. Arakere, *A Review of Rolling Contact Fatigue.* Journal of Tribology, 2009. **131**(4): p. 041403.
13. Warhadpande, A., F. Sadeghi, M.N. Kotzalas, and G. Doll, *Effects of plasticity on subsurface initiated spalling in rolling contact fatigue.* International Journal of Fatigue, 2012. **36**(1): p. 80-95.
14. Noyel, J.P., F. Ville, P. Jacquet, A. Gravouil, and C. Changenet, *Development of a Granular Cohesive Model for Rolling Contact Fatigue Analysis: Crystal Anisotropy Modeling.* Tribology Transactions, 2016. **59**(3): p. 469-479.
15. Bomidi, J.A.R., N. Weinzapfel, F. Sadeghi, A. Liebel, and J. Weber, *An Improved Approach for 3D Rolling Contact Fatigue Simulations with Microstructure Topology.* Tribology Transactions, 2013. **56**(3): p. 385-399.

16. Franklin, F.J., J.E. Garnham, D.I. Fletcher, C.L. Davis, and A. Kapoor, *Modelling rail steel microstructure and its effect on crack initiation.* Wear, 2008. **265**(9-10): p. 1332-1341.
17. Slack, T. and F. Sadeghi, *Cohesive zone modeling of intergranular fatigue damage in rolling contacts.* Tribology International, 2011. **44**(7-8): p. 797-804.
18. Simonovski, I. and L. Cizelj, *Automatic parallel generation of finite element meshes for complex spatial structures.* Computational Materials Science, 2011. **50**(5): p. 1606-1618.
19. Boots, B.N., *The arrangement of cells in "random" networks.* Metallography, 1982. **15**(1): p. 53-62.
20. Fritzen, F., T. Böhlke, and E. Schnack, *Periodic three-dimensional mesh generation for crystalline aggregates based on Voronoi tessellations.* Computational Mechanics, 2009. **43**(5): p. 701-713.
21. Zhang, P., D. Balint, and J. Lin, *An integrated scheme for crystal plasticity analysis: Virtual grain structure generation.* Computational Materials Science, 2011. **50**(10): p. 2854-2864.
22. Grassie, S.L., *20 - Maintenance of the wheel–rail interface,* in *Wheel–Rail Interface Handbook*. 2009, Woodhead Publishing. p. 576-607.
23. Li, W. and B. Liu, *Experimental investigation on the effect of shot peening on contact fatigue strength for carburized and quenched gears.* International Journal of Fatigue, 2018. **106**: p. 103-113.
24. Magel, E.E., *Rolling contact fatigue : a comprehensive review.* 2011.
25. Arakere, N.K., N. Branch, G. Levesque, V. Svendsen, and N.H. Forster, *Rolling Contact Fatigue Life and Spall Propagation of AISI M50, M50NiL, and AISI 52100, Part II: Stress Modeling* Tribology Transactions, 2009. **53**(1): p. 42-51.
26. Pandkar, A.S., N. Arakere, and G. Subhash, *Microstructure-sensitive accumulation of plastic strain due to ratcheting in bearing steels subject to Rolling Contact Fatigue.* International Journal of Fatigue, 2014. **63**: p. 191-202.
27. Garnham, J.E. and C.L. Davis, *The role of deformed rail microstructure on rolling contact fatigue initiation.* Wear, 2008. **265**(9-10): p. 1363-1372.
28. Alley, E., K. Sawamiphakdi, P. Anderson, and R. Neu, *Modeling the Influence of Microstructure in Rolling Contact Fatigue.* Journal of ASTM International, 2010. **7**(2): p. 1-20.
29. Jalalahmadi, B. and F. Sadeghi, *A Voronoi FE Fatigue Damage Model for Life Scatter in Rolling Contacts.* Journal of Tribology, 2010. **132**(2): p. 021404.
30. Ahmadi, A., R. Mirzaeifar, N.S. Moghaddam, A.S. Turabi, H.E. Karaca, and M. Elahinia, *Effect of manufacturing parameters on mechanical properties of 316L stainless steel parts fabricated by selective laser melting: A computational framework.* Materials & Design, 2016. **112**: p. 328-338.
31. Li, L., L. Shen, and G. Proust, *Fatigue crack initiation life prediction for aluminium alloy 7075 using crystal plasticity finite element simulations.* Mechanics of Materials, 2015. **81**: p. 84-93.
32. Taheri Andani, M., M. Ghodrati, M.R. Karamooz-Ravari, R. Mirzaeifar, and J. Ni, *Damage modeling of metallic alloys made by additive manufacturing.* Materials Science and Engineering: A, 2019. **743**: p. 656-664.
33. Alley, E.S. and R.W. Neu, *Microstructure-sensitive modeling of rolling contact fatigue.* International Journal of Fatigue, 2010. **32**(5): p. 841-850.

34. Paulson, N.R., J.A.R. Bomidi, F. Sadeghi, and R.D. Evans, *Effects of crystal elasticity on rolling contact fatigue.* International Journal of Fatigue, 2014. **61**: p. 67-75.
35. Vijay, A., N. Paulson, and F. Sadeghi, *A 3D finite element modelling of crystalline anisotropy in rolling contact fatigue.* International Journal of Fatigue, 2018. **106**: p. 92-102.
36. Wang, W., H. Liu, C. Zhu, P. Wei, and J. Tang, *Effects of microstructure on rolling contact fatigue of a wind turbine gear based on crystal plasticity modeling.* International Journal of Fatigue, 2019. **120**: p. 73-86.
37. Jiang, Y. and H. Sehitoglu, *A model for rolling contact failure.* Wear, 1999. **224**(1): p. 38-49.
38. Wong, K.V. and A. Hernandez, *A review of additive manufacturing.* ISRN Mechanical Engineering, 2012. **2012**.
39. Huang, Y., M.C. Leu, J. Mazumder, and A. Donmez, *Additive Manufacturing: Current State, Future Potential, Gaps and Needs, and Recommendations.* Journal of Manufacturing Science and Engineering, 2015. **137**(1): p. 014001-014001-10.
40. Frazier, W.E., *Metal Additive Manufacturing: A Review.* Journal of Materials Engineering and Performance, 2014. **23**(6): p. 1917-1928.
41. Seifi, M., A. Salem, J. Beuth, O. Harrysson, and J.J. Lewandowski, *Overview of materials qualification needs for metal additive manufacturing.* Jom, 2016. **68**(3): p. 747-764.
42. Sames, W.J., F. List, S. Pannala, R.R. Dehoff, and S.S. Babu, *The metallurgy and processing science of metal additive manufacturing.* International Materials Reviews, 2016. **61**(5): p. 315-360.
43. Wei, H., J. Elmer, and T. DebRoy, *Origin of grain orientation during solidification of an aluminum alloy.* Acta Materialia, 2016. **115**: p. 123-131.
44. David, S. and J. Vitek, *Correlation between solidification parameters and weld microstructures.* International Materials Reviews, 1989. **34**(1): p. 213-245.
45. Chen, Y., F. Lu, K. Zhang, P. Nie, S.R.E. Hosseini, K. Feng, and Z. Li, *Dendritic microstructure and hot cracking of laser additive manufactured Inconel 718 under improved base cooling.* Journal of Alloys and Compounds, 2016. **670**: p. 312-321.
46. Xiao, H., S. Li, W. Xiao, Y. Li, L. Cha, J. Mazumder, and L. Song, *Effects of laser modes on Nb segregation and Laves phase formation during laser additive manufacturing of nickel-based superalloy.* Materials Letters, 2017. **188**: p. 260-262.
47. Parimi, L.L., G. Ravi, D. Clark, and M.M. Attallah, *Microstructural and texture development in direct laser fabricated IN718.* Materials Characterization, 2014. **89**: p. 102-111.
48. Thijs, L., F. Verhaeghe, T. Craeghs, J. Van Humbeeck, and J.-P. Kruth, *A study of the microstructural evolution during selective laser melting of Ti–6Al–4V.* Acta materialia, 2010. **58**(9): p. 3303-3312.
49. Koepf, J.A., M.R. Gotterbarm, M. Markl, and C. Körner, *3D multi-layer grain structure simulation of powder bed fusion additive manufacturing.* Acta Materialia, 2018. **152**: p. 119-126.
50. Keller, T., G. Lindwall, S. Ghosh, L. Ma, B.M. Lane, F. Zhang, U.R. Kattner, E.A. Lass, J.C. Heigel, and Y. Idell, *Application of finite element, phase-field, and CALPHAD-based methods to additive manufacturing of Ni-based superalloys.* Acta materialia, 2017. **139**: p. 244-253.

51. Nie, P., O. Ojo, and Z. Li, *Numerical modeling of microstructure evolution during laser additive manufacturing of a nickel-based superalloy.* Acta Materialia, 2014. **77**: p. 85-95.
52. Dezfoli, A.R.A., W.-S. Hwang, W.-C. Huang, and T.-W. Tsai, *Determination and controlling of grain structure of metals after laser incidence: Theoretical approach.* Scientific Reports, 2017. **7**: p. 41527.
53. Francois, M.M., A. Sun, W.E. King, N.J. Henson, D. Tourret, C.A. Bronkhorst, N.N. Carlson, C.K. Newman, T.S. Haut, and J. Bakosi, *Modeling of additive manufacturing processes for metals: Challenges and opportunities.* Current Opinion in Solid State and Materials Science, 2017. **21**(LA-UR-16-24513).
54. Ghosh, S., L. Ma, N. Ofori-Opoku, and J.E. Guyer, *On the primary spacing and microsegregation of cellular dendrites in laser deposited Ni–Nb alloys.* Modelling and simulation in materials science and engineering, 2017. **25**(6): p. 065002.
55. Akram, J., P. Chalavadi, D. Pal, and B. Stucker, *Understanding grain evolution in additive manufacturing through modeling.* Additive Manufacturing, 2018. **21**: p. 255-268.
56. Zinoviev, A., O. Zinovieva, V. Ploshikhin, V. Romanova, and R. Balokhonov, *Evolution of grain structure during laser additive manufacturing. Simulation by a cellular automata method.* Materials & Design, 2016. **106**: p. 321-329.
57. Rodgers, T.M., J.D. Madison, and V. Tikare, *Simulation of metal additive manufacturing microstructures using kinetic Monte Carlo.* Computational Materials Science, 2017. **135**: p. 78-89.
58. Lu, L.-X., N. Sridhar, and Y.-W. Zhang, *Phase field simulation of powder bed-based additive manufacturing.* Acta Materialia, 2018. **144**: p. 801-809.
59. Andani, M.T., M.R. Karamooz-Ravari, R. Mirzaeifar, and J. Ni, *Micromechanics modeling of metallic alloys 3D printed by selective laser melting.* Materials & Design, 2018. **137**: p. 204-213.
60. Mazumder, J., J. Choi, K. Nagarathnam, J. Koch, and D. Hetzner, *The direct metal deposition of H13 tool steel for 3-D components.* JOM, 1997. **49**(5): p. 55-60.
61. Gu, D., W. Meiners, K. Wissenbach, and R. Poprawe, *Laser additive manufacturing of metallic components: materials, processes and mechanisms.* International materials reviews, 2012. **57**(3): p. 133-164.
62. Andani, M.T., N.S. Moghaddam, C. Haberland, D. Dean, M.J. Miller, and M. Elahinia, *Metals for bone implants. Part 1. Powder metallurgy and implant rendering.* Acta biomaterialia, 2014. **10**(10): p. 4058-4070.
63. Shamsaei, N., A. Yadollahi, L. Bian, and S.M. Thompson, *An overview of Direct Laser Deposition for additive manufacturing; Part II: Mechanical behavior, process parameter optimization and control.* Additive Manufacturing, 2015. **8**: p. 12-35.
64. Yadollahi, A. and N. Shamsaei, *Additive manufacturing of fatigue resistant materials: Challenges and opportunities.* International Journal of Fatigue, 2017. **98**: p. 14-31.
65. Bian, L., S.M. Thompson, and N. Shamsaei, *Mechanical properties and microstructural features of direct laser-deposited Ti-6Al-4V.* Jom, 2015. **67**(3): p. 629-638.
66. Fatemi, A., R. Molaei, J. Simsiriwong, N. Sanaei, J. Pegues, B. Torries, N. Phan, and N. Shamsaei, *Fatigue behaviour of additive manufactured materials: An overview of some recent experimental studies on Ti-6Al-4V considering various processing and loading direction effects.* Fatigue & Fracture of Engineering Materials & Structures, 2019. **42**(5): p. 991-1009.

67. Yadollahi, A., N. Shamsaei, S.M. Thompson, A. Elwany, and L. Bian, *Effects of building orientation and heat treatment on fatigue behavior of selective laser melted 17-4 PH stainless steel.* International Journal of Fatigue, 2017. **94**: p. 218-235.
68. Yadollahi, A., M.J. Mahtabi, A. Khalili, H.R. Doude, and J.C. Newman Jr, *Fatigue life prediction of additively manufactured material: Effects of surface roughness, defect size, and shape.* Fatigue & Fracture of Engineering Materials & Structures, 2018. **41**(7): p. 1602-1614.
69. Molaei, R., A. Fatemi, N. Sanaei, J. Pegues, N. Shamsaei, S. Shao, P. Li, D.H. Warner, and N. Phan, *Fatigue of additive manufactured Ti-6Al-4V, Part II: The relationship between microstructure, material cyclic properties, and component performance.* International Journal of Fatigue, 2020. **132**: p. 105363.
70. Romano, S., A. Brückner-Foit, A. Brandão, J. Gumpinger, T. Ghidini, and S. Beretta, *Fatigue properties of AlSi10Mg obtained by additive manufacturing: Defect-based modelling and prediction of fatigue strength.* Engineering Fracture Mechanics, 2018. **187**: p. 165-189.
71. Andani, M.T., R. Dehghani, M.R. Karamooz-Ravari, R. Mirzaeifar, and J. Ni, *Spatter formation in selective laser melting process using multi-laser technology.* Materials & Design, 2017. **131**: p. 460-469.
72. Andani, M.T., R. Dehghani, M.R. Karamooz-Ravari, R. Mirzaeifar, and J. Ni, *A Study on the Effect of Energy Input on Spatter Particles Creation during Selective Laser Melting Process.* Additive Manufacturing, 2017. **20**: p. 33-43.
73. Andani, M.T., M. Ghodrati, M.R. Karamooz-Ravari, R. Mirzaeifar, J.J.M.S. Ni, and E. A, *Damage modeling of metallic alloys made by additive manufacturing.* Materials Science and Engineering: A, 2019. **743**: p. 656-664.
74. Andani, M.T., M.R. Karamooz-Ravari, R. Mirzaeifar, and J. Ni, *Micromechanics modeling of metallic alloys 3D printed by selective laser melting.* Materials and Design, 2018. **137**: p. 204-213.
75. Xie, F., Q. Chen, J. Gao, and Y. Li, *Laser 3D Printing of Fe-Based Bulk Metallic Glass: Microstructure Evolution and Crack Propagation*. Journal of Materials Engineering and Performance, 2019. **28**(6): p. 3478-3486.
76. Markus, J.B., *Molecular nanomechanics of nascent bone: fibrillar toughening by mineralization.* Nanotechnology, 2007. **18**(29): p. 295102.
77. Barthelat, F., *Nacre from mollusk shells: a model for high-performance structural materials.* Bioinspir Biomim, 2010. **5**(3): p. 035001.
78. Gupta, H.S., J. Seto, W. Wagermaier, P. Zaslansky, P. Boesecke, and P. Fratzl, *Cooperative deformation of mineral and collagen in bone at the nanoscale.* Proceedings of the National Academy of Sciences, 2006. **103**(47): p. 17741-17746.
79. Rho, J.-Y., L. Kuhn-Spearing, and P. Zioupos, *Mechanical properties and the hierarchical structure of bone.* Medical Engineering & Physics, 1998. **20**(2): p. 92-102.
80. He, L.H. and M.V. Swain, *Understanding the mechanical behaviour of human enamel from its structural and compositional characteristics.* Journal of the Mechanical Behavior of Biomedical Materials, 2008. **1**(1): p. 18-29.
81. Kamat, S., X. Su, R. Ballarini, and A.H. Heuer, *Structural basis for the fracture toughness of the shell of the conch Strombus gigas.* Nature, 2000. **405**: p. 1036.
82. Barthelat, F. and R. Rabiei, *Toughness amplification in natural composites.* Journal of the Mechanics and Physics of Solids, 2011. **59**(4): p. 829-840.

83. Bajaj, D., S. Park, G.D. Quinn, and D. Arola, *Fracture processes and mechanisms of crack growth resistance in human enamel.* JOM, 2010. **62**(7): p. 76-82.
84. Barthelat, F., *Architectured materials in engineering and biology: fabrication, structure, mechanics and performance.* International Materials Reviews, 2015. **60**(8): p. 413-430.
85. Aizenberg, J., J.C. Weaver, M.S. Thanawala, V.C. Sundar, D.E. Morse, and P. Fratzl, *Skeleton of Euplectella sp.: Structural Hierarchy from the Nanoscale to the Macroscale.* Science, 2005. **309**(5732): p. 275-278.
86. Bruet, B.J.F., J. Song, M.C. Boyce, and C. Ortiz, *Materials design principles of ancient fish armour.* Nature Materials, 2008. **7**: p. 748.
87. Currey, J.D., *Hierarchies in Biomineral Structures.* Science, 2005. **309**(5732): p. 253-254.
88. Fratzl, P. and R. Weinkamer, *Nature's hierarchical materials.* Progress in Materials Science, 2007. **52**(8): p. 1263-1334.
89. Gao, H., B. Ji, I.L. Jäger, E. Arzt, and P. Fratzl, *Materials become insensitive to flaws at nanoscale: Lessons from nature.* Proceedings of the National Academy of Sciences, 2003. **100**(10): p. 5597-5600.
90. Sen, D. and M.J. Buehler, *Structural hierarchies define toughness and defect-tolerance despite simple and mechanically inferior brittle building blocks.* Scientific Reports, 2011. **1**: p. 35.
91. Ji, B. and H. Gao, *A study of fracture mechanisms in biological nano-composites via the virtual internal bond model.* Materials Science and Engineering: A, 2004. **366**(1): p. 96-103.
92. Fratzl, P., H.S. Gupta, F.D. Fischer, and O. Kolednik, *Hindered Crack Propagation in Materials with Periodically Varying Young's Modulus—Lessons from Biological Materials.* Advanced Materials, 2007. **19**(18): p. 2657-2661.
93. Okumura, K. and P.-G. de Gennes, *Why is nacre strong? Elastic theory and fracture mechanics for biocomposites with stratified structures.* The European Physical Journal E, 2001. **4**(1): p. 121-127.
94. Dimas Leon, S., H. Bratzel Graham, I. Eylon, and J. Buehler Markus, *Tough Composites Inspired by Mineralized Natural Materials: Computation, 3D printing, and Testing.* Advanced Functional Materials, 2013. **23**(36): p. 4629-4638.
95. Livanov, K., H. Jelitto, B. Bar-On, K. Schulte, A. Schneider Gerold, and H. Wagner Daniel, *Tough Alumina/Polymer Layered Composites with High Ceramic Content.* Journal of the American Ceramic Society, 2014. **98**(4): p. 1285-1291.
96. Aksay, I.A., M. Trau, S. Manne, I. Honma, N. Yao, L. Zhou, P. Fenter, P.M. Eisenberger, and S.M. Gruner, *Biomimetic Pathways for Assembling Inorganic Thin Films.* Science, 1996. **273**(5277): p. 892-898.
97. Tang, Z., N.A. Kotov, S. Magonov, and B. Ozturk, *Nanostructured artificial nacre.* Nature Materials, 2003. **2**: p. 413.
98. Bouville, F., E. Maire, S. Meille, B. Van de Moortèle, A.J. Stevenson, and S. Deville, *Strong, tough and stiff bioinspired ceramics from brittle constituents.* Nature Materials, 2014. **13**: p. 508.
99. Deville, S., E. Saiz, R.K. Nalla, and A.P. Tomsia, *Freezing as a path to build complex composites.* Science, 2006. **311**(5760): p. 515-8.
100. Erb, R.M., R. Libanori, N. Rothfuchs, and A.R. Studart, *Composites Reinforced in Three Dimensions by Using Low Magnetic Fields.* Science, 2012. **335**(6065): p. 199-204.

101. Mirzaeifar, R., L.S. Dimas, Z. Qin, and M.J. Buehler, *Defect-Tolerant Bioinspired Hierarchical Composites: Simulation and Experiment.* ACS Biomaterials Science & Engineering, 2015. **1**(5): p. 295-304.
102. Mueller, T., A.G. Kusne, and R. Ramprasad, *Machine Learning in Materials Science: Recent Progress and Emerging Applications*. Reviews in Computational Chemistry. 2016. 88.
103. Hattrick-Simpers, J.R., J.M. Gregoire, and A.G. Kusne, *Perspective: Composition–structure–property mapping in high-throughput experiments: Turning data into knowledge.* APL Materials, 2016. **4**(5): p. 053211.
104. Ramprasad, R., R. Batra, G. Pilania, A. Mannodi-Kanakkithodi, and C. Kim, *Machine learning in materials informatics: recent applications and prospects.* npj Computational Materials, 2017. **3**(1): p. 54.
105. Liu, Y., T. Zhao, W. Ju, and S. Shi, *Materials discovery and design using machine learning.* Journal of Materiomics, 2017. **3**(3): p. 159-177.
106. Olson, G.B., *Designing a New Material World.* Science, 2000. **288**(5468): p. 993.
107. Kiani, J., C. Camp, and S. Pezeshk, *On the application of machine learning techniques to derive seismic fragility curves.* Computers & Structures, 2019. **218**: p. 108-122.
108. Gu, G.X., L. Dimas, Z. Qin, and M.J. Buehler, *Optimization of Composite Fracture Properties: Method, Validation, and Applications.* Journal of Applied Mechanics, 2016. **83**(7): p. 071006-071006-7.
109. Gu, G.X., S. Wettermark, and M.J. Buehler, *Algorithm-driven design of fracture resistant composite materials realized through additive manufacturing.* Additive Manufacturing, 2017. **17**: p. 47-54.
110. Xiang, S., H. Shi, K.-m. Wang, Y.-t. Ai, and Y.-d. Sha, *Thin plate spline radial basis functions for vibration analysis of clamped laminated composite plates.* European Journal of Mechanics - A/Solids, 2010. **29**(5): p. 844-850.
111. Orr, M.J.L., *Introduction to radial basis function networks*. 1996, Centre for Cognitive Science, Edinburgh University.
112. Katsikadelis, J.T. and N.G. Babouskos, *Stiffness and buckling optimization of thin plates with BEM.* Archive of Applied Mechanics, 2012. **82**(10): p. 1403-1422.
113. Chaboche, J.L., *Constitutive equations for cyclic plasticity and cyclic viscoplasticity.* International Journal of Plasticity, 1989. **5**(3): p. 247-302.
114. Rezvani Rad, M., G.H. Farrahi, M. Azadi, and M. Ghodrati, *Stress analysis of thermal barrier coating system subjected to out-of-phase thermo-mechanical loadings considering roughness and porosity effect.* Surface and Coatings Technology, 2015. **262**: p. 77-86.
115. Azadi, M., M. Ghodrati, and G.H. Farrahi, *Experimental and numerical evaluations of stress relaxation in A356 aluminium alloy subjected to out-of-phase thermomechanical cyclic loadings.* Materials at High Temperatures, 2014. **31**(3): p. 204-210.
116. Böhmer, A. and T. Klimpel, *Plastic deformation of corrugated rails—a numerical approach using material data of rail steel.* Wear, 2002. **253**(1): p. 150-161.
117. Rezvani Rad, M., G.H. Farrahi, M. Azadi, and M. Ghodrati, *Effects of preheating temperature and cooling rate on two-step residual stress in thermal barrier coatings considering real roughness and porosity effect.* Ceramics International, 2014. **40**(10, Part A): p. 15925-15940.

118. Chaboche, J.L., *A review of some plasticity and viscoplasticity constitutive theories.* International Journal of Plasticity, 2008. **24**(10): p. 1642-1693.
119. Farrahi, G.H., M. Ghodrati, M. Azadi, and M. Rezvani Rad, *Stress–strain time-dependent behavior of A356.0 aluminum alloy subjected to cyclic thermal and mechanical loadings.* Mechanics of Time-Dependent Materials, 2014. **18**(3): p. 475-491.
120. *ABAQUS 6.14, Abaqus Documentation, Providence (RI, USA): Dassault Systems Simulia Corp.; 2014.*
121. Pletz, M., W. Daves, W. Yao, W. Kubin, and S. Scheriau, *Multi-scale finite element modeling to describe rolling contact fatigue in a wheel–rail test rig.* Tribology International, 2014. **80**: p. 147-155.
122. Simonovski, I. and L. Cizelj, *Cohesive zone modeling of intergranular cracking in polycrystalline aggregates.* Nuclear Engineering and Design, 2015. **283**: p. 139-147.
123. Kabo, E. and A. Ekberg, *Material defects in rolling contact fatigue of railway wheels—the influence of defect size.* Wear, 2005. **258**(7-8): p. 1194-1200.
124. Onal, O., D. Canadinc, H. Sehitoglu, K. Verzal, and Y. Jiang, *Investigation of rolling contact crack initiation in bainitic and pearlitic rail steels.* Fatigue & Fracture of Engineering Materials & Structures, 2012. **35**(11): p. 985-997.
125. Khoramishad, H., A.D. Crocombe, K.B. Katnam, and I.A. Ashcroft, *Predicting fatigue damage in adhesively bonded joints using a cohesive zone model.* International Journal of Fatigue, 2010. **32**(7): p. 1146-1158.
126. Lemaitre, J. and R. Desmorat, *Engineering Damage Mechanics: Ductile, Creep, Fatigue and Brittle Failures*. 2005, Berlin: Springer Berlin Heidelberg.
127. Aglan, H.A. and M. Fateh, *Fracture and fatigue crack growth analysis of rail steels* Journal of Mechanics of Materials and Structures, 2007. **2**(2).
128. Weinzapfel, N. and F. Sadeghi, *Numerical modeling of sub-surface initiated spalling in rolling contacts.* Tribology International, 2013. **59**: p. 210-221.
129. Quey, R., P.R. Dawson, and F. Barbe, *Large-scale 3D random polycrystals for the finite element method: Generation, meshing and remeshing.* Computer Methods in Applied Mechanics and Engineering, 2011. **200**(17): p. 1729-1745.
130. *Elastic and Elastic-Plastic Contact*, in *Introduction to Contact Mechanics*, A.C. Fischer-Cripps, Editor. 2007, Springer US: Boston, MA. p. 175-188.
131. Marshall, M.B., R. Lewis, R.S. Dwyer-Joyce, U. Olofsson, and S. Björklund, *Experimental Characterization of Wheel-Rail Contact Patch Evolution.* Journal of Tribology, 2006. **128**(3): p. 493.
132. Nygårds, M. and P. Gudmundson, *Three-dimensional periodic Voronoi grain models and micromechanical FE-simulations of a two-phase steel.* Computational Materials Science, 2002. **24**(4): p. 513-519.
133. Ringsberg, J.W., M. Loo-Morrey, B.L. Josefson, A. Kapoor, and J.H. Beynon, *Prediction of fatigue crack initiation for rolling contact fatigue.* International Journal of Fatigue, 2000. **22**(3): p. 205-215.
134. Larijani, N., J. Brouzoulis, M. Schilke, and M. Ekh, *The effect of anisotropy on crack propagation in pearlitic rail steel.* Wear, 2014. **314**(1-2): p. 57-68.
135. Meymand, S.Z., A. Keylin, and M. Ahmadian, *A survey of wheel–rail contact models for rail vehicles.* Vehicle System Dynamics, 2016. **54**(3): p. 386-428.
136. Johnson, E., *Measurement of forces and neutral temperatures in railway rails - an introductory study*, in *SP Rapport*. 2004. p. 70.

137. Abdul-Baqi, A., P.J.G. Schreurs, and M.G.D. Geers, *Fatigue damage modeling in solder interconnects using a cohesive zone approach.* International Journal of Solids and Structures, 2005. **42**(3-4): p. 927-942.
138. Wang, Y.-q., H. Zhou, Y.-j. Shi, and B.-r. Feng, *Mechanical properties and fracture toughness of rail steels and thermite welds at low temperature.* International Journal of Minerals, Metallurgy, and Materials, 2012. **19**(5): p. 409-420.
139. Zerbst, U., M. Schödel, and R. Heyder, *Damage tolerance investigations on rails.* Engineering Fracture Mechanics, 2009. **76**(17): p. 2637-2653.
140. Ma, L., C.G. He, X.J. Zhao, J. Guo, Y. Zhu, W.J. Wang, Q.Y. Liu, and X.S. Jin, *Study on wear and rolling contact fatigue behaviors of wheel/rail materials under different slip ratio conditions.* Wear, 2016. **366-367**: p. 13-26.
141. Ekberg, A. and E. Kabo, *Fatigue of railway wheels and rails under rolling contact and thermal loading—an overview.* Wear, 2005. **258**(7-8): p. 1288-1300.
142. Li, Y., A.J. Bushby, and D.J. Dunstan, *The Hall-Petch effect as a manifestation of the general size effect.* Proc Math Phys Eng Sci, 2016. **472**(2190): p. 20150890.
143. *Metals Handbook Desk Edition, Second Edition*, J.R. Davis, Editor. 1998, ASM International. p. 153-173.
144. Owsiński, R., S. Kamiński, M. Szymaniec, A. Niesłony, and T. Łagoda, *Evaluation of fatigue life of steel using steel grain size.* Materialwissenschaft und Werkstofftechnik, 2015. **46**(10): p. 1059-1067.
145. Su, X. and P. Clayton, *Surface-initiated rolling contact fatigue of pearlitic and low carbon bainitic steels.* Wear, 1996. **197**(1): p. 137-144.
146. Beynon, J.H., J.E. Garnham, and K.J. Sawley, *Rolling contact fatigue of three pearlitic rail steels.* Wear, 1996. **192**(1): p. 94-111.
147. Zerbst, U., R. Lundén, K.O. Edel, and R.A. Smith, *Introduction to the damage tolerance behaviour of railway rails – a review.* Engineering Fracture Mechanics, 2009. **76**(17): p. 2563-2601.
148. Ringsberg, J.W., *Cyclic ratchetting and failure of a pearlitic rail steel.* Fatigue & Fracture of Engineering Materials & Structures, 2000. **23**(9): p. 747-758.
149. Frolish, M.F., D.I. Fletcher, and J.H. Beynon, *A quantitative model for predicting the morphology of surface initiated rolling contact fatigue cracks in back-up roll steels.* Fatigue & Fracture of Engineering Materials & Structures, 2002. **25**(11): p. 1073-1086.
150. Aglan, H.A., *Fatigue Crack Growth and Fracture Behavior of Bainitic Rails Steels*. 2011, Federal Railroad Administration.
151. Hill, R., *Generalized constitutive relations for incremental deformation of metal crystals by multislip.* Journal of the Mechanics and Physics of Solids, 1966. **14**(2): p. 95-102.
152. Rice, J.R., *Inelastic constitutive relations for solids: an internal-variable theory and its application to metal plasticity.* Journal of the Mechanics and Physics of Solids, 1971. **19**(6): p. 433-455.
153. Asaro, R.J., *Micromechanics of crystals and polycrystals*, in *Advances in applied mechanics*. 1983, Elsevier. p. 1-115.
154. Peirce, D., R. Asaro, and A. Needleman, *An analysis of nonuniform and localized deformation in ductile single crystals.* Acta metallurgica, 1982. **30**(6): p. 1087-1119.
155. Huang, Y., *A user-material subroutine incroporating single crystal plasticity in the ABAQUS finite element program*. 1991: Harvard Univ.

156. Ghodrati, M., M. Ahmadian, and R. Mirzaeifar, *Modeling of rolling contact fatigue in rails at the microstructural level.* Wear, 2018. **406–407**: p. 205-217.
157. Yan, W. and F.D. Fischer, *Applicability of the Hertz contact theory to rail-wheel contact problems.* Archive of Applied Mechanics, 2000. **70**(4): p. 255-268.
158. Zhu, Y., *Adhesion in the wheel-rail contact*, in *Trita-MMK*. 2013, KTH Royal Institute of Technology: Stockholm. p. 31.
159. Haines, D.J. and E. Ollerton, *Contact Stress Distributions on Elliptical Contact Surfaces Subjected to Radial and Tangential Forces.* Proceedings of the Institution of Mechanical Engineers, 1963. **177**(1): p. 95-114.
160. Srivastava, J.P., P.K. Sarkar, V.R.K. Meesala, and V. Ranjan, *Rolling Contact Fatigue Life of Rail for Different Slip Conditions.* Latin American Journal of Solids and Structures, 2017. **14**: p. 2243-2264.
161. Caprioli, S. and A. Ekberg, *Numerical evaluation of the material response of a railway wheel under thermomechanical braking conditions.* Wear, 2014. **314**(1): p. 181-188.
162. Ciavarella, M., F. Monno, and G. Demelio, *On the Dang Van fatigue limit in rolling contact fatigue.* International Journal of Fatigue, 2006. **28**(8): p. 852-863.
163. Brommesson, R., M. Ekh, and C. Joseph, *3D grain structure modelling of intergranular fracture in forged Haynes 282.* Engineering Fracture Mechanics, 2016. **154**: p. 57-71.
164. Coenen, E.W.C., V.G. Kouznetsova, and M.G.D. Geers, *Novel boundary conditions for strain localization analyses in microstructural volume elements.* International Journal for Numerical Methods in Engineering, 2012. **90**(1): p. 1-21.
165. Pierce, D.T., K. Nowag, A. Montagne, J.A. Jiménez, J.E. Wittig, and R. Ghisleni, *Single crystal elastic constants of high-manganese transformation- and twinning-induced plasticity steels determined by a new method utilizing nanoindentation.* Materials Science and Engineering: A, 2013. **578**: p. 134-139.
166. Lindroos, M., A. Laukkanen, G. Cailletaud, and V.-T. Kuokkala, *On the effect of deformation twinning and microstructure to strain hardening of high manganese austenitic steel 3D microstructure aggregates at large strains.* International Journal of Solids and Structures, 2017. **125**: p. 68-76.
167. Simonovski, I., K.-F. Nilsson, and L. Cizelj. *Material Properties Calibration for 316L Steel Using Polycrystalline Model*. in *Proceedings of the 13th International Conference on Nuclear Engineering*. 2005. Chinese Nuclear Society.
168. El Shawish, S. and L. Cizelj, *Combining Single- and Poly-Crystalline Measurements for Identification of Crystal Plasticity Parameters: Application to Austenitic Stainless Steel.* Crystals, 2017. **7**(6).
169. Tvergaard, V. and J.W. Hutchinson, *The relation between crack growth resistance and fracture process parameters in elastic-plastic solids.* Journal of the Mechanics and Physics of Solids, 1992. **40**(6): p. 1377-1397.
170. Simonovski, I. and L. Cizelj, *Cohesive element approach to grain level modelling of intergranular cracking.* Engineering Fracture Mechanics, 2013. **110**: p. 364-377.
171. Clayton, P. and X. Su, *Surface initiated fatigue of pearlitic and bainitic steels under water lubricated rolling/sliding contact.* Wear, 1996. **200**(1): p. 63-73.
172. Wang, W.J., S.R. Lewis, R. Lewis, A. Beagles, C.G. He, and Q.Y. Liu, *The role of slip ratio in rolling contact fatigue of rail materials under wet conditions.* Wear, 2017. **376-377**: p. 1892-1900.

173. Andani, M.T., M. Ghodrati, M.R. Karamooz-Ravari, R. Mirzaeifar, and J. Ni, *Damage Modeling of 3D Printed Metallic Alloys.* Acta Materialia, 2018.
174. Hussein, A., L. Hao, C. Yan, and R. Everson, *Finite element simulation of the temperature and stress fields in single layers built without-support in selective laser melting.* Materials & Design (1980-2015), 2013. **52**: p. 638-647.
175. Vrancken, B., L. Thijs, J.-P. Kruth, and J. Van Humbeeck, *Heat treatment of Ti6Al4V produced by Selective Laser Melting: Microstructure and mechanical properties.* Journal of Alloys and Compounds, 2012. **541**: p. 177-185.
176. Andani, M.T., R. Dehghani, M.R. Karamooz-Ravari, R. Mirzaeifar, and J. Ni, *A study on the effect of energy input on spatter particles creation during selective laser melting process.* Additive Manufacturing, 2018. **20**: p. 33-43.
177. Gu, D., Y.-C. Hagedorn, W. Meiners, G. Meng, R.J.S. Batista, K. Wissenbach, and R. Poprawe, *Densification behavior, microstructure evolution, and wear performance of selective laser melting processed commercially pure titanium.* Acta Materialia, 2012. **60**(9): p. 3849-3860.
178. Dinda, G., A. Dasgupta, and J. Mazumder, *Evolution of microstructure in laser deposited Al–11.28% Si alloy.* Surface and Coatings Technology, 2012. **206**(8-9): p. 2152-2160.
179. Mirzaeifar, R., R. DesRoches, A. Yavari, and K. Gall, *A micromechanical analysis of the coupled thermomechanical superelastic response of textured and untextured polycrystalline NiTi shape memory alloys.* Acta Materialia, 2013. **61**(12): p. 4542-4558.
180. Bisht, M., N. Ray, F. Verbist, and S. Coeck, *Correlation of selective laser melting-melt pool events with the tensile properties of Ti-6Al-4V ELI processed by laser powder bed fusion.* Additive Manufacturing, 2018. **22**: p. 302-306.
181. Prashanth, K.G. and J. Eckert, *Formation of metastable cellular microstructures in selective laser melted alloys.* Journal of Alloys and Compounds, 2017. **707**: p. 27-34.
182. Saeidi, K., X. Gao, Y. Zhong, and Z.J. Shen, *Hardened austenite steel with columnar sub-grain structure formed by laser melting.* Materials Science and Engineering: A, 2015. **625**: p. 221-229.
183. Wang, D., C. Song, Y. Yang, and Y. Bai, *Investigation of crystal growth mechanism during selective laser melting and mechanical property characterization of 316L stainless steel parts.* Materials & Design, 2016. **100**: p. 291-299.
184. Wang, Y.M., T. Voisin, J.T. McKeown, J. Ye, N.P. Calta, Z. Li, Z. Zeng, Y. Zhang, W. Chen, T.T. Roehling, R.T. Ott, M.K. Santala, Philip J. Depond, M.J. Matthews, A.V. Hamza, and T. Zhu, *Additively manufactured hierarchical stainless steels with high strength and ductility.* Nature Materials, 2017. **17**: p. 63.
185. Zhong, Y., L. Liu, S. Wikman, D. Cui, and Z. Shen, *Intragranular cellular segregation network structure strengthening 316L stainless steel prepared by selective laser melting.* Journal of Nuclear Materials, 2016. **470**: p. 170-178.
186. Ghodrati, M., M. Ahmadian, and R. Mirzaeifar, *Three-dimensional study of rolling contact fatigue using crystal plasticity and cohesive zone method.* International Journal of Fatigue, 2019. **128**: p. 105208.
187. Ray, A. and M.-K. Wu, *Fatigue damage control of mechanical systems.* Smart Materials and Structures, 1994. **3**(1): p. 47-58.
188. Zhao, B., F. Shen, Y. Cui, Y. Xie, and K. Zhou, *Damage analysis for an elastic-plastic body in cylindrical contact with a rigid plane.* Tribology International, 2017. **115**: p. 18-27.

189. Roy, S.C., S. Goyal, R. Sandhya, and S.K. Ray, *Low cycle fatigue life prediction of 316 L(N) stainless steel based on cyclic elasto-plastic response.* Nuclear Engineering and Design, 2012. **253**: p. 219-225.
190. Vijay, A. and F. Sadeghi, *An anisotropic damage model for tensile fatigue.* Fatigue & Fracture of Engineering Materials & Structures, 2019. **42**(1): p. 129-142.
191. Bass, L., C.B. Williams, and N.A. Meisel, *Exploring variability of orientation and aging effects in material properties of multi-material jetting parts.* Rapid Prototyping Journal, 2016. **22**(5): p. 826-834.
192. Gu, G.X., C.-T. Chen, and M.J. Buehler, *De novo composite design based on machine learning algorithm.* Extreme Mechanics Letters, 2018. **18**: p. 19-28.
193. Deb, K., S. Agrawal, A. Pratap, and T. Meyarivan. *A Fast Elitist Non-dominated Sorting Genetic Algorithm for Multi-objective Optimization: NSGA-II*. in *Parallel Problem Solving from Nature PPSN VI*. 2000. Berlin, Heidelberg: Springer Berlin Heidelberg.
194. Coello, C.A. and A.D. Christiansen, *Multiobjective optimization of trusses using genetic algorithms.* Computers & Structures, 2000. **75**(6): p. 647-660.
195. Bouazizi, M.L., S. Ghanmi, R. Nasri, and N. Bouhaddi, *Robust optimization of the non-linear behaviour of a vibrating system.* European Journal of Mechanics - A/Solids, 2009. **28**(1): p. 141-154.
196. Fu, Z., J. Mo, L. Chen, and W. Chen, *Using genetic algorithm-back propagation neural network prediction and finite-element model simulation to optimize the process of multiple-step incremental air-bending forming of sheet metal.* Materials & Design, 2010. **31**(1): p. 267-277.
197. Mashhadi, B., H. Mousavi, and M. Montazeri, *Obtaining relations between the Magic Formula coefficients and tire physical properties.* IUST, 2015. **5**(1): p. 911-922.
198. Sadr, M.H., S. Astaraki, and S. Salehi, *Improving the neural network method for finite element model updating using homogenous distribution of design points.* Archive of Applied Mechanics, 2007. **77**(11): p. 795-807.
199. Kollár, L.P. and G.S. Springer, *Mechanics of Composite Structures*. 2003, Cambridge: Cambridge University Press.
200. Allien, V.J., H. Kumar, and V. Desai, *Dynamic analysis and optimization of SiC reinforced Al6082 and Al7075 MMCs.* Materials Research Express, 2019. **6**(5): p. 056528.
201. Guo, X. and H. Gao. *Bio-Inspired Material Design and Optimization*. in *IUTAM Symposium on Topological Design Optimization of Structures, Machines and Materials*. 2006. Dordrecht: Springer Netherlands.